Ocean Acidification and Changes in Marine Productivity in Simulations with the Fully Coupled 3-D Climate Model CSM1.4-carbon

Diplomarbeit

der Philosophisch–naturwissenschaftlichen Fakultät
der Universität Bern

vorgelegt von
Marco Steinacher
2007

Leiter der Arbeit:
Prof. Dr. F. Joos

Abteilung für Klima– und Umweltphysik
Physikalisches Institut der Universität Bern

Contents

Thesis summary

In the first part of this thesis, the fundamental concepts of the global carbon cycle and in particular the role of the ocean are presented (chapter 1). Covering about 70% of the Earth's surface and being a vast carbon reservoir, the ocean is an important part of the global carbon cycle. Several coupled biogeochemical cycles exist in the ocean. Most relevant to this thesis are the production, export and remineralization of organic matter, as well as the calcium carbonate cycle.

Most results in this thesis are from simulations performed with the NCAR CSM1.4-carbon model (chapter 2). This is a fully coupled state-of-the-art climate model consisting of ocean, atmosphere, land and sea-ice components and it includes biogeochemical land and ocean models. The simulations are performed over the period 1820 to 2100 and are mainly based on historical CO_2 emissions (1820-2000) and future emission scenarios (SRES A2 and B1, 2000-2100).

The analysis of the simulation results with respect to ocean acidification (chapter 3) shows that the model results match data-based estimates reasonably well in most regions. There is a weakness in the North Pacific Intermediate Water and the saturation horizon generally tends to be somewhat too deep. The simulated seasonal variability in the aragonite saturation state is small in the high latitude and tropical ocean. In the mid-latitudes of the Northern Hemisphere there are deviations up to 15-20% from the annual mean. The interannual variability is small. The carbonate saturation state at the surface is mainly given by the in-situ CO_3^{-2} concentration. The direct influence of temperature and salinity is relatively small. The Arctic surface ocean becomes undersaturated with respect to aragonite for atmospheric CO_2 exceeding 475 ppm, which is reached by 2040 in the SRES A2 scenario. After the year 2070 (625 ppm) high latitude waters become largely undersaturated. Surface waters with $\Omega_A > 4$ disappear by 2010 and the global volume of undersaturated waters increases by about 30% until 2100. The global annual mean surface pH drops from 8.17 (1820) to 7.77 (2100) in the A2 scenario. Largest pH changes (about -0.46) can be found in the Arctic. Changes in the seasonal variability are small in the future scenarios. The global warming has only a little effect on ocean acidification in most regions, except for the Arctic Ocean and a part of the North Atlantic. The projected decrease in global annual mean Ω_A is about 4 % larger without changing climate due to increased CO_2 uptake by the ocean.

Simulations with the NCAR CSM1.4-carbon and two other models (IPSL and MPIM) project a decrease in marine primary productivity of 7% to 25% (-2.0 GtC/yr to -8.8 GtC/yr) from 1860 to 2100 (chapter 4). There are, however, relatively large differences between the three model results. The simulated production in the IPSL model is significantly higher as in the other models and shows also the largest changes during the simulation. The NCAR

model projects largest reductions in the North Atlantic, whereas the other models show more distributed changes with maxima in the low latitude ocean. Production is partially enhanced in the Southern Ocean, in the North Pacific and in the Arctic. Finding clear drivers of the productivity changes is difficult. In the NCAR model, mixed layer dynamics seem to play an important role, ecpecially in the North Atlantic. Stratification is enhanced in all models and regions, which leads to a reduction of surface nutrient concentrations in many regions. In the NCAR model, reduced phosphate diminishes production in the North and South Atlantic, as well as in the West Indian Ocean, whereas reduced iron concentrations dominate the productivity changes in the Pacific.

Chapter 1

Introduction

There is strong evidence that the Earth's climate has changed since the onset of the industrial revolution. It is also likely that it will continue to change, because carbon dioxide emissions, which are known to contribute largely to the climate change, are still increasing in order to meet the energy demands of the world population. But the question how it will change is difficult to answer, because it depends on many factors (e.g. future carbon emissions and mitigation initiatives) and because our understanding of the climate system is still limited, although much facts are broadly accepted nowadays. The first problem can be circumvented by defining certain scenarios and base future projections thereon. In order to improve our knowledge of the climate system, modeling studies can help and are the tool of choice when assessing future climate change.

This thesis attempts to evaluate two specific consequences related to the global carbon cycle using a state-of-the-art climate model described in chapter 2. The first consequence is that the ocean chemistry is changing due to increased atmospheric carbon dioxide concentrations and subsequent uptake by the ocean. This effect is known as 'ocean acidification' and will be discussed in chapter 3. The other consequence, which will be discussed in chapter 4, is that climate change also affects marine biota and biological productivity in the ocean, which in turn are important components of the global carbon cycle.

This first chapter presents an overview of the carbon cycle and the relevant mechanisms for this thesis.

1.1 The global carbon cycle

The chemical element carbon is essential for life on Earth. It's the basis of organic chemistry and occurs in all organic life, but is also a component of carbon dioxide (CO_2) and methane (CH_4), which are the two most important greenhouse gases after water vapor.

The amount of carbon on Earth is almost constant, thus if carbon is disposed somewhere (e.g. plants that build biomass by carbon respiration), it has to be obtained from somewhere else. The processes that are responsible for such carbon fluxes can be biological, geological, chemical or physical and the entire system is usually referred to as the global carbon cycle. Similar biogeochemical cycles exist also for oxygen (O) and other elements like nitrogen (N), phosphorus (P), silicon (Si), iron (Fe), etc.

Since the industrial revolution, the carbon cycle plays an even more important role, because it is tightly coupled to the energy needs of the growing world population. Energy sources like crude oil, natural gas and coal are extracted and consumed in large amounts and short time. This leads, together with increased land use (e.g. deforestation), to a significant perturbation of the global carbon cycle, and thus, of the climate system as a whole.

1.1.1 Carbon reservoirs and fluxes

The main carbon reservoirs are the atmosphere, the biosphere, the ocean and sediments. Table 1.1 shows estimated fluxes, residence times and the amount of carbon stored in these reservoirs. The atmosphere contains carbon mainly in the form of carbon dioxide, methane and carbon monoxide (CO). The biomass in the biosphere can be summarized by glucose ($C_6H_{12}O_6$) and most of carbon in living biomass is stored on land. In the ocean, carbon can be found mainly in dissolved inorganic form (dissolved inorganic carbon, DIC) and some amount of dissolved organic carbon (DOC). The biggest carbon reservoirs are sediments, that contain predominantly $CaCO_3$ and $MgCO_3$. The residence time of carbon in sediments is long and processes are only relevant on time scales of more than a 1000 years.

The most important carbon fluxes are those between atmosphere and biosphere (photosynthesis/respiration) and the gas exchange between the atmosphere and the surface ocean. Furthermore there are carbon fluxes from living land biota to soils, and from soils to the atmosphere, as well as transport of carbon by rivers from the land to the ocean and sedimentation in the ocean. The fluxes in the ocean are rather complex and discussed separately in the next section.
The pre-industrial carbon cycle was changed by additional fluxes from the land to the atmosphere induced by land use emissions and fossil fuel combustion. In consequence, the amount of carbon in the land biosphere and soils decline, while the atmosphere and the ocean accumulate carbon.

1.2 The ocean carbon cycle

The ocean is of major importance for the global carbon cycle because it is the biggest carbon reservoir with relatively short residence times. It contains about 60 times more carbon than the atmosphere and controls the atmospheric CO_2 concentration on time scales up to several 1000 years.

The carbon cycle in the ocean is determined by the interaction of various biogeochemical processes and is tightly coupled to the cycle of nutrients like iron (Fe), phosphate (P) and nitrate (N). The ocean circulation and mixing by itself would lead to a uniform distribution of matter as it is more or less the case with salinity. This is not the case for carbon, because the distribution of carbon is also affected by the carbonate chemistry in the water and biological processes.

1.2.1 Production, export and remineralization of organic matter

In the euphotic zone near the ocean surface ($\approx$ top 100 m), where light and nutrients are abundant, the production of organic matter, calcium carbonate ($CaCO_3$), and silicate shells

Atmosphere	
CO_2 (before 1850)	594 GtC
CO_2 (2000)	786 GtC
CH_4/CO	4 GtC
Atm. - ocean CO_2 exchange	78 GtC/yr
Atm. - land biota, photosynthesis/respiration	65 GtC/yr
Residence time (total)	4 yr
Exchange with ocean only	8 yr
Exchange with land only	9 yr
Land	
Living biota	560 GtC
Soil, humus	1500 GtC
Groundwater	450 GtC
Fossil fuels	ca. 5500 GtC
Volcanism	ca. 0.07 GtC/yr
Fossil fuel combustion (2000)	6.5 GtC/yr
Living biota residence time	11yr
Oceans	
Inorganic C (DIC)	37400 GtC
Dissolved organic matter (DOM)	ca. 1600 GtC
Biomass	3 GtC
Marine photosynthesis	45 GtC/yr
Sedimentation	0.2 GtC/yr
Residence time (photosynthesis)	0.07 yr
Exchange with atmosphere	530 yr
Sedimentation only	200'000 yr
Sediments	
Inorganic C	ca. 60'000'000 GtC
Organic C	ca. 12'000'000 GtC
Residence time	212'000 yr

Table 1.1: Major global carbon reservoirs, gross fluxes and resident times. The estimated amount of carbon is given in gigatons carbon (1 GtC = 10^{15} g Carbon). The residence time is defined as $\tau = \frac{M}{F}$, where M is the mass in the reservoir and F the flux. (Main sources: Bolin et al. (1979), Bolin (1981), Clark (1982))

(SiO_2, opal) takes place. Carbon and nutrients are turned into organic matter by marine organisms (mostly phytoplankton) via photosynthesis. After subtracting the metabolic costs of all other metabolic processes by the organisms themselves, the remaining organic carbon becomes available to heterotrophs (organisms that require organic substrates to get carbon) and is called net primary production (NPP). The main factors that determine the amount of NPP are temperature, the availability of light (required for photosynthesis), and the availability of macro- (e.g. N,P) and micronutrients[1] (trace elements like Fe).

A part of the organic carbon is exported to the deep ocean either in the form of dissolved organic matter (DOM) or particulate organic matter (POM). DOM is transported by ocean circulation and mixing only, whereas the heavier POM is also transported by particle settling (gravitational sinking). The fraction of the produced organic matter that leaves the euphotic zone, is called export production (EP). The efficiency of vertical POM transport is strongly related to the strength of the oceanic sink for atmospheric CO_2, because it influences the CO_2 partial pressure (pCO_2) at the surface and thus the ocean's ability to absorb CO_2 from the atmosphere.

The majority of exported organic matter is remineralized in the upper few 100 m of the thermocline[2] and only a small fraction makes it to the deep ocean. The understanding of remineralization is lesser developed then our understanding how organic matter is formed in the euphotic zone. Most of the organic matter is remineralized by heterotrophic organisms within the water column or in sediments. Normally oxygen is used as oxidant (aerobic remineralization), leading to reduced oxygen concentrations where the remineralization takes place. Where oxygen is scarce, nitrate can replace oxygen and nitrate is reduced (referred to as denitrification).

The so-called 'biological pump' (or 'soft-tissue pump' when referring explicitly to the cycling of organic matter and not to that of minerals like calcium carbonate) refers to the production of organic matter from inorganic nutrients and carbon in the euphotic zone near the ocean surface, and the transport to deep and intermediate waters, followed by the remineralization of the organic matter to inorganic nutrients and carbon, which then are transported back to the surface by circulation and mixing. The term 'pump' is used for that process, because it transports nutrients and carbon from the surface to the intermediate and deep ocean. The concentrations of nutrients and carbon is reduced in the surface ocean and increased in the intermediate and deep ocean. Ocean circulation and mixing counteracts this process and lead to a vertical gradient of carbon and nutrient concentrations in the steady state. Circulation and mixing only would result in a more uniform distribution as it is the case for salinity.

Because the molecular ratios of C, N and P in phytoplankton is relatively constant, the relative amount of carbon and different inorganic nutrients that are involved in the production and remineralization of organic matter is almost constant. The ratios P:N:C:O_2 = 1:16:106:-150 are known as the Redfield-ratios and follow from the "best guess" of the stoichiometry of organic carbon production:

$$106\ CO_2 + 16\ HNO_3 + H_3PO_4 + 78\ H_2O = C_{106}H_{175}O_{42}N_{16}P + 150\ O_2 \qquad (1.1)$$

[1] Nutrients are defined as components of sea water that sometimes limit biological production of organic matter. Carbon is always available and thus no nutrient.

[2] The thermocline is a layer in the water column below the mixed layer where the temperature changes rapidly with depth.

The composition of this organic matter is 54.4% protein, 25% carbohydrate, 16.1% lipid, and 4.0% nucleic acid by dry weight [Sarmiento and Gruber, 2004].
Most of the water column remineralization of organic matter occurs by the reverse of the synthesis reaction at the surface (eq. 1.1). However, the stoichiometry of the remineralization reaction below 400 m appears to be somewhat different:

$$\mathrm{P : N : C_{org} : O_2} = 1 : (16 \pm 1) : 117(\pm 14) : (-170 \pm 10) \tag{1.2}$$

Two important measures that are influenced by the biological pump are dissolved inorganic carbon (DIC, often also referred to as total inorganic carbon or total CO_2) and alkalinity (Alk). Alkalinity is a measure of the ability of a solution to neutralize acids. Alk and DIC are defined as

$$\begin{aligned} \mathrm{DIC} &= [\mathrm{CO_2^*}] + [\mathrm{HCO_3^-}] + [\mathrm{CO_3^{2-}}] && (1.3)\\ \mathrm{Alk} &= [\mathrm{HCO_3^-}] + 2[\mathrm{CO_3^{2-}}] + [\mathrm{OH^-}] - [\mathrm{H^+}] + [\mathrm{B(OH)_4^-}] && (1.4)\\ &\quad +[\mathrm{HPO_4^{2-}}] + \text{minor bases.} \end{aligned}$$

Knowing that NO_3^- and HPO_4^{-2} rather than HNO_3 and H_3PO_4, respectively, are the dominant chemical species present in seawater, equation 1.1 can be rewritten as

$$106\ \mathrm{CO_2} + 16\ \mathrm{NO_3^-} + \mathrm{HPO_4^{2-}} + 78\ \mathrm{H_2O} + 18\ \mathrm{H^+} = \mathrm{C_{106}H_{175}O_{42}N_{16}P} + 150\ \mathrm{O_2}. \tag{1.5}$$

From this it follows that the production of 1 mol organic matter decreases DIC by 106 mol ($-106\ CO_2$) and increases Alk by about 17 moles ($-18\ H^+$, $-HPO_4^{2-}$). Accordingly, the remineralization of organic matter increases DIC and decreases Alk.
The effect of the biological pump on DIC and Alk exhibit an important connection to the calcium carbonate cycle discussed in section 1.2.3, because the net effect of both, organic matter production/remineralization and calcium carbonate production/dissolution, determines the resulting DIC and Alk concentrations.

1.2.2 CO_2 uptake by the ocean

Besides the biological pump, the exchange of CO_2 with the atmosphere plays an important role in the marine carbon cycle, particularly because of anthropogenic emissions, that lead to an uptake of CO_2 by the ocean.

Atmospheric CO_2 enters the ocean by the air-sea gas exchange at the ocean surface, which tends to equilibrate the partial pressure (pCO_2) across the air-sea interface (Figure 1.1). Most of the CO_2 molecules combine with water to carbonic acid (H_2CO_3) and only a small fraction remains in aqueous solution $CO_{2(aq)}$. Like all acids, H_2CO_3 releases hydrogen ions (H^+) into the solution, leaving bicarbonate (HCO_3^-) and carbonate (CO_3^{2-}) ions. Again a little fraction of H_2CO_3 does not dissolve and is identified together with $CO_{2(aq)}$ as CO_2^*. The release of H^+ into the solution lowers the pH[3] of the seawater and decreases the carbonate ion concentration $[CO_3^{2-}]$, because some CO_3^{2-} combine with H^+ to HCO_3^-.

[3] pH is a measure of the acidity or basicity of a solution and defined as $\mathrm{pH} = -\log_{10}(a_{\mathrm{H^+}})$, where $a_{\mathrm{H^+}}$ denotes the activity of H^+ ions. In dilute solutions, the activity is approximately equal to the numeric value of the concentration of the H^+ ion; $\mathrm{pH} \approx -\log_{10}([\mathrm{H^+}])$.

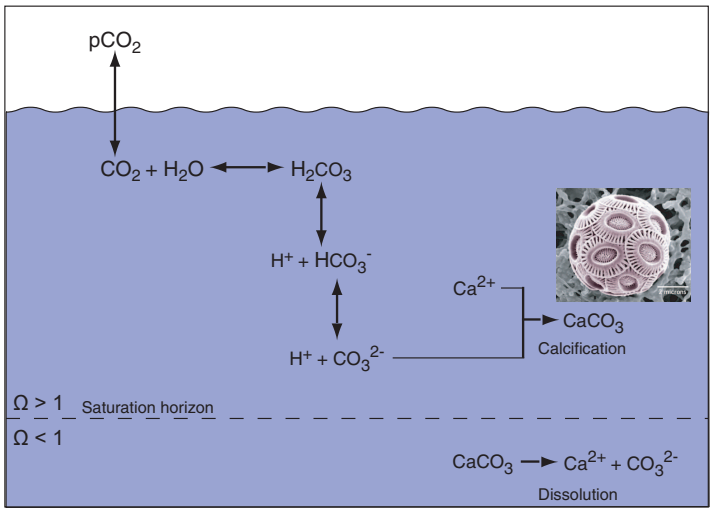

Figure 1.1: A simplified diagram of the carbonate system in seawater. Ocean uptake of CO_2 changes the carbonate ion concentration [CO_3^{2-}], which has an influence on calcifying organisms.

This series of chemical equilibria determines the partitioning of the components CO_2, H_2CO_3, HCO_3^- and CO_3^{2-}, which are identified together as total dissolved inorganic carbon (DIC). From the net chemical reaction

$$H_2O + CO_2 + CO_3^{2-} \Leftrightarrow 2HCO_3^- \tag{1.6}$$

follows that if CO_2 rises, the CO_3^{2-} concentration falls. One consequence is the change in the calcium carbonate saturation state Ω, as discussed in the next section.

1.2.3 Calcium carbonate ($CaCO_3$)

The calcium carbonate cycle is a process similar to the 'soft-tissue' pump discussed above, sometimes referred to as 'carbonate pump'. Mineral calcium carbonates ($CaCO_3$) are produced by organisms and exported to the deep ocean and to sediments. One important difference to the export of organic matter is that about a third of the $CaCO_3$ that leaves the surface arrives at the sediments, and that about half of this $CaCO_3$ is buried, whereas only about 0.2% of surface organic matter export is buried [Sarmiento and Gruber, 2004].
Because of the high burial of $CaCO_3$, a significant amount of alkalinity (removal of CO_3^{2-}) is lost from the ocean, which is replaced by riverine input of Alk stemming from continental weathering and a small input from hydrothermal vents. On time scales larger than 1000 years, the calcium carbonate cycle leads to a negative (stabilizing) feedback, which forces the system towards an equilibrium between the input of alkalinity by weathering and the burial of alkalinity in sediments. This provides a mechanism, often referred to as calcium carbonate compensation, to reduce perturbations in atmospheric CO_2 by the ocean-sediment flux. Changes in the export production of $CaCO_3$ on the other hand, can influence atmospheric CO_2.

Although the water in the upper layers of the ocean is supersaturated with respect to Ca^{2+} and CO_3^{2-}, mineral calcium carbonates are formed almost exclusively by biological processes [Sarmiento and Gruber, 2004]. There are three groups of marine organisms that are mainly

responsible for the production of $CaCO_3$ in the open ocean: Coccolithophorids, Foraminifera and Pteropods. Coccolithophorids are a phytoplankton group and the other two are zooplankton. They form shells or skeletons out of calcite or aragonite. Aragonite is the less stable phase of $CaCO_3$ at any pressure and temperature in the oceans. In the benthic zone $CaCO_3$ is mainly produced by corals, calcifying algae, benthic foraminifera, molluscs and echinoderms [Kleypas et al., 2006].

Several experiments have shown that coral calcification is mainly controlled by $[CO_3^{2-}]$, rather than by pH or other factors [Schneider and Erez, 2006]. Further, Gattuso et al. [1998] and Langdon et al. [2000] found in experiments that an increase in $[Ca^{2+}]$ has the same effect on coral calcification as an increase in $[CO_3^{2-}]$, if $[CO_3^{2-}]$ is not limiting. This leads to the hypothesis that the calcium carbonate saturation state defined as

$$\Omega = \frac{[Ca^{2+}][CO_3^{2-}]}{K_{sp}} \tag{1.7}$$

mainly determines the calcification rate by corals, and possibly, by other calcifiers.

Studies have confirmed that chemical precipitation is proportional to Ω; the greater the ion concentration product, the greater the rate of formation of the mineral. The relationship is described by a rate law of the form

$$R = k(\Omega - 1)^n, \tag{1.8}$$

where k is the rate constant and n the order of the reaction. There is some controversy as to whether in the case of aragonite precipitation in seawater n=1 [Inskeep and Bloom, 1985] or n=1.8-2.4 [Zhong and Mucci, 1989].

It is believed that many calcification data sets are well described by this rate law [Kleypas et al., 2006]. Langdon and Atkinson [2005] found that the first-order saturation state model gave a good fit to the calcification rates of an assemblage of corals during summer and winter: $R = (8 \pm 1 \text{ mmol } CaCO_3 \text{ m}^{-2}\text{h}^{-1})(\Omega_A - 1)$.

In equation 1.7, $K_{sp} = [Ca^{2+}]_{sat}[CO_3^{2-}]_{sat}$ is the solubility product defined by the equilibrium relationship for the dissolution reaction of mineral $CaCO_3$

$$Ca^{2+} + CO_3^{2-} \Leftrightarrow CaCO_3 \tag{1.9}$$

with $[Ca^{2+}]_{sat}$ and $[CO_3^{2-}]_{sat}$ being the concentrations of the dissolved calcium and carbonate ions in equilibrium with mineral $CaCO_3$. Because the solubility product is different for different phases of mineral $CaCO_3$, we differentiate between Ω_C and Ω_A, that denote the saturation states with respect to calcite and the less stable aragonite. The concentrations of Ca^{2+} in normal seawater is almost three orders of magnitude larger than that of CO_3^{2-} and the maximum Ca^{2+} variations by the formation and dissolution of $CaCO_3$ is less than 1%. Therefore $[Ca^{2+}]$ is approximately constant and with $[Ca^{2+}] \approx [Ca^{2+}]_{sat}$, Ω can be written as

$$\Omega \approx \frac{[CO_3^{2-}]}{[CO_3^{2-}]_{sat}}. \tag{1.10}$$

At values of Ω less than one, waters are undersaturated with respect to $CaCO_3$ and dissolution will occur, at values larger than one the waters are supersaturated. The interface between these two domains (where $\Omega = 1$) is called the saturation horizon.

Besides this relative measure of the saturation state, one can also focus on the absolute difference between the effective and the saturation concentration by defining

$$\Delta[CO_3^{2-}] = [CO_3^{2-}] - [CO_3^{2-}]_{sat}. \tag{1.11}$$

Using equation 1.7 and approximation 1.10, the following relations between Ω and $\Delta[CO_3^{2-}]$ can be found:

$$\Delta[CO_3^{2-}] \approx [CO_3^{2-}](1 - \frac{1}{\Omega}) \tag{1.12}$$

$$\Omega \approx \frac{1}{1 - \frac{\Delta[CO_3^{2-}]}{[CO_3^{2-}]}} \tag{1.13}$$

From this it follows that $\Omega = 1$ (value at the saturation horizon) is virtually equivalent to $\Delta[CO_3^{2-}] = 0$.

1.2.4 Controls on $[CO_3^{2-}]$ and Ω

The carbonate ion concentration can roughly be approximated by the difference

$$\begin{aligned} \text{Alk} - \text{DIC} &\approx ([HCO_3^-] + 2[CO_3^{2-}]) - ([HCO_3^-] + [CO_3^{2-}]) \\ &= [CO_3^{2-}], \end{aligned} \tag{1.14}$$

because alkalinity and dissolved inorganic carbon in sea water is mainly composed of HCO_3^- and CO_3^{2-}. The error of this approximation for the observation-based data set used in this study (see section 3.2.2) is $(21 \pm 24)\%$. Due to this relation, the distribution of $[CO_3^{2-}]$ is mainly given by the distribution of DIC and Alk.
Because the chemical equilibria associated with Alk and DIC depend on temperature and salinity, the $[CO_3^{2-}]$ distribution is also temperature and salinity dependent. Most notably, surface $[CO_3^{2-}]$ is affected by temperature due to the solubility of CO_2 in sea water, which leads to higher $[CO_3^{2-}]$ (less DIC) at low latitudes and lower concentrations (more DIC) at high latitudes. In section 3.3.1 the observed distribution of $[CO_3^{2-}]$ will be discussed.
The DIC content in the ocean also depends on the CO_2 concentration in the atmosphere. An increase in atmospheric CO_2 and the subsequent CO_2 uptake by the ocean increases DIC and lowers $[CO_3^{2-}]$ (see section 1.2.2).

Besides the pure sea water chemistry, $[CO_3^{2-}]$ is of course also affected by ocean circulation and mixing, as well as by biology. As we have seen in section 1.2.1, alkalinity and DIC both are affected by the biological pumps, but in different proportions (table 1.2.4). The remineralization of an amount of organic matter that increases DIC by 1 mol, decreases alkalinity by $\frac{N}{C} = \frac{16}{117} = 0.14$ mol, due to the oxidation of organic nitrogen to nitrate (supply of H^+ ions that decrease Alk). This follows from equation 1.5 and from the N:C Redfield-ratio, that describes the stoichiometry of the remineralization of organic matter below 400 m (equation 1.2).
On the other hand the dissolution of 1 mol $CaCO_3$ increases DIC by 1 mol and alkalinity by 2 mol (equation 1.9). Hence, the net effect of the two biological pumps on $[CO_3^{2-}]$ depends on the ratio of the remineralization of organic matter to the dissolution of $CaCO_3$.
Because of this competitive relation, $[CO_3^{2-}]$ tends to be low where the influence of remineralized organic matter is dominant. This is mainly the case for nutrient rich surface waters,

Process	Alk change	DIC change	$[CO_3^{2-}]$ change
Organic matter remineralization:	-0.14 mol	+1 mol	-1.14 mol
$CaCO_3$ dissolution:	+2 mol	+1 mol	+1 mol

Table 1.2: The effect of the biological pumps (organic matter and $CaCO_3$ cycling) on alkalinity, DIC, and carbonate ion concentration. The net effect on $[CO_3^{2-}]$ depends on the relative strength of the two pumps.

as organic matter is being remineralized at depths of a few 100 m, whereas the dissolution of $CaCO_3$ occurs at depth of some 1000 m.

We have already seen that $[Ca^{2+}]$ is nearly constant in the ocean and therefore the calcium carbonate saturation state Ω is mainly controlled by $[CO_3^{2-}]$ and the apparent solubility product $K_{\rm sp}$ (eq. 1.7). Mucci [1983] has empirically determined equations for $K_{\rm sp}$ of calcite and aragonite for a total pressure of 1 atm:

$$\begin{aligned}\log_{10}(K_{\rm sp,calcite}) &= -171.9065 + \frac{2839.319}{T} + 71.595\log_{10}(T) - 0.077993T + \\ &\quad (-0.77712 + \frac{178.34}{T} + 0.0028426T)S^{1/2} - 0.07711S + 0.0041249S^{3/2} \qquad (1.15)\\ \log_{10}(K_{\rm sp,aragonite}) &= -171.945 + \frac{2903.293}{T} + 71.595\log_{10}(T) - 0.077993T + \\ &\quad (-0.068393 + \frac{88.135}{T} + 0.0017276T)S^{1/2} - 0.10018S + 0.0059415S^{3/2}, \qquad (1.16)\end{aligned}$$

where $K_{\rm sp}$ is given in $\frac{\rm mol}{\rm kg\ soln}$, the temperature T in K, and the salinity S in PSU. From this, it follows that Ω depends non-linearly on T and S. The solubility of $CaCO_3$ increases with higher salinity. At constant salinity and pressure, $K_{\rm sp}$ increases slightly for low temperatures and declines with higher temperatures (figure 1.2). The temperature where the maximum solubility at constant salinity is reached, increases with higher salinity from about -5 to 5 °C for aragonite and from about 0 to 20 °C for calcite. Hence Ω is generally larger at higher temperatures (i.e. surface waters of low latitudes), than in colder regions with similar salinity and carbonate ion concentrations.

The effect of pressure on the dissociation constants (K_i) can be made from equations of the form

$$\ln(\frac{K_i^P}{K_i^0}) = -\frac{\Delta V_i}{RT}P = \frac{0.5\Delta\kappa_i}{RT}P^2, \qquad (1.17)$$

where P is the applied pressure in bars, $R = 83.131\frac{\rm mol\ bar}{\rm °C}$ the gas constant, T the temperature in K, and ΔV_i and $\Delta\kappa_i$ are the molal volume and compressibility change for the association and dissociation reactions [Millero, 1979]. The effect of pressure on the solubility of calcite and aragonite has been determined from measurements of Ingle [1975]:

$$\begin{aligned}\Delta V_{\rm calcite} &= -48.76 - 0.5304\ T_C \qquad (1.18)\\ \Delta\kappa_{\rm calcite} &= -11.76\cdot10^{-3} - 0.3692\cdot10^{-3}\ T_C \qquad (1.19)\\ \Delta V_{\rm aragonite} &= -46.00 - 0.5304\ T_C \qquad (1.20)\\ \Delta\kappa_{\rm aragonite} &= -11.76\cdot10^{-3} - 0.3692\cdot10^{-3}\ T_C, \qquad (1.21)\end{aligned}$$

where T_C is the temperature in °C. The solubility constant increases rapidly with increasing pressure (figure 1.2).

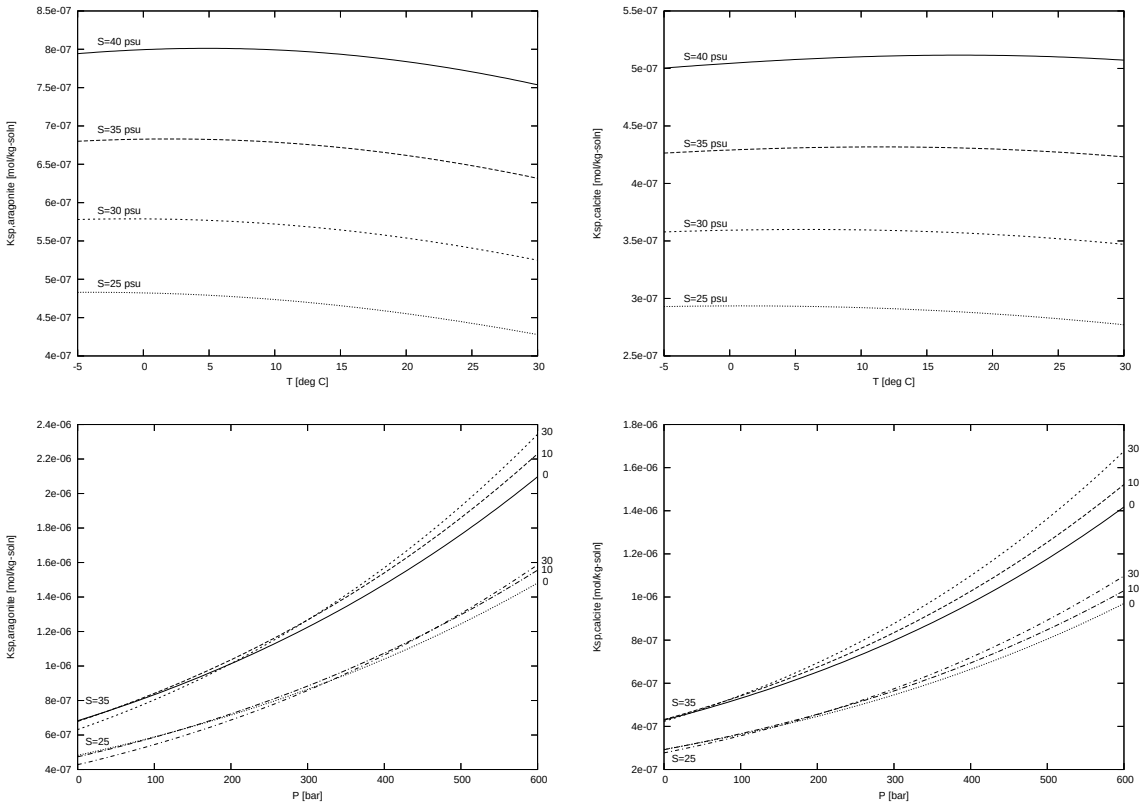

Figure 1.2: Temperature, salinity and pressure effects on calcite and aragonite solubility constants.
Top row: Temperature effect on K_{sp} for aragonite (left) and calcite (right) with salinity $S = 25, 30, 35, 40$ and a total pressure of 1 atm.
Bottom row: Pressure effect on K_{sp} for aragonite (left) and calcite (right) at temperatures $T = 0, 10, 30$ °C. The upper three curves show the relationship for salinity $S = 35$ psu, and the lower for $S = 25$ psu.

Chapter 2

The NCAR CSM1.4-carbon climate model

This work is based on simulations that were performed with the CSM1.4-carbon climate model. This fully coupled 3-D climate model was developed by the National Center for Atmospheric Research (NCAR) in Boulder, USA, and is based on the framework of the Community Climate System Model (CCSM) project [Blackmon et al., 2001].
The core of the model is a modified version of the NCAR CSM1.4 coupled physical model, consisting of ocean, atmosphere, land and sea-ice physical components integrated via a flux coupler without flux adjustments [Boville and Gent, 1998].
The CSM1.4-carbon source code is available electronically[1] and described in detail in Doney et al. [2006] and Fung et al. [2005]. Further information can also be found at the NCAR Community Climate System Model web site[2].

Some technical aspects of running the CSM1.4-carbon model are included in appendix A.

2.1 The physical model

The atmospheric model CCM3 is run with a spectral truncation resolution of 3.75° (T31 grid) and 18 levels in the vertical [Kiehl et al., 1998]. The 3-D atmospheric CO_2 distribution is advected and mixed as a dry-air mixing ratio using a semi-Lagrangian advection scheme. Both, dry and moist turbulent mixing schemes are used for the transport of water vapor mass fractions. The model CO_2 field affects the shortwave and long wave radiative fluxes through the column average CO_2 concentration.
The ocean model is the NCAR CSM Ocean Model (NCOM) with 25 levels in the vertical and a resolution of 3.6° in longitude and 0.8° to 1.8° in latitude (T31x3 grid) [Gent et al., 1998]. The water cycle is closed through a river runoff scheme, and modifications have been made to the ocean's horizontal and vertical diffusivity and viscosity from the original version (CSM1.0) to improve the equatorial ocean circulation and interannual variability. The sea ice component model runs at the same resolution as the ocean model, and the land surface model runs at the same resolution as the atmospheric model.

[1] http://www.ccsm.ucar.edu/working_groups/Biogeo/csm1_bgc/
[2] http://www.ccsm.ucar.edu/models/ccsm1.4/

2.2 The biogeochemical model

The CSM1.4-carbon model combines the NCAR Land Surface Model (LSM) [Bonan, 1996] with the Carnegie-Ames-Stanford Approach (CASA) biogeochemical model [Randerson et al., 1997]. The land surface is characterized by the fractional coverage of 14 plant functional types (PFTs) and 3 soil textures. The net primary productivity (NPP) is assumed to be 50% of the gross primary productivity (GPP) calculated by LSM and allocated to three live biomass polls, namely leaf, wood and roots. Additionally there are 9 dead carbon pools with leaf mortality contributing to surface litter, root mortality contributing to soil litter and wood mortality contributing to coarse woody debris. The subsequent decomposition by microbes leads to transfer of carbon to the dead surface and soil microbial pools and to the slow and passive pools. Other land surface processes that affect atmosphere-biosphere interactions (e.g. explicit nitrogen cycle, fires, dynamic vegetation change or anthropogenic land cover change) are not included in this implementation.

2.2.1 The biogeochemical ocean model

The ocean carbon-cycle model is a derivative of the OCMIP-2[3] biotic carbon model [Najjar et al., 1992]. The primary differences between this model and the OCMIP-2 biogeochemical model are that the biological source-sink term has been changed from a restoring formulation to a prognostic formulation, iron has been added as a limiting nutrient, and a parametrization for the iron cycle has been introduced [Doney et al., 2006]. The prognostic variables transported in the ocean model are phosphate (PO_4), total dissolved inorganic Fe, dissolved organic phosphorus (DOP), dissolved inorganic carbon (DIC), alkalinity (Alk), and oxygen (O_2).

The ocean biogeochemical model includes in simplified form the main processes of the physical-chemical carbon cycle and the organic and inorganic carbon cycle within the ocean, and air-sea CO_2 flux. It includes atmospheric dust deposition/iron dissolution, biological uptake, vertical particle transport and scavenging.
Phosphate (PO_4), dissolved organic phosphorus (DOP), dissolved inorganic carbon (DIC), and alkalinity (Alk), which are most relevant tracers for the present study, are implemented using the following conservation equations:

$$\frac{d[\mathrm{PO_4}]}{dt} = \mathcal{L}([\mathrm{PO_4}]) + J_{b,\mathrm{PO_4}} \tag{2.1}$$

$$\frac{d[\mathrm{DOP}]}{dt} = \mathcal{L}([\mathrm{DOP}]) + J_{b,\mathrm{DOP}} \tag{2.2}$$

$$\frac{d[\mathrm{DIC}]}{dt} = \mathcal{L}([\mathrm{DIC}]) + J_{b,\mathrm{DIC}} + J_{g,\mathrm{DIC}} + J_{v,\mathrm{DIC}} \tag{2.3}$$

$$\frac{d[\mathrm{Alk}]}{dt} = \mathcal{L}([\mathrm{Alk}]) + J_{b,\mathrm{Alk}} + J_{v,\mathrm{Alk}} \tag{2.4}$$

All four tracers are transported by advection, diffusion, and convection, which is represented by the 3-D transport operator $\mathcal{L}$. J_b denotes the corresponding biological source/sink terms for the tracers, which are discussed below. The equations for DIC and Alk have additional

[3]The OCMIP-2 HOWTOs are available at http://www.ipsl.jussieu.fr/OCMIP/phase2/simulations/

source/sink terms due to air-sea gas exchange of CO_2 ($J_{g,\mathrm{DIC}}$) and virtual surface fluxes due to evaporation and precipitation, as well as sea ice formation ($J_{v,\mathrm{DIC}}$ and $J_{v,\mathrm{Alk}}$). These sink/source terms (J_g and J_v) are added only as surface boundary conditions and are equivalent to the corresponding fluxes, divided by the surface layer thickness.

The CSM1.4-carbon model implements four fluxes of carbon between the ocean and other reservoirs (figure 2.1); the fluxes from the atmosphere to the ocean (F_{gAO}) and vice versa (F_{gOA}) by gas exchange, as well as the virtual fluxes ice-ocean (F_{vICE}) and ocean-atmosphere due to precipitation and evaporation (F_{vPE}). The virtual carbon fluxes approximate the effect of precipitation and evaporation and of ice formation and melting on local DIC and Alk concentrations. These virtual fluxes are used, because the model has a rigid lid (fixed ocean surface) and the surface flux of water in the real world is replaced by the surface flux of salt in the model.
When forced with historic CO_2 emission data, the net total uptake of carbon by the ocean in this model is 1.75 GtC/yr for years 1980-1989 and 2.01 GtC/yr for years 1990-1999. This compares with 1.8±0.8 PgC yr^{-1} and 1.9±0.7 PgC yr^{-1} estimated by Le Quéré et al. [2003], and 1.7±0.6 PgC yr^{-1} and 2.4±0.7 PgC yr^{-1} estimated by Plattner et al. [2002]. The global uptake is almost entirely determined by the difference between F_{gAO} and F_{gOA}, because the virtual fluxes from ice and to the atmosphere by precipitation-evaporation nearly compensate each other.

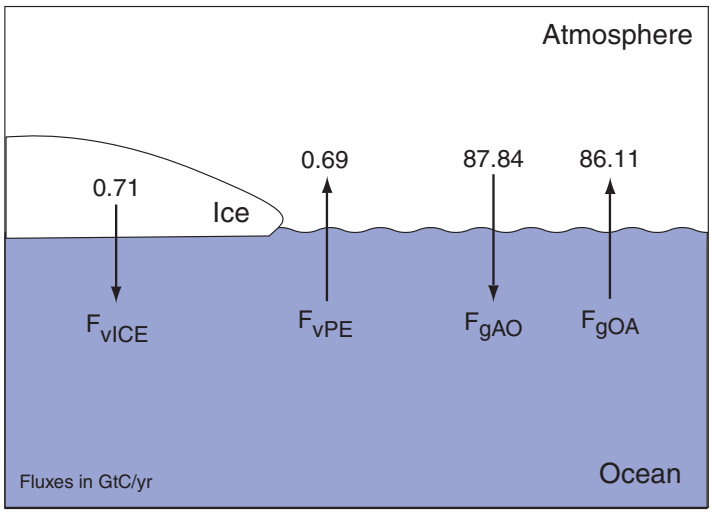

Figure 2.1: Carbon fluxes from and to the ocean component of the CSM1.4-carbon model: Gas exchange with the atmosphere (F_{gAO} and F_{gOA}), virtual precipitation-evaporation flux to atmosphere (F_{vPE}), and virtual flux from ice (F_{vICE}). The figures specify the fluxes in GtC/yr for the years 1980-1989, based on a simulation with historical CO_2 emission data. The net uptake by the ocean as a result of gas exchange is 1.73 GtC/yr and the net total uptake yields to 1.75 GtC/yr.

New/export production is computed prognostically as the turnover of biomass, modulated by temperature, surface solar irradiance and macro- and micronutrients. Phosphate was chosen instead of nitrate as the basic currency of the model so as to avoid the complexities of nitrogen fixation and denitrification. In the productive zone above the compensation depth (z_c = 75 m), PO_4 is turned into dissolved (DOP) and particulate (POP) organic matter by organisms. In this model, a fixed fraction $\sigma = 0.67$ of the production is DOP and the rest

is POP. DOP is left where the production takes place, whereas POP is exported instantly to the compensation depth. Including the remineralization of DOP and POP back to PO_4, the source/sink terms for PO_4 and DOP are

$$J_{b,\mathrm{PO_4}} = \begin{cases} -J_{\mathrm{prod}} + \kappa[\mathrm{DOP}] & (z < z_c) \\ -\frac{\partial F}{\partial z} + \kappa[\mathrm{DOP}] & (z > z_c) \end{cases} \tag{2.5}$$

$$J_{b,\mathrm{DOP}} = \begin{cases} \sigma J_{\mathrm{prod}} - \kappa[\mathrm{DOP}] & (z < z_c) \\ -\kappa[\mathrm{DOP}] & (z > z_c). \end{cases} \tag{2.6}$$

J_{prod} is the turnover of biomass described below, $\kappa = 2\ \mathrm{yr}^{-1}$ is the consumption rate constant for semi-labile organic matter, that characterizes the remineralization of DOP, and $F(z)$ is the downward flux of POP, which decreases with depth due to remineralization following a power law relationship

$$F(z) = F_c(\frac{z}{z_c})^{-a}, \tag{2.7}$$

for $z > z_c$. The exponent $a = 0.9$ was chosen based on data from sediment traps and F_c is the downward flux of POP at the compensation depth:

$$F_c = (1 - \sigma) \int_0^{z_c} J_{\mathrm{prod}} dz \tag{2.8}$$

The production term is calculated as

$$J_{\mathrm{prod}} = F_T\ F_N\ F_I\ B\ \max(1, \frac{z_{\mathrm{ML}}}{z_c})\ \frac{1}{\tau}, \tag{2.9}$$

where F_T, F_N, and F_I are the limiting factors with respect to temperature, nutrients and light, B is a proxy for biomass, and $\tau = 15$ days is the optimal uptake timescale, which differs form the OCMIP-2 protocol, where $\tau = 30$ days. The mixed layer scaling factor $\max(1, \frac{z_{\mathrm{ML}}}{z_c})$ scales up the production in the entire water column above z_c, if the mixed layer depth z_{ML} exceeds the compensation depth, in order to account for the production that would take place in the mixed layer below z_c.
The limitation factors and the biomass proxy are defined as

$$F_T = \frac{T + 2}{T + 10} \tag{2.10}$$

$$F_N = \min(\frac{[\mathrm{PO_4}]}{[\mathrm{PO_4}] + \kappa_{\mathrm{PO_4}}}, \frac{[\mathrm{Fe}]}{[\mathrm{Fe}] + \kappa_{\mathrm{Fe}}}) \tag{2.11}$$

$$F_I = \frac{I}{I + \kappa_I} \tag{2.12}$$

$$B = \min([\mathrm{PO_4}], \frac{[\mathrm{Fe}]}{r_{\mathrm{Fe:P}}}), \tag{2.13}$$

where T is the temperature in °C, $\kappa_{\mathrm{PO_4}} = 0.05\ \mu$mol/l, $\kappa_{\mathrm{Fe}} = 0.03$ nmol/l, and $\kappa_I = 20\ \mathrm{W/m^2}$ are the half-saturation values for the corresponding Michaelis-Menten terms, and $r_{\mathrm{Fe:P}} = 117 \cdot 5 \cdot 10^{-6}$ is the Redfield Fe:P ratio. Figure 2.2 shows the characteristics of the limitation factors.
The short wave irradiance I decays exponentially from the surface with 20 m depth-scale ($I(z) = I_0 \mathrm{e}^{\frac{z}{20\ \mathrm{m}}}$). The amount of energy that is deposited above the mixed layer depth is

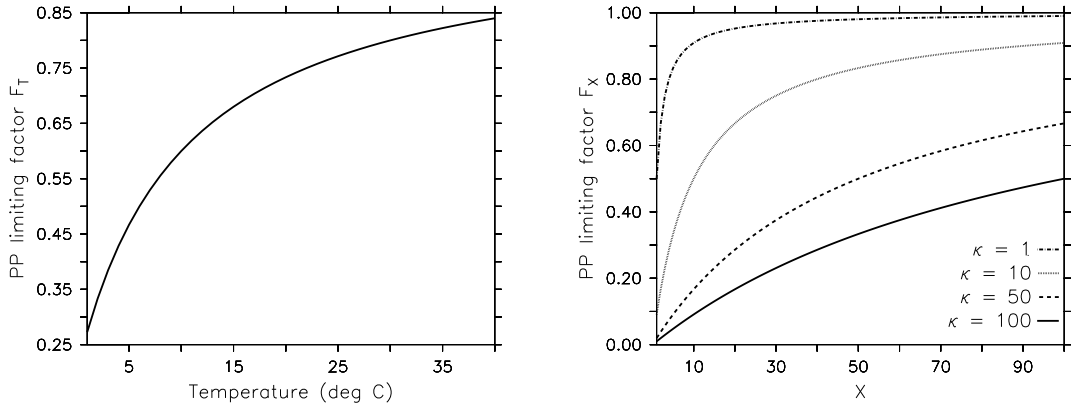

Figure 2.2: Characteristics of the temperature limiting factor F_T (left) and the generic Michaelis-Menten limiting term F_X (right) for different half-saturation values κ (1%, 10%, 50%, and 100% of the maximum displayed value of X), as it is used for nutrient and light limitation.

averaged over the entire mixed layer and is available homogeneously in the water column above z_c. Therefore, the light limitation factor in a water parcel depends on the mixed layer depth of the corresponding water column. Minimum light limitation for a given irradiance at the surface is attained when the mixed layer depth is near the compensation depth. If the mixed layer exceeds the production zone, the available light above z_c is reduced. This effect is compensated by the mixed layer scaling factor described above. Figure 2.3 shows the relation between the light limitation and the mixed layer scaling factor.

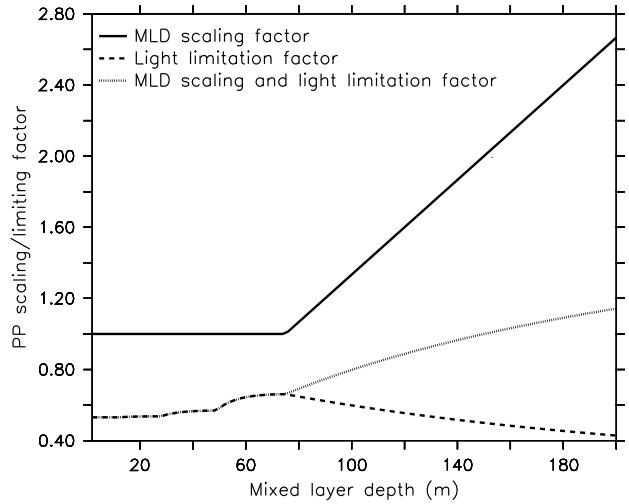

Figure 2.3: The mixed layer scaling factor (solid line) and the light limitation factor F_I (dashed) as functions of the mixed layer depth. The light limitation factor is calculated with a surface short wave irradiance of 150 W/m^2 and the average over the compensation depth z_c is shown. The dotted line shows the combined effect of the two factors. The odd shape of the light limitation curve below $z_c = 75$m is due to discretization effects that exist because the production zone is divided into four layers with boundaries at 12 m, 28 m, 49 m, and 76 m.

DIC and Alk cycles are linked to phosphate and calcium cycling by the source/sink terms

$$J_{b,\mathrm{DIC}} = r_{\mathrm{C:P}}\ J_{b,\mathrm{PO_4}} + J_{b,\mathrm{Ca}} \tag{2.14}$$

$$J_{b,\mathrm{Alk}} = -r_{\mathrm{N:P}}\ J_{b,\mathrm{PO_4}} + 2\ J_{b,\mathrm{Ca}}, \tag{2.15}$$

where $r_{\mathrm{C:P}} = 117$ and $r_{\mathrm{N:P}} = 16$ are the carbon to phosphorus and nitrogen to phosphorus Redfield ratios, and

$$J_{b,\mathrm{Ca}} = \begin{cases} -R\ r_{\mathrm{C:P}}\ (1-\sigma) J_{\mathrm{prod}} & (z < z_c) \\ -\frac{\partial F_{\mathrm{Ca}}}{\partial z} & (z > z_c) \end{cases} \tag{2.16}$$

is the source/sink term of dissolved calcium. The formation of calcium carbonate in surface waters is linked to the POC production $(1-\sigma)J_{\mathrm{prod}}$ by the so-called rain-ratio $R = 0.07$, that defines the molar ratio of the downward POC flux to the downward $CaCO_3$ flux at the compensation depth. Below z_c, the $CaCO_3$ flux F_{Ca} is assumed to decrease exponentially

$$F_{\mathrm{Ca}}(z) = R\ r_{\mathrm{C:P}}\ F_c\ \mathrm{e}^{\frac{-(z-z_c)}{d}}, \tag{2.17}$$

with a depth scale $d = 3500$ m. No sediment model is included and, as with POC, any flux of $CaCO_3$ reaching the sea floor is assumed to dissolve there instantaneously and diffuse back into the water column.

2.3 Simulations

2.3.1 The experimental setup

To initialize the model, a sequential spin-up procedure including a 1000 year fully coupled control run was employed by Doney et al. [2006]. Starting from this nearly steady state initial conditions, a simulation with prescribed historic fossil fuel and land use CO_2 emissions was performed from 1820 to 2000, as well as two continuative emission scenario simulations from 2000 to 2100 (SRES-A2 and SRES-B1). Figure 2.4 shows the prescribed fossil fuel and land use emissions from 1820-2100 for these simulations, as well as the simulated atmospheric CO_2 concentration at the ocean surface in response to these emissions.

Besides these CO_2 emissions, observation-based time histories of solar irradiance [Wang et al., 2005], spatially explicit aerosol loading from explosive volcanism [Ammann et al., 2003], non-CO_2 greenhouse gases methane (CH_4), nitrous oxide (N_2O), chlorofluorocarbons (CFC-11 and CFC-12), other halogenated species, sulfur hexafluoride (SF6), and anthropogenic sulfate aerosols with a recurring annual cycle of ozone and natural sulfate aerosol have also been included [Joos et al., 2001, Ammann et al., 2007]. The volcanic forcing was established by converting ice core aerosol proxies to meridionally and temporally varying atmospheric aerosol fields following Ammann et al. [2003]. Volcanic aerosols were specified as a single aerosol size distribution, and optical depth was scaled linearly with the aerosol loading. Atmospheric CH_4, N_2O, CFCs and other halogenated species concentrations were individually prescribed following ice core measurements and direct atmospheric observations. The effect of variations in orbital parameters, which vary very slowly, have not been considered.
In the scenario simulations from 2000 to 2100, the solar irradiance is set to be constant (1366.12 W/m^2) and no fictive volcanic eruptions are assumed over this century.

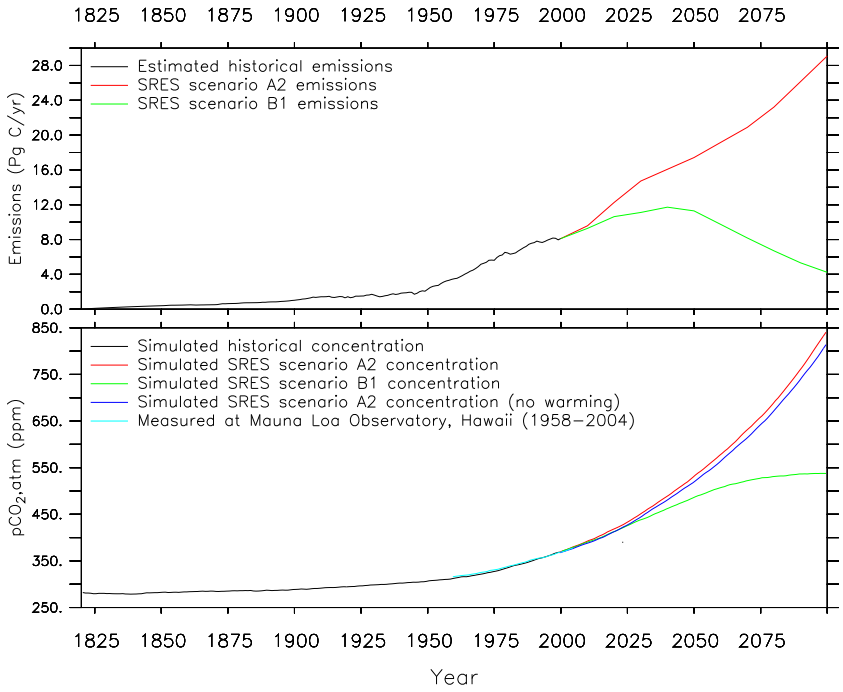

Figure 2.4: Top: Prescribed fossil fuel and land use CO_2 emissions (PgC/yr = GtC/yr) based on historical data (1820-2000) and the SRES-A2/B1 scenarios (2000-2100). Bottom: Simulated atmospheric global annual mean CO_2 concentrations (ppm) at the ocean surface resulting from the corresponding emissions. The blue line indicates the concentrations in the SRES A2 simulation without radiative forcing and the cyan line shows annual mean concentrations observed at Mauna Loa Observatory, Hawaii from 1958 to 2004 [Keeling and Whorf, 2005].

Additionally, another simulation based on the SRES-A2 emission scenario has been performed, in which the radiative forcing of CO_2 and the other factors described above were disabled. This means that in this simulation the CO_2 concentrations increase and CO_2 is transported like in the other simulations, but no warming due to radiative forcing in the atmosphere occurs.

2.3.2 The SRES emission scenarios

The SRES-A2 and SRES-B1 scenarios are two of six illustrative scenarios of the set of emission scenarios in the Special Report on Emission Scenarios (SRES) published by the Intergovernmental Panel on Climate Change (IPCC) in 2000 [IPCC, 2000]. These scenarios were developed between 1996 and 1999 based on different models and story lines that represent demographic, social, economic, technological, and environmental developments. The A2 scenario assumes a heterogeneous world with high population, high energy use, low economic growth in developing countries, medium economic growth in industrialized countries, and slow technology development that is balanced with respect to fossil/non-fossil energy. Whereas the B1 scenario describes a convergent world with a global population, that peaks in mid-century and declines thereafter. Rapid changes in economic structures towards a service and information economy are assumed, with reductions in material intensity and the introduction of clean and resource-efficient technologies. The emphasis in B1 is on global solutions to economic,

social and environmental sustainability, including improved equity, but without additional climate initiatives.

Recently Van Vuuren and O'Neill [2006] investigated the consistency of the IPCC SRES scenarios with available 1990-2000 data and recent projections. They found that the SRES assumptions for 1990-2000 are reasonably consistent with available data as well as with current near-term projections. Although the range of population and economic projections has shifted downwards since SRES publication and the A2 scenario population is significantly higher than the high end of the current range of projections, the SRES scenarios still seem to be fully consistent with the current range of more recent outlooks in terms of emissions.

2.3.3 Control run and model trend

In order to verify that the initial state of the model is a steady state, a control run over 480 years (1820-2300) has been performed. Unfortunately, several variables are not constant in the long-term average, but exhibit a slight trend. In order to remove the model drift, this trend was subtracted from the simulation results using a spline function with a cut-off period of 1000 years. This approach implies that the model drift is independent of the actual state, i.e. the actual values of the variables. This is possibly not true, but as long as the drift is small enough compared to the simulated changes, it is an appropriate approximation. The following variables used for this study have been detrended in the manner described above: Alk, DIC, Fe, PO_4, S, and T. The differences between different computing platforms are discussed in appendix A.3.

Chapter 3

Ocean acidification

3.1 Introduction

Atmospheric carbon dioxide concentration is increasing and expected to reach double preindustrial levels within the next 50-60 years in response to anthropogenic emissions. Carbon dioxide is well-known as the most important anthropogenic greenhouse gas, that contributes a large amount (about 1.7 W/m^2 in 2005) to the global radiative forcing and to the expected global warming ranging between 1.1°C to 6.4°C within this century [IPCC, 2007].

Besides global warming, there are also other effects related to increasing atmospheric CO_2 concentrations that need to be considered when discussing climate change. Currently only about 50% of CO_2 emitted to the atmosphere remains airbone; the other half is taken up by the ocean and terrestrial biosphere. [Manning and Keeling, 2006] estimate that about a third of the carbon dioxide released ends up in the ocean. This leads to a direct geochemical effect, frequently denoted by the term "ocean acidification", which refers to the decrease in pH of seawater due to the uptake of carbon dioxide. The shift in ocean chemistry is expected to have a major impact on calcifying organisms, such as corals and some plankton. Those organisms play important roles in the marine ecosystem and it is crucial to understand the underlying mechanisms, in order to evaluate possible impacts.

This chapter provides results on ocean acidification from simulations performed with the coupled climate-carbon cycle model CSM1.4-carbon. After a short overview of the methods used, model results are compared with present-day observations in order to evaluate the model's ability to reproduce observed geochemical tracer distributions. Then, the projected changes until 2100 are presented, followed by the discussion of sensitivity analysis and uncertainties. Last, the main results and possible consequences are discussed and compared to related work.

Constant definition	*Description*	*References*
$K_0 = \frac{[CO_2]}{f_{CO_2}}$	Solubility of CO_2	Weiss (1974)
$K_1 = \frac{[H][HCO_3]}{[H_2CO_3]}$	Dissociation of carbonic acid	Lueker et al. [2000]
$K_2 = \frac{[H][CO_3]}{[HCO_3]}$		
$K_b = \frac{[H][BO_2]}{[HBO_2]}$	Dissociation of boric acid	Dickson (1990)
$K_{p1} = \frac{[H][H_2PO_4]}{[H_3PO_4]}$	Dissociation of phosphoric acid	DOE (1994), Millero (1974)
$K_{p2} = \frac{[H][HPO_4]}{[H_2PO_4]}$		
$K_{p3} = \frac{[H][PO_4]}{[HPO_4]}$		
$K_{si} = \frac{[H][SiO(OH)_3]}{[Si(OH)_4]}$	Dissociation of silicic acid	Yao and Millero (1995)
$K_w = [H][OH]$	Dissociation of water	Dickson and Riley (1979)
$K_s = \frac{[H][SO_4]}{[HSO_4]}$	Dissociation of HSO_4^-	Dickson (1990)
$K_f = \frac{[H][F]}{[HF]}$	Dissociation of hydrofluoric acid	Dickson and Riley (1979)
$K_{spc} = [Ca]_{sat,c}\ [CO_3]_{sat,c}$	Apparent solubility of calcite	Mucci [1983] (eq. 1.15
$K_{spa} = [Ca]_{sat,a}\ [CO_3]_{sat,a}$	Apparent solubility of aragonite	and 1.16)

Table 3.1: Solubility and dissociation constants of different compounds in seawater that were used to calculate the carbonate concentration according to Millero [1995].

3.2 Methods

3.2.1 Calculation of the ocean carbonate chemistry

Since the carbonate ion concentration and the corresponding saturation states are not output fields of the CSM1.4-carbon model, they have to be calculated offline from other modeled or observed quantities. This was done using the chemistry routines from the OCMIP-3/NOCES project[1]. These routines, originally by Dickson [2002], contain empirical formulas that mainly can be found in Millero [1995], but have been changed to total pH scale [Lueker et al., 2000] instead of seawater pH scale.
The calculation comprises basically the following three steps:

1. Calculation of a set of 13 solubility and dissociation constants K_i (table 3.1), that characterize the series of chemical equilibria described in section 1.2.3. All these constants are functions of temperature T and salinity S; $K_i = f(T, S)$.

2. Correction of these constants to take the pressure effect into account, according to Millero [1979] (eq. 1.17 - 1.21); $K_i' = f(T, p, K_i)$.

3. Calculation of the carbonate ion concentration $[CO_3^{2-}]$ and the saturation states $\Omega_{A/C}$, which all are functions of dissolved inorganic carbon (DIC), alkalinity, silicate, phosphate and the dissociation constants, according to Millero [1995];
$f(\mathrm{DIC}, \mathrm{Alk}, [SiO_3^{2-}], [PO_4^{3-}], K_i')$.

Table 3.2 summarizes the input and output variables of the calculations described above. The output variables are the basis for the further analysis. Input data are either taken from output of the CSM1.4-carbon model or from observations, except for the pressure.

[1] http://www.ipsl.jussieu.fr/OCMIP/phase3/simulations/NOCES/HOWTO-NOCES.html

Input variables		
Temperature	T	[°C]
Pressure	p	[bar]
Salinity	S	[psu]
Alkalinity	Alk	[mol/m^3]
DIC	DIC	[mol/m^3]
Silicate	[SiO_3^{2-}]	[mol/m^3]
Phosphate	[PO_4^{3-}]	[mol/m^3]
Output variables		
Carbonate	[CO_3^{2-}]	[mol/m^3]
Saturation state (aragonite)	Ω_A	[1]
Saturation state (calcite)	Ω_C	[1]
pH-value	pH	[1]

Table 3.2: Input and output variables with symbolic names and units used for the calculation of the investigated quantities.

For this application it seemed appropriate to use a simple approach to calculate the pressure. Therefore it has been calculated as hydrostatic pressure that depends only on the depth z

$$p(z) = \rho g z + p_0, \tag{3.1}$$

where $\rho = 1028 \frac{\text{kg}}{\text{m}^3}$ is the mean density of seawater, $g = 9.80665 \frac{\text{m}}{\text{s}^2}$ the gravitational constant and $p_0 = 1.01325$ bar the average atmospheric pressure at sea level.
Silicate concentrations have always been taken from observation based data, also for the calculation of simulated results, because the model output does not contain silicate fields.
$\Delta[CO_3^{2-}]$ has been calculated from the output variables Ω and $[CO_3^{2-}]$ according to equation 1.12.

3.2.2 Sources of measurements

To compare the model results with observations, measurements from the Global Data Analysis Project (GLODAP) [Key et al., 2004] and the World Ocean Atlas 2001 (WOA01) [Conkright et al., 2002] were used. The GLODAP data set contains measurements of DIC and alkalinity performed on cruises in the Atlantic, Pacific, Indian and Southern Ocean over the decade of the 1990s. The World Ocean Atlas 2001 contains objectively analyzed fields of several commonly measured ocean variables like temperature, salinity, phosphate and silicate.

It was necessary to remap the GLODAP and WOA01 data sets to the model grid, in order to compare the measurements and derived variables ($[CO_3^{2-}]$, Ω_A, Ω_C) to the model output. This was done by multi-axis linear interpolation with FERRET[2]. The model grid is coarser than the one used by GLODAP and WOA01 and there is no benefit from regridding the model output to a finer grid.

The observation based carbonate variables were computed for each month, which corresponds to the time resolution of the model output. At depths where no data were available at this

[2]http://ferret.pmel.noaa.gov/

Variable	*Source*	$z = 0 - 500$ m	$z = 500 - 1500$ m	$z = 1500 - 5750$ m
Alkalinity	GLODAP	annual means	annual means	annual means
DIC	GLODAP	annual means	annual means	annual means
Temperature	WOA01	monthly means	monthly means	seasonal means
Salinity	WOA01	monthly means	monthly means	seasonal means
Silicate	WOA01	monthly means	annual means	annual means
Phosphate	WOA01	monthly means	annual means	annual means

Table 3.3: Composition of the data set used to calculate the observation based carbonate ion concentration. At different depths, variables from different climatological periods were used, depending on their availability.

time resolution, the missing values were filled with seasonal or annual means. Table 3.3 shows the compilation of the variables from GLODAP and WOA01 for different depths.
From the model output (and the silicate fields from WOA01), the carbonate variables were computed for each month from 1990 to 1999. This time is assumed to correspond with the observations from WOA01 and GLODAP.
The comparison between model and observation based variables was then done using annual means. A comparison of seasonal variability is not possible, because GLODAP provides only annual mean data for alkalinity and DIC.

Preindustrial DIC concentrations can be estimated by subtracting estimates of anthropogenic CO_2 in the ocean from the measured DIC concentration. In GLODAP, anthropogenic CO_2 has been estimated using the $\Delta C^\star$ technique [Gruber et al., 1996]. This technique separates the preformed[3] DIC into an equilibrium component that can be calculated from thermodynamics, and a substantially smaller disequilibrium component:

$$\mathrm{DIC}^{(\mathrm{anth})} = \mathrm{DIC}^{(\mathrm{meas})} - \Delta\mathrm{DIC}^{(\mathrm{bio})} - \mathrm{DIC}^{(\mathrm{eq})} - \Delta\mathrm{DIC}^{(\mathrm{diseq})} \tag{3.2}$$

Where $\mathrm{DIC}^{(\mathrm{anth})}$ is the anthropogenic CO_2 concentration of a sub-surface water sample; $\mathrm{DIC}^{(\mathrm{meas})}$ is the measured DIC concentration; $\Delta\mathrm{DIC}^{(\mathrm{bio})}$ is the change in DIC as a result of biological activity (both organic carbon and $CaCO_3$ cycling); $\mathrm{DIC}^{(\mathrm{eq})}$ is the DIC of seawater (at the temperature, salinity, and preformed alkalinity of the sample) in equilibrium with a pre-industrial CO_2 partial pressure of 280 ppm; and $\Delta\mathrm{DIC}^{(\mathrm{diseq})}$ is the air-sea CO_2 disequilibrium a water parcel had when it was last in contact with the atmosphere.
The equilibrium component can be calculated explicitly for each water sample as

$$\begin{aligned}
\Delta C^\star &= \mathrm{DIC}^{(\mathrm{anth})} + \Delta\mathrm{DIC}^{(\mathrm{diseq})} \\
&= \mathrm{DIC}^{(\mathrm{meas})} - \Delta\mathrm{DIC}^{(\mathrm{bio})} - \mathrm{DIC}^{(\mathrm{eq})} \\
&= \mathrm{DIC}^{(\mathrm{meas})} - \mathrm{DIC}^{(\mathrm{eq})} + \frac{117}{170}(\mathrm{O_2} - \mathrm{O_2^{(sat)}}) - \frac{1}{2}(\mathrm{Alk} - \mathrm{Alk_0} - \frac{16}{170}(\mathrm{O_2} - \mathrm{O_2^{(sat)}})) \\
&\quad + \frac{106}{104}\mathrm{N^*_{anom}},
\end{aligned} \tag{3.3}$$

where $\mathrm{DIC}^{(\mathrm{meas})}$, Alk, and O_2 are the measured concentrations for a given water sample; $\mathrm{Alk_0}$ is the preformed alkalinity value; $\mathrm{O_2^{(sat)}}$ is the calculated oxygen saturation value that

[3]The preformed concentration of a tracer in a water parcel refers to the concentration that it had, when it left the surface, i.e. when no more gas exchange with the atmosphere occurs.

the waters would have if they were adiabatically raised to the surface; and N^*_{anom} is the net denitrification signal in the waters.
For shallow or ventilated isopycnal surfaces that contain measurable levels of chlorofluorocarbons (CFC), the disequilibrium component $\Delta DIC^{(diseq)}$ was derived from the CFC-12 corrected $\Delta C^\star$ calculation. For isopycnal surfaces located in the interior of the ocean where CFC-12 is absent and where one can reasonably assume that there is no anthropogenic CO_2, the $\Delta C^\star$ values in these waters are equal to $\Delta DIC^{(diseq)}$.

3.3 Results

3.3.1 Observation-based distribution of $[CO_3^{2-}]$

The surface aragonite saturation state Ω_A, derived from GLODAP and WOA01 data (see section 3.2.2) is shown in figure 3.4 (top panel). Maximum values (around 4) can be found in the tropics. At higher latitudes the values decrease and minimum values (around 1.25) can be found in the Southern Ocean near the coast of Antarctica.
Since the saturation concentration $[CO_3^{2-}]_{sat}$ at the surface is almost constant compared to $[CO_3^{2-}]$ (figure 3.1), this distribution is not determined by the direct influence of temperature and salinity on the $CaCO_3$ solubility, but by the in-situ concentration $[CO_3^{2-}]$, which is in turn mainly given by the difference between alkalinity and DIC concentrations. Since alkalinity is more constant, the variation of carbonate ion concentration is influenced more by variations of DIC.
The DIC concentration is linked to the cycles of organic matter (photosynthesis, respiration and remineralization) and $CaCO_3$. For example, it is high in the Southern Ocean due to transport of remineralized organic matter to the surface. Increased DIC concentrations and reduced Ω can also be found in the upwelling regions of the eastern Pacific. But DIC is also influenced by the air-sea gas flux, which is strongly temperature dependent, and therefore there is an indirect influence of temperature via DIC on the saturation state.

Until depths of 500-1000 m, the distribution of the $CaCO_3$ saturation state remains mainly determined by $[CO_3^{2-}]$ (figure 3.2), which in turn follows roughly the DIC distribution. At greater depth, the pressure dependency of $CaCO_3$ solubility plays a significant role, while the variability of alkalinity and DIC is lower than at the surface (figure 3.3). This leads to a decrease of the saturation state in the deep ocean, although the carbonate ion concentration is relatively homogeneous below 1000 m.

3.3.2 Comparison of model results with observations

In order to get an estimation of the quality of the model results, they are compared with values based on the GLODAP and WOA01 data sets.
Figure 3.4 shows the saturation state with respect to aragonite Ω_A at the surface, simulated with the CSM1.4-carbon model and calculated from the observation-based data set. In the overall picture the model matches the measured patterns and values reasonably well. The global correlation coefficient of Ω_A is 0.93, best results can be found in the Atlantic and Indian Ocean (about 0.95), whereas the top 200 m are correlated only with 0.89 (Figure 3.5).

The model represents the amplitude of variations of Ω_A well in all regions, as indicated by values of the relative standard deviation around 1.0. Absolute concentrations of $[CO_3^{2-}]$ show less good correlation coefficients (0.87 to 0.91), and in the Pacific the model results yield a smaller variance than the observation based ones.
This indicates that differences in $[CO_3^{2-}]$ are compensated partially by similar differences in $[CO_3^{2-}]_{sat}$, because of equation 1.10. This is particularly true in the Pacific, but not for the top 200 m of the global ocean. Since the saturation concentration depends only on temperature and salinity, the compensation is most likely accomplished due to differences in T and/or S.

A closer look at the differences shows that the model underestimates the surface carbonate saturation in the North Pacific, in the North Atlantic and in some regions south of Africa,

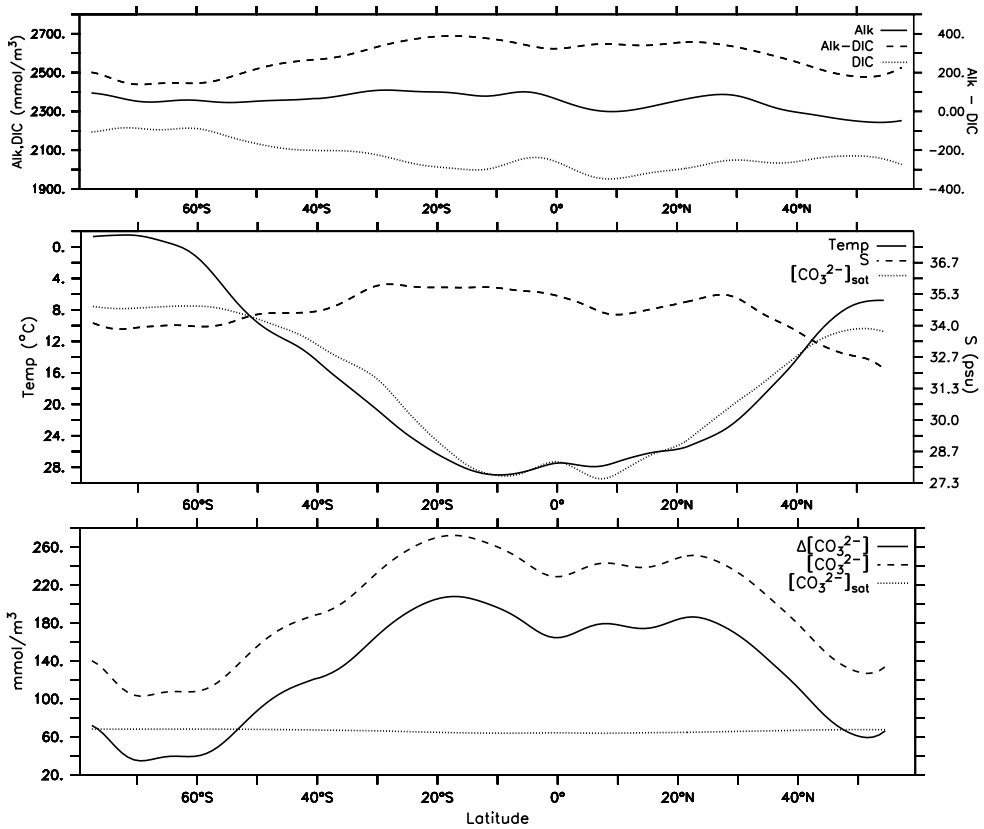

Figure 3.1: Different observation based quantities related to carbonate ion saturation in surface waters of the Pacific at 160°W (GLODAP, 1994; WOA 2001). The top panel shows surface alkalinity and DIC concentrations. The difference between these concentrations (dashed line, right axis) is an approximation for $[CO_3^{2-}]$, that is shown in the bottom panel. The middle panel shows the temperature (left axis, inverted) and salinity (right axis), that determine the solubility of $CaCO_3$ (K_{sp}) in surface waters. The dotted line (without scale; min/max 64/68 mmol/m^3) represents the saturation concentration $[CO_3^{2-}]_{sat}$ with respect to aragonite, that is also shown in the bottom panel. Because the salinity is more or less constant in many regions, the solubility is mainly influenced by temperature. $[CO_3^{2-}]_{sat}$ decreases with increasing temperature. This effect, however, is reduced or even inverted at low temperatures (see also figure 1.2). But the changes in $[CO_3^{2-}]_{sat}$ are very small compared to the changes in the in situ concentration $[CO_3^{2-}]$ (bottom panel), and the difference $\Delta[CO_3^{2-}]$ shows the same characteristics as $[CO_3^{2-}]$.

South America and New Zeeland. Regions where the modeled saturation state is somewhat too high can mainly be found between 40°N and 40°S in the Pacific and the Indian Ocean.

Between the surface and 100 m depth the underestimation in the North Pacific and North Atlantic declines, while the overestimation in the tropics increases (Figure 3.6). At 200 m the model overestimates the saturation state in almost the whole North Pacific. With greater depth the differences decrease and become very small at 1000 m except for the North Pacific, where the difference remains bigger than anywhere else.

The same pattern can also be seen in the zonal average $\Delta[CO_3^{2-}]$ of the Pacific and the Atlantic (Figure 3.7). The overestimation in the North Pacific at depths between 200 m and 1000 m is clearly visible.

The average difference between modeled and measured $\Delta[CO_3^{2-}]$ varies from 0 mmol/m^3 to 40

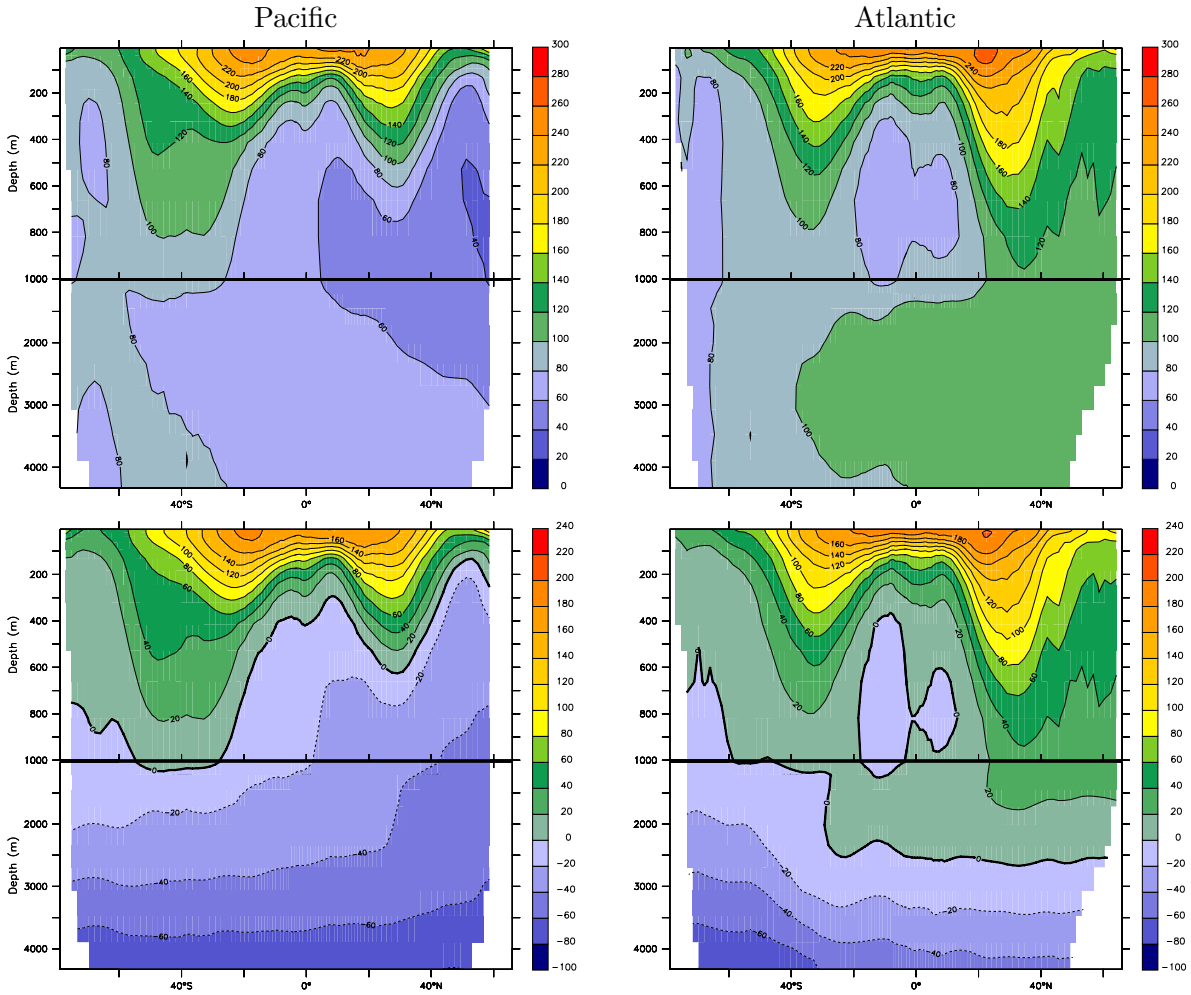

Figure 3.2: Meridional sections through the Pacific (left) and the Atlantic (right) showing zonal mean of observation-based $[CO_3^{2-}]$ (top) and $\Delta[CO_3^{2-}]$ (bottom) with respect to aragonite in mmol/m^3. The saturation horizon is indicated by the thick line at $\Delta[CO_3^{2-}] = 0$. The figures show annual mean concentrations and are based on DIC and alkalinity data from the GLODAP data set (1994).

mmol/m^3 in the Pacific and from -10 mmol/m^3 to 20 mmol/m^3 in the Atlantic. The variance of these differences depend strongly on the depth and latitude (Figure 3.8).

Most of the undersaturated water, in terms of absolute volume, can be found between 20°S and 60°S at depths of 1500-4000 m, and in the North Pacific between 2500 and 4500 m (figure 3.9). The volume of undersaturated waters differs by about 15% from the observation-based data for the decade 1990-1999. This can partly be explained with differences in the topography of the two data sets. Particularly, at depths below 3500 m the observation-based data set covers a larger volume, which yields about 1/5 of the discrepancy. Most of the difference, however, can be attributed to the too deep saturation horizon of the model results. These differences can primarily be found in the North Pacific and Southern Ocean, and lead to large differences in the volume of supersaturated waters between 500 m and 1500 m depth. Above 250 m, the model results match the observation-based data set well.

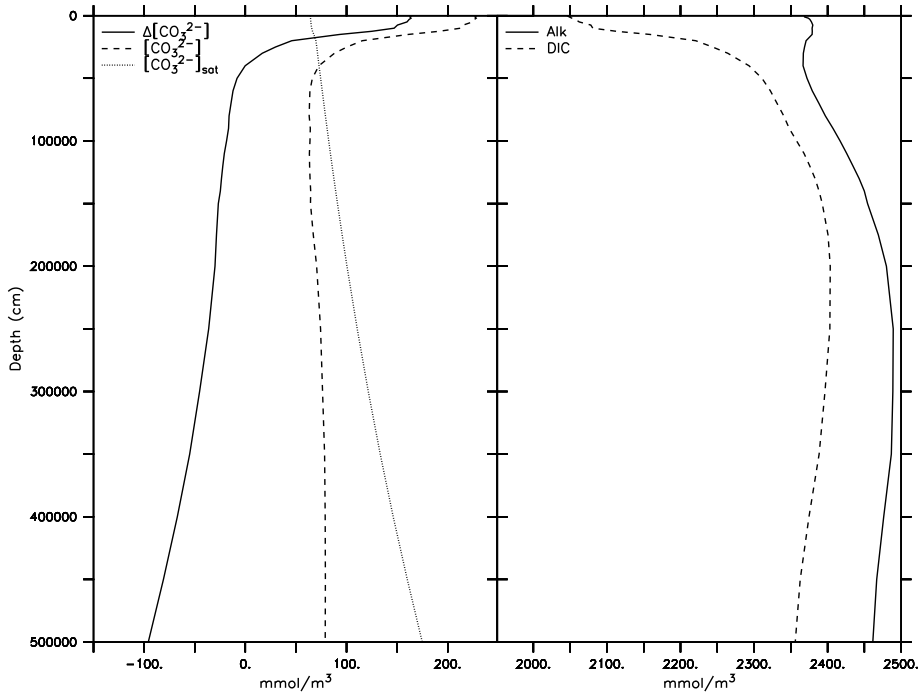

Figure 3.3: Alkalinity, DIC and carbonate ion concentrations from observations (GLODAP, 1994) in the equatorial Pacific. $[CO_3^{2-}]$ is high at the surface as the difference between alkalinity and DIC is large. Within 500 m this difference decreases rapidly, leading to minimal $[CO_3^{2-}]$ between 500 and 1500 m. Below 1500 m the carbonate ion concentration increases slightly again. The (aragonite) saturation concentration $[CO_3^{2-}]_{sat}$ increases with depth due to the pressure dependency of K_{sp} (see also figure 1.2), which leads to the decrease of $\Delta[CO_3^{2-}]$ in the deep ocean, despite more or less constant $[CO_3^{2-}]$.

The main factor responsible for these above described differences in the carbonate saturation state are differences in DIC and alkalinity, as the differences in $[CO_3^{2-}]_{sat}$ are very small ($< 1\%$ of the maximum $[CO_3^{2-}]$ difference). More precisely, it is the anomaly of the difference between alkalinity and DIC (eq. 1.14) that determines the carbonate saturation anomaly. If we eliminate the anomaly in the Alk-DIC difference by changing the value of DIC or alkalinity to match the measured difference, the carbonate saturation anomaly decreases by a factor of 10 or more.

The model shortcomings in the North Pacific are probably caused by the too low export of organic matter due to deficiencies in the ocean circulation. Oxidation of organic matter falling from surface layers releases CO_2, which in turn decreases $[CO_3^{2-}]$. This decrease is underestimated in the model due to the underestimation of export production. This is correlated with too low apparent oxygen utilization (AOU) and phosphate concentrations in the North Pacific.

The shallow layers of aragonite-undersaturated water between 20°N and 15°S at depths of 500-1000 m in the eastern tropical Atlantic are reproduced by the model, but are somewhat too extensive. The undersaturation in these layers results most likely from a combination of the uptake of anthropogenic CO_2 and the oxidation of organic matter falling from the highly productive overlying surface waters [Chung et al., 2004]. Thus the model seems to reasonably reproduce Ω_A in the Atlantic, but the export production and/or the input of anthropogenic

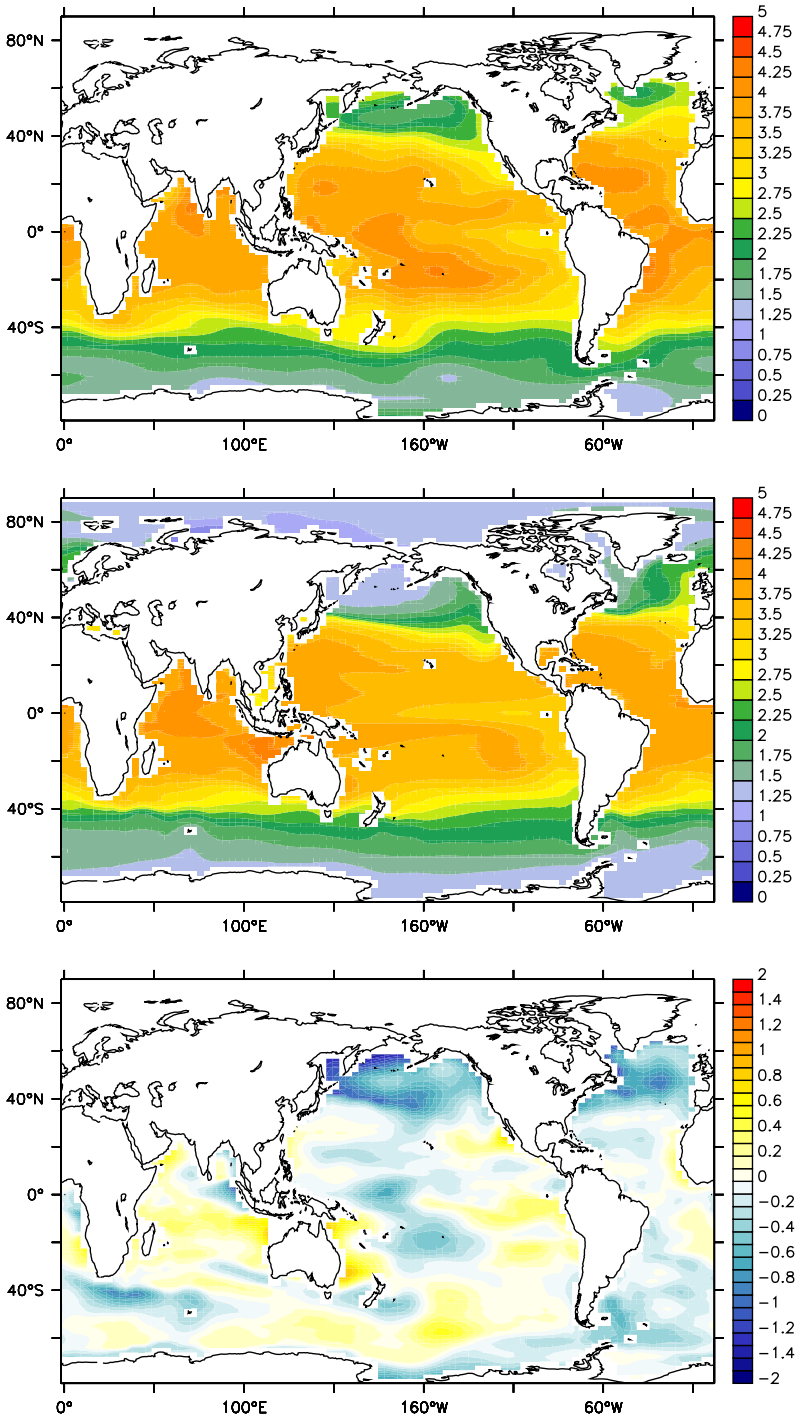

Figure 3.4: Comparison between the observed (top) and the modeled (middle) annual mean (1990-1999) aragonite saturation state at the surface. The difference plot at the bottom shows regions where the model is over- (red) or underestimating (blue) the values from measurements.

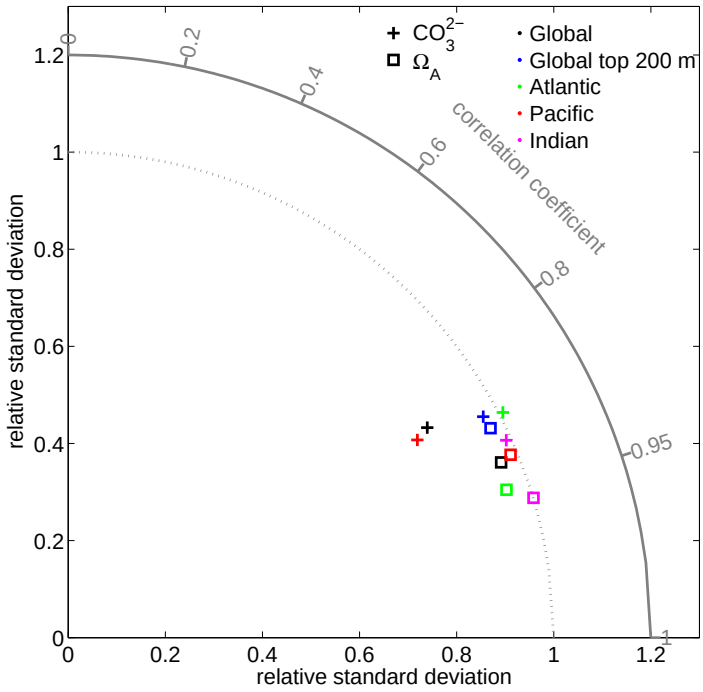

Figure 3.5: Taylor diagram conveying information about the pattern similarity between simulated and observation based results for annual mean (1990-1999) Ω_A (squares) and $[CO_3^{2-}]$ (crosses). The observed field is represented by a point at unit distance from the origin along the abscissa. The distance from this point to the other points representing simulated fields, indicates the normalized r.m.s error. The values are calculated for the entire global ocean (black), for the top 200 m of the global ocean (blue), as well as for the entire Atlantic (green), Pacific (red), and Indian Ocean (magenta).

CO_2 in the tropics is too high, possibly due to too intense upwelling.

For the Arctic Ocean there are no observation data available from GLODAP, but a qualitative comparison with data from the Arctic Ocean Section 94 (AOS94) and the Polarstern Arctic '96 expedition (ACSYS 96) [Jutterström and Anderson, 2005] shows, that the model results match the measured aragonite saturation state at the surface reasonably well. In particular, the low Ω_A-values at the shelf break depth seem to be well reproduced by the model (figure 3.10). These low saturation states are correlated with nutrient maxima and very low O_2 concentrations, that suggest remineralization of organic matter. At depths below 500 m, the model overestimates Ω_A by about 25%, and consequently the depth of the aragonite saturation horizon is about 3500 m, instead of the observed 2500 m.

3.3.3 Projected changes in carbonate saturation state until 2100

The evolution of the carbonate saturation state is projected until 2100. The results are based on reconstructed fossil fuel and land use emissions for the 19th and 20th century and on the emissions projected by the SRES-A2 and SRES-B1 scenarios for the 21th century (see section 2.3).

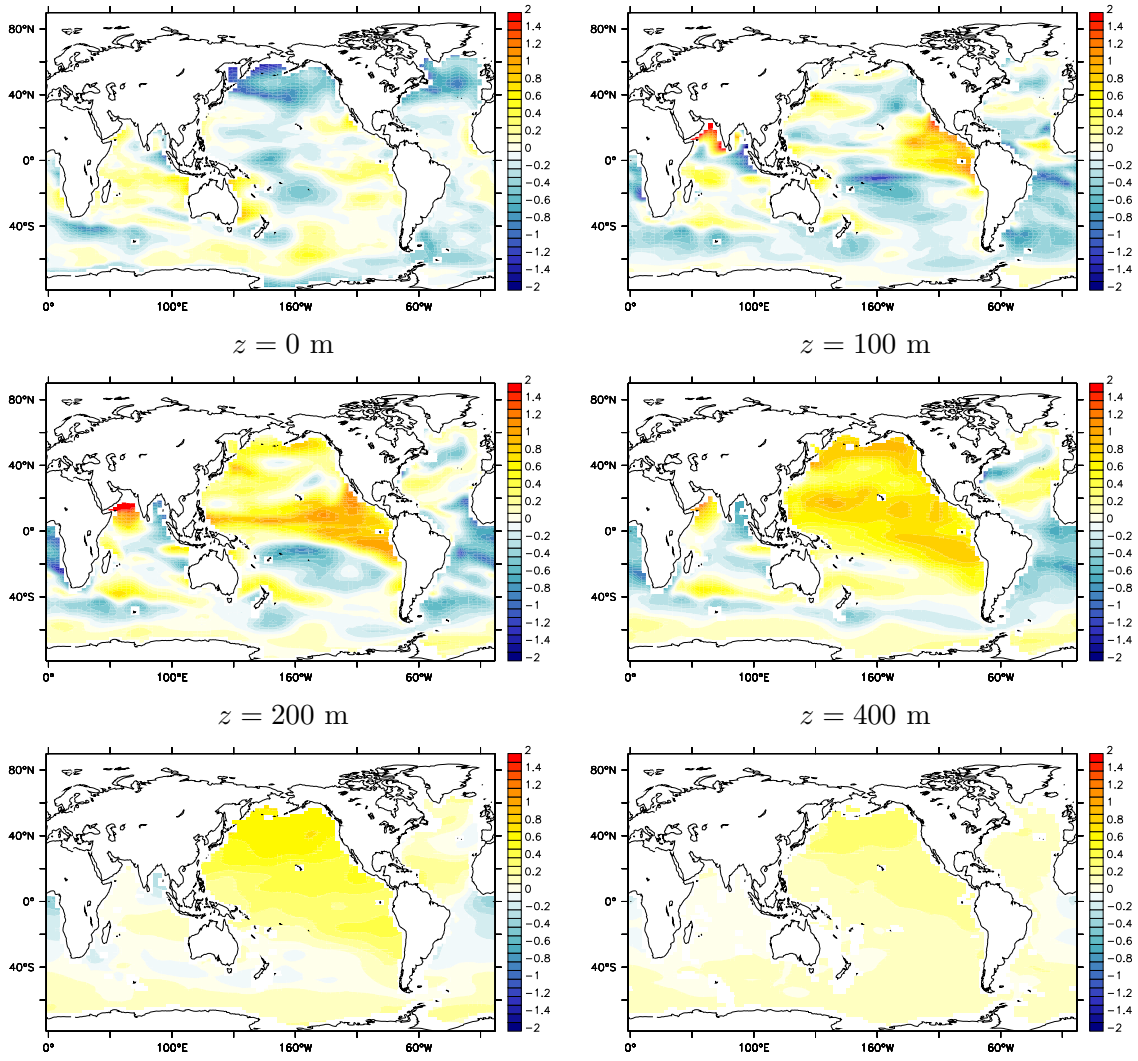

Figure 3.6: Differences between modeled and measured annual mean (1990-1999) aragonite saturation state at depths from 0 m to 2000 m.

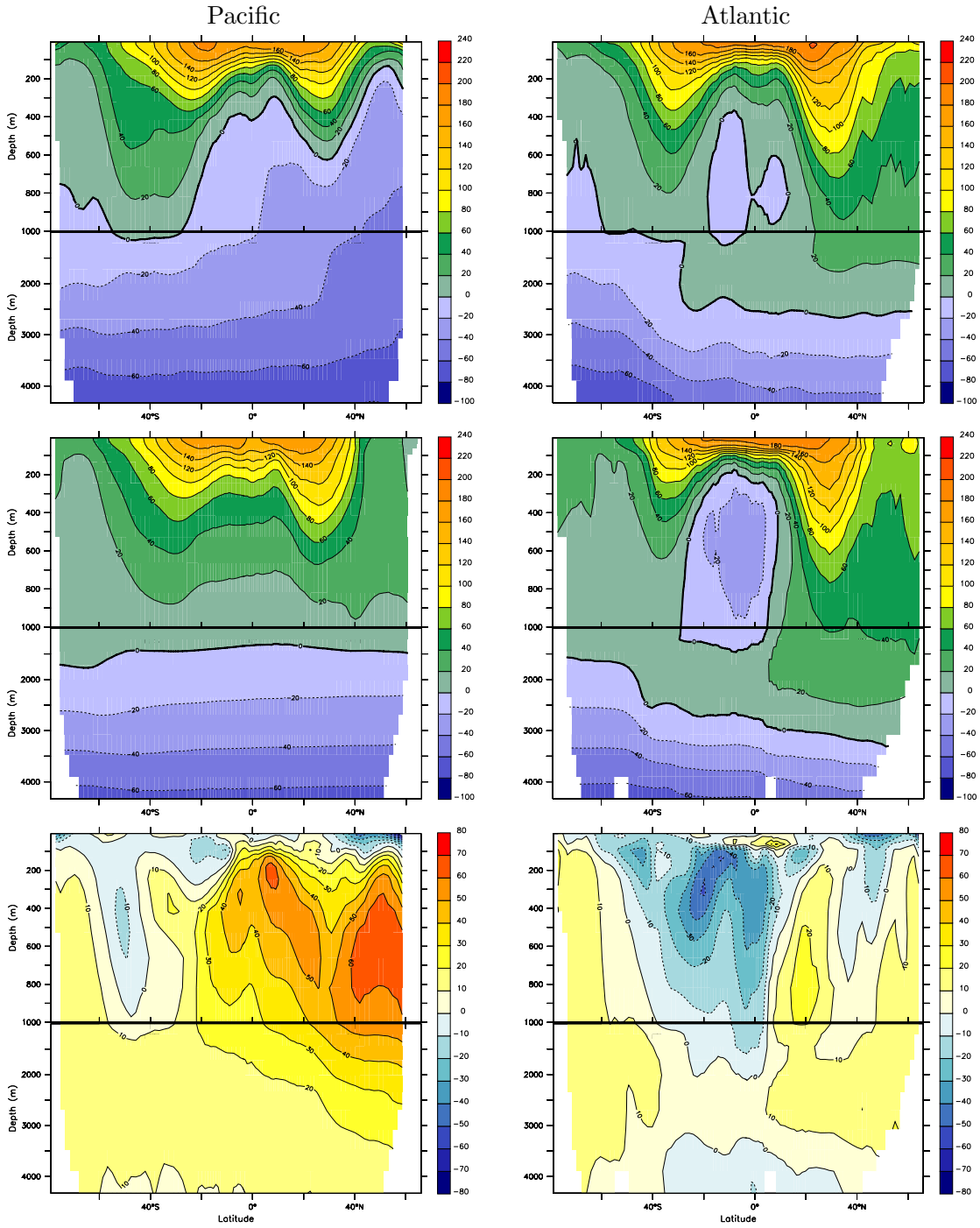

Figure 3.7: Meridional sections through the Pacific (left) and the Atlantic (right) showing zonal annual mean (1990-1999) of observed (top) and modeled (middle) $\Delta[CO_3^{2-}]$ in mmol/m^3. The saturation horizon is indicated by the thick line at $\Delta[CO_3^{2-}] = 0$. The bottom row shows the differences between model and measurements.

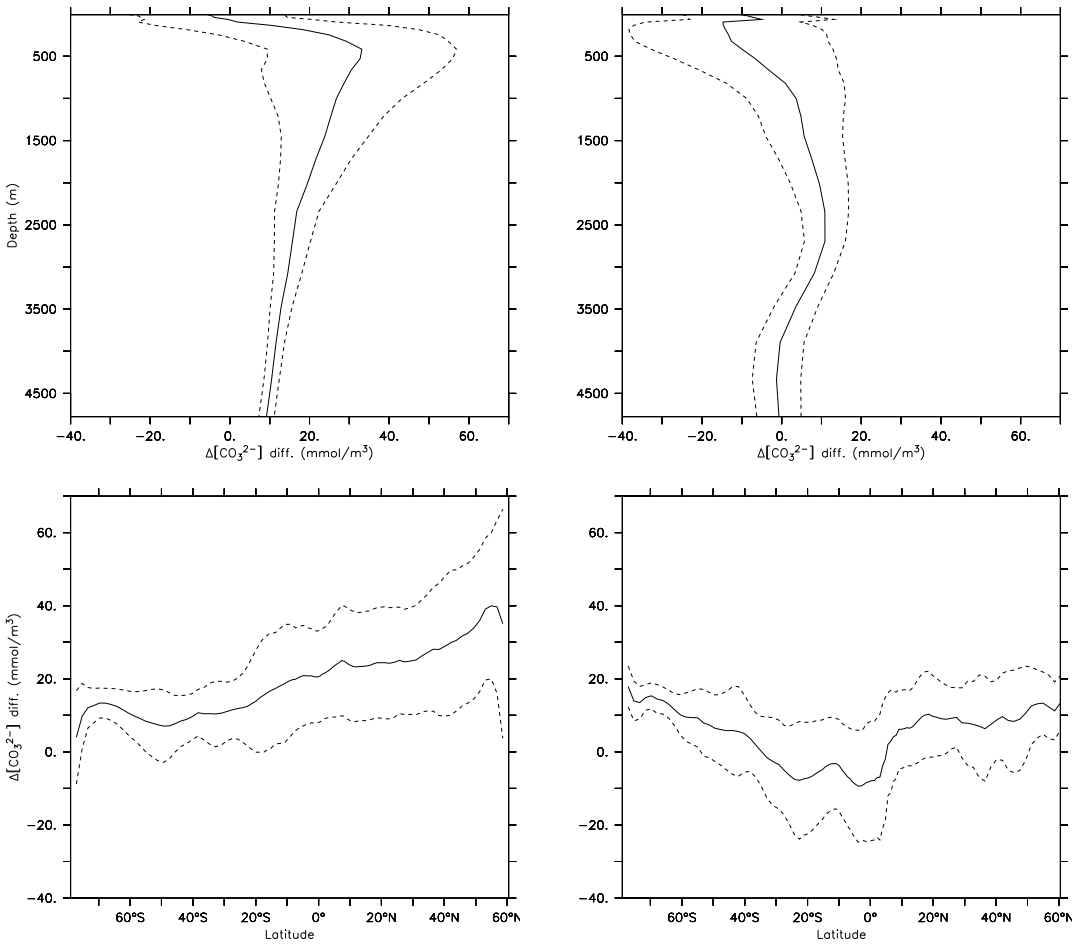

Figure 3.8: The average difference and variance between modeled and measured annual mean (1990-1999) $\Delta[CO_3^{2-}]$ (mmol/m^3) at different depths (top row) and latitudes (bottom row) for the Pacific (left) and the Atlantic (right). The area enclosed by dashed lines indicate the range of one standard deviation.

Changes in the surface aragonite saturation state

It is projected that the aragonite saturation state of surface waters will continue to decrease rapidly in all regions. Surface waters will first become undersaturated with respect to aragonite by the year 2040 at high northern and by 2065 at high southern latitudes in the A2 scenario (Figures 3.11 and 3.12). Large regions in the Southern Ocean, the Arctic Ocean, and the subarctic Pacific will be undersaturated at the surface by the end of this century. In tropical and subtropical regions, the saturation state will drop to values around 2.

For the B1 scenario, the pattern looks similar until 2050, high northern surface waters will also become undersaturated around 2040. After 2050 the stabilization of the CO_2 concentration in the atmosphere slows down the decreasing of the saturation state. By the end of the century the saturation state seems to stabilize at the surface, although at a lower level. The Southern Ocean will remain mostly saturated, the undersaturation is limited to high northern latitudes. In tropical and subtropical regions the surface saturation state will stabilize at $\Omega_A = 2.5\text{-}3.0$.

The biggest absolute changes of Ω_A can be found in the tropics and subtropics. The values

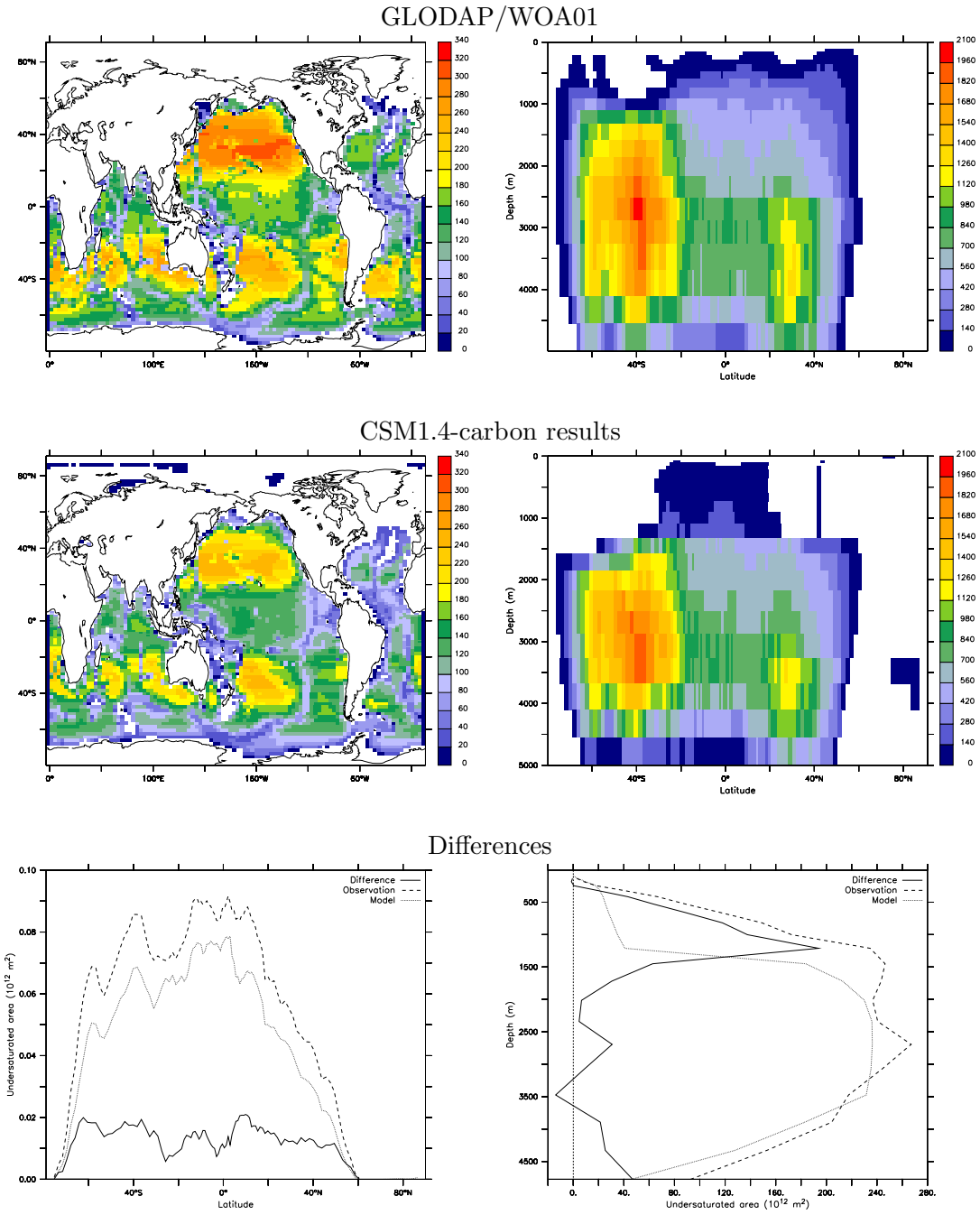

Figure 3.9: Volume of undersaturated water (10^{12} m^3) with respect to aragonite (annual mean 1990-1999) per array of gird boxes for the observation based data set (top row) and model results (middle row). The bottom panels show differences in the volume of supersaturated water at different latitudes (left) and depths (right).

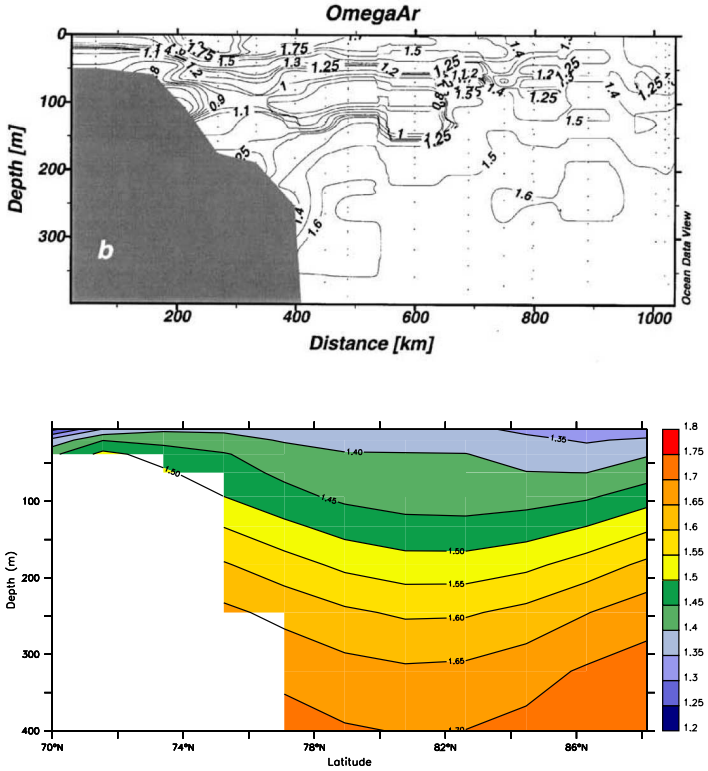

Figure 3.10: Comparison of model results with observation-based data from the Arctic Ocean Section 94 (AOS94). The top panel shows Ω for aragonite in the top 400 m over the shelf break from Jutterström and Anderson [2005], based on measurements taken on the AOS94 cruise, which started at 70°N/190°E in the Chukchi Sea (north of the Bering Strait), then led across the Mendeleyev-Alpha Ridge and the Makariv Basin to 89°N/146°E at the Lomonosov Ridge near the North Pole. As the measurements were taken in the summer, covering the months July to October, the bottom panel shows model results for this period only.

drop from 3-4 to 2 in the A2 scenario from 2000 to 2100. The spread of the absolute changes is smaller in B1 ($\Delta\Omega_A$ = -1.0 to -0.2) than in the A2 scenario ($\Delta\Omega_A$ = -1.9 to -0.5).

The changes of the aragonite saturation state at the ocean surface can be related to the mean atmospheric CO_2 concentration in the boundary layer. Surface waters north of 70° will become undersaturated at pCO_2 = 500 ppm, when the concentration reaches 600 ppm, surface waters in the south polar zone will become undersaturated, too.
This atmospheric CO_2 - surface saturation state relationship depends only little on the emission scenario. The divergence of Ω_A is 0.02±0.03 (1±2%) for the common pCO_2 range (370-540 ppm) of the A2 and B1 scenarios.
The changes in the saturation state are not linear with respect to atmospheric CO_2 concentrations, but slowing down with increasing pCO_2. The global mean surface Ω_A relative to pCO_2 can be fitted well with a second order polynomial $\Omega_A(x = pCO_2) = ax^2 + bx + c$, for the values derived from 1820-2099 under SRES A2 ($a = 4.04 \cdot 10^{-6}, b = -0.0072, c = 4.922$).
Maximum variations of the saturation state changes can be found in the subtropics, where Ω_A first drops by about 0.5 per 100 ppm at pCO_2 = 300 ppm. With increasing pCO_2 concentrations this rate decreases to about 0.35/100 ppm at pCO_2 = 500 ppm and 0.2/100 ppm at pCO_2 = 700 ppm.

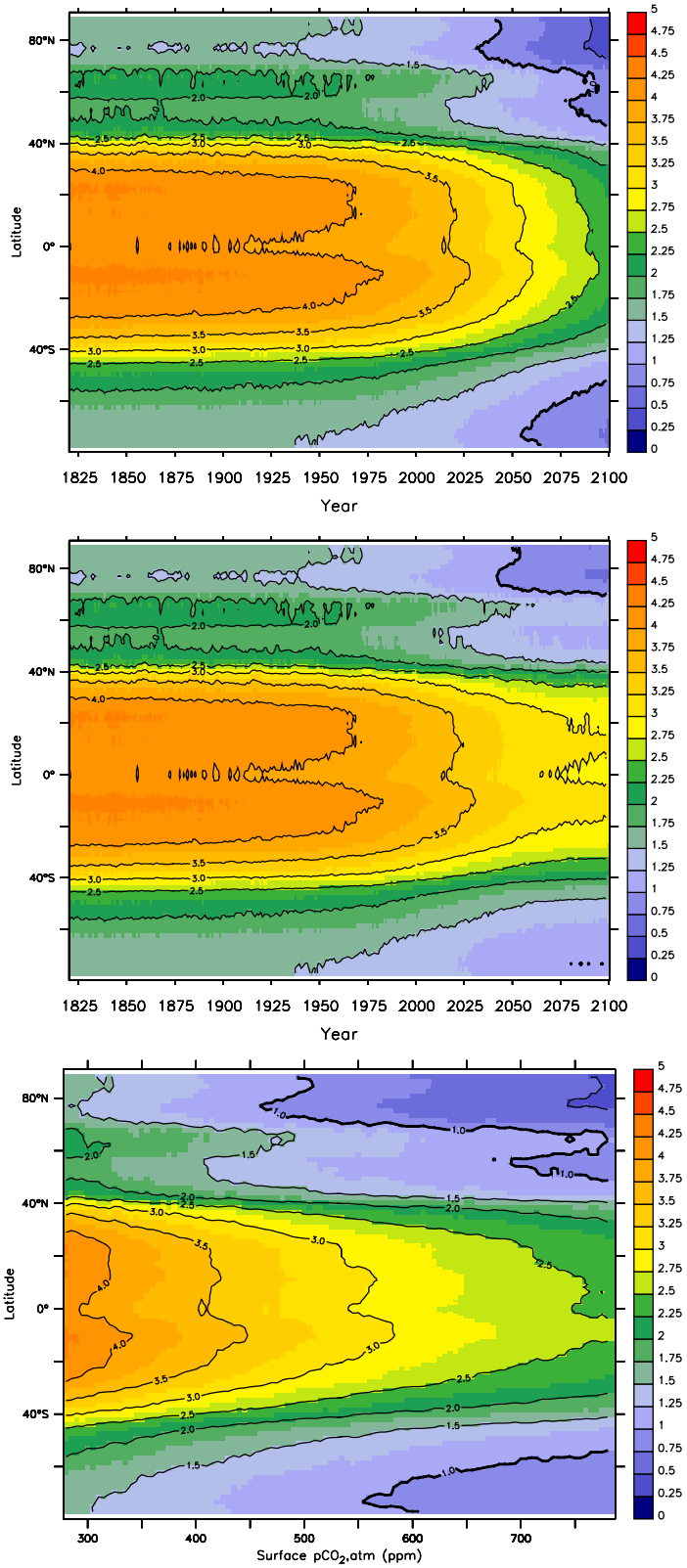

Figure 3.11: Hovmueller diagrams showing the global zonal mean evolution of the annual mean surface aragonite saturation state at different latitudes in the SRES A2 (top) and B1 (middle) scenarios. The third diagram relates the saturation state to increasing atmospheric pCO_2 at the surface. In the A2 scenario, the saturation horizon (thick line) reaches the surface by the year 2040 (and 475 ppm respectively) at high northern latitudes. After the year 2070 (625 ppm), high latitude regions will become largely undersaturated.

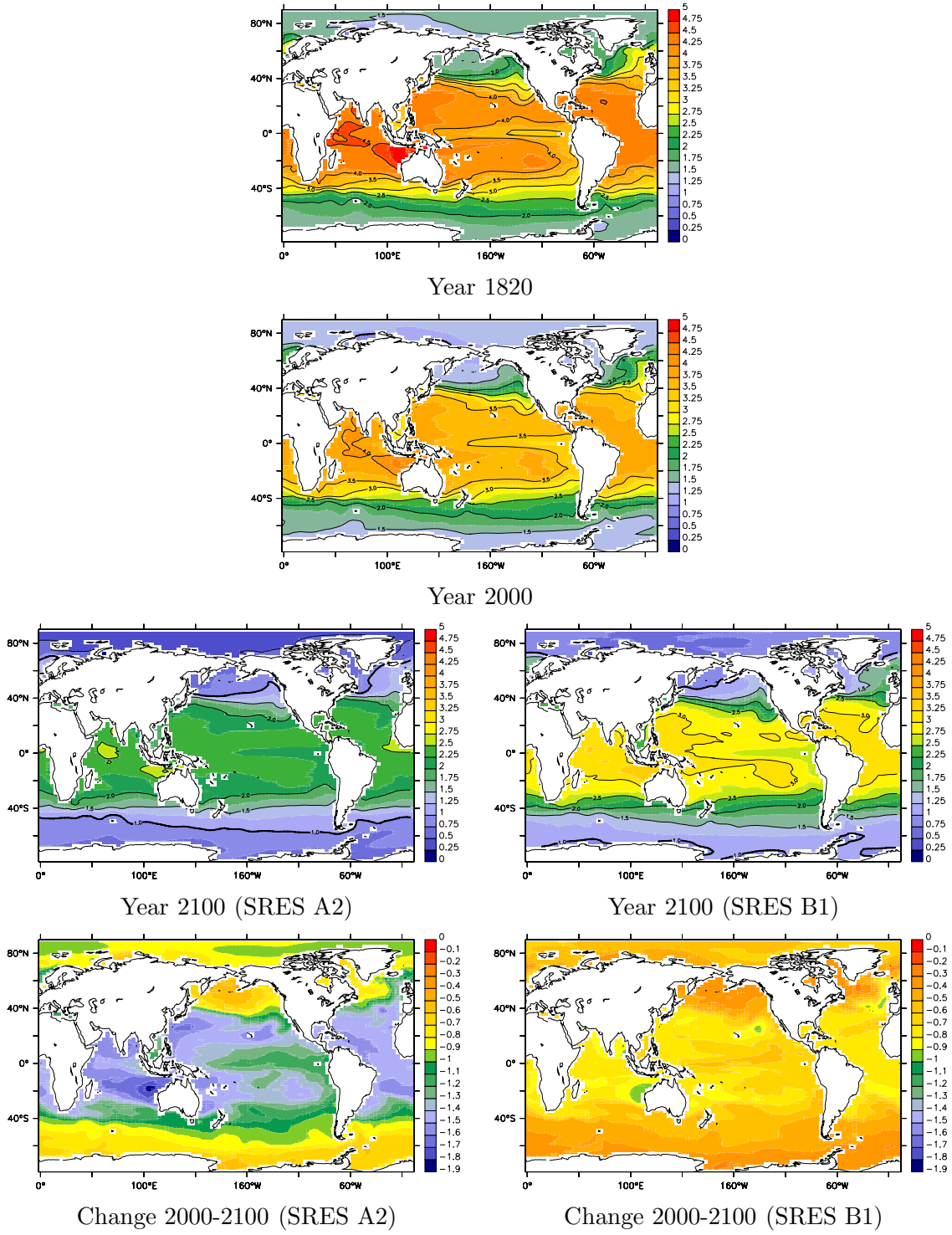

Figure 3.12: Annual mean aragonite saturation state at the surface by the years 1820, 2000 and 2100. The biggest absolute changes of Ω_A can be found in the subtropics (bottom).

Changes in the depth of the saturation horizon and in the volume of supersaturated waters

The decrease of the saturation state leads to a rise of the saturation horizon (Figures 3.13 and 3.14). At high latitudes this rise is very steep as the saturation state changes quickly in the whole water column from the surface to the saturation horizon. Whereas the rise in the lower latitudes is smoother and surface waters are more affected than deep waters. In the tropical Pacific the saturation horizon remains at the same depth of 1500 meters until 2100, although the saturation state at the surface decreases rapidly.

The shift of the saturation horizon causes a significant decrease in the volume of supersaturated seawater (Figure 3.15). In the SRES-A2 scenario it is expected that no water masses with $\Omega_A > 3$ will exist after 2070. In 1820 these water masses represented 3.2% of the global ocean volume. Further the volumes of waters with $2 < \Omega_A < 3$ and $1 < \Omega_A < 2$ decrease by about 75% and 30% of their preindustrial values, while undersaturated waters ($\Omega_A < 1$) extend from 58% to 75% of the total ocean volume. The changes in the SRES-B1 scenario are about 50% smaller than those in the A2 scenario, except for waters with $\Omega_A > 4$ and $3 < \Omega_A < 4$, that show no and only a small difference respectively.
For the top 210 m, which represents the potential habitat for many calcifying organisms, the changes are correspondingly bigger. Waters with $\Omega_A > 4$ and $3 < \Omega_A < 4$, which made up 13% and 34% of the total volume above 210 m in 1820, will vanish under SRES A2. The volume of waters with $2 < \Omega_A < 3$ is expected to decrease by about 40% from 29% to 18%, while the volume of waters with $1 < \Omega_A < 2$ and undersaturated waters increase from 24% to 45% and from 1% to 37%, respectively.

3.3.4 Projected changes in ocean surface pH until 2100

With increasing atmospheric CO_2 and the subsequent uptake by the ocean, the pH of seawater changes along with the changes in carbonate saturation described above. In the SRES A2 scenario simulation, the global annual mean ocean surface pH drops from 8.17 in the year 1820 to 7.77 in the year 2099. Under the SRES B1 scenario, the reduction is less accentuated and the projected global average pH in 2099 is 7.94 (figure 3.16).
Under the SRES A2 scenario, the largest changes from 2000 to 2100 (ΔpH around -0.45) can be found in the Arctic Ocean, where the annual mean pH drops from values around 8.15 to values around 7.70 (figure 3.17). This turns the Arctic from a region with relatively high pH in the global context to a region with relatively low pH in 2100. In the Tropics and in the Ross Sea the smallest pH reductions of about -0.25 are found. In the Southern Ocean, in the North Pacific, and in the North Atlantic, the pH is reduced more or less uniformly by about -0.30 to -0.35.

3.3.5 Seasonal variability

Seasonal variability and their changes over time has been addressed by calculating anomalies $\Delta\Omega_A = \overline{\Omega_A} - \Omega_A$ for the decades 1820-1829, 1990-1999, and 2090-2099 (under SRES A2), where $\overline{\Omega_A}$ is the mean value of the corresponding decade. At the ocean surface, Ω_A undergoes seasonal variations with maximum values in the Northern Hemisphere from August to October and minimum values from February to April (figure 3.18, left column). In the Southern Hemisphere the pattern looks the other way round, like it does for the temperature.

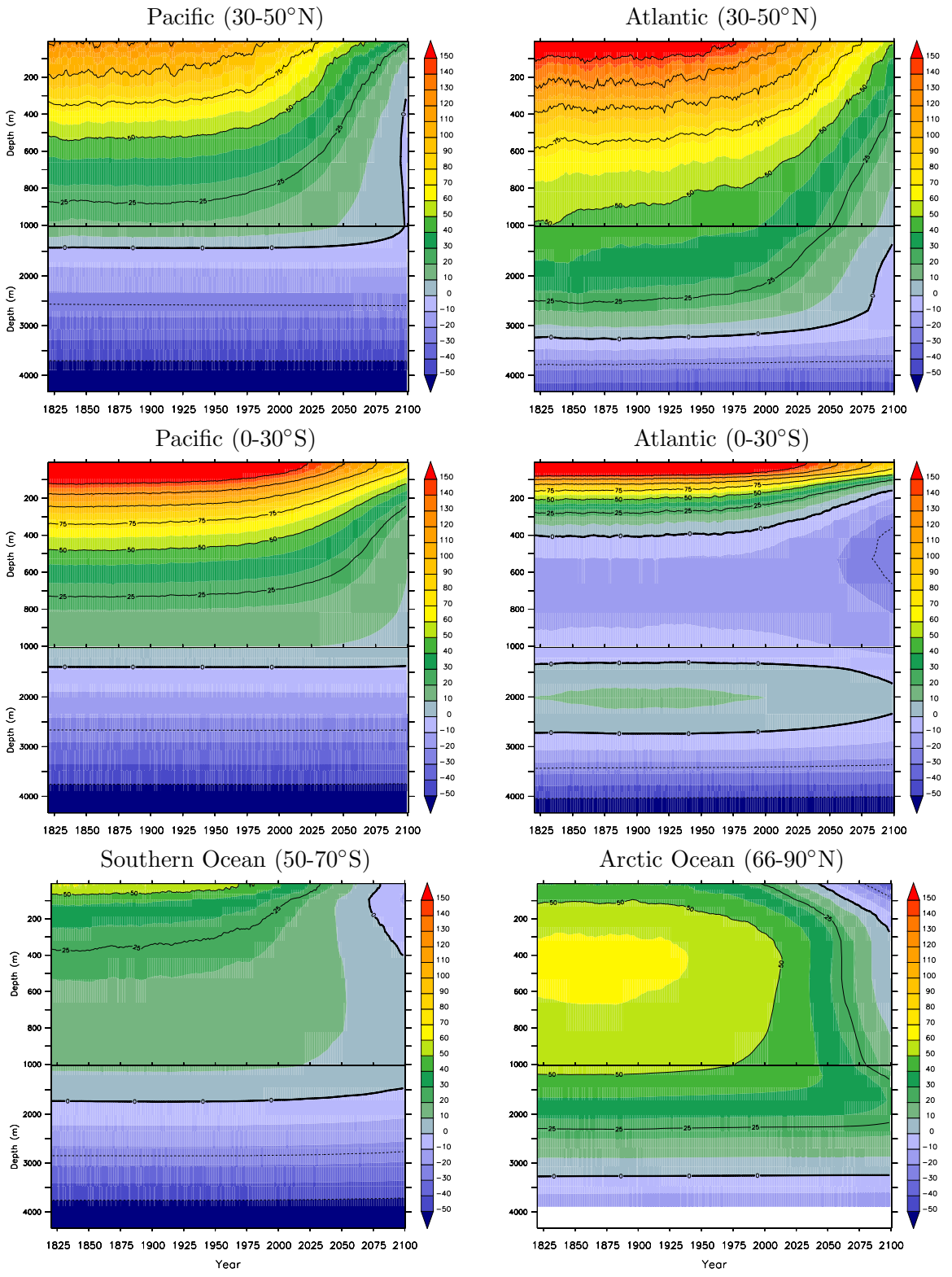

Figure 3.13: Time-depth diagrams of mean $\Delta[CO_3^{2-}]$ (mmol/m^3) at 30-50°N (top) and 0-30°S (middle) in the Pacific (left) and Atlantic (right); in the Southern Ocean (bottom left, global mean 50-70°S), and in the Arctic Ocean (bottom right, global mean 66-90°N). These projections under the A2 scenario clearly show the upward shift of the saturation horizon (thick line). In the Pacific and at low latitudes in the Atlantic, the corresponding regions in the other hemisphere show similar patterns.

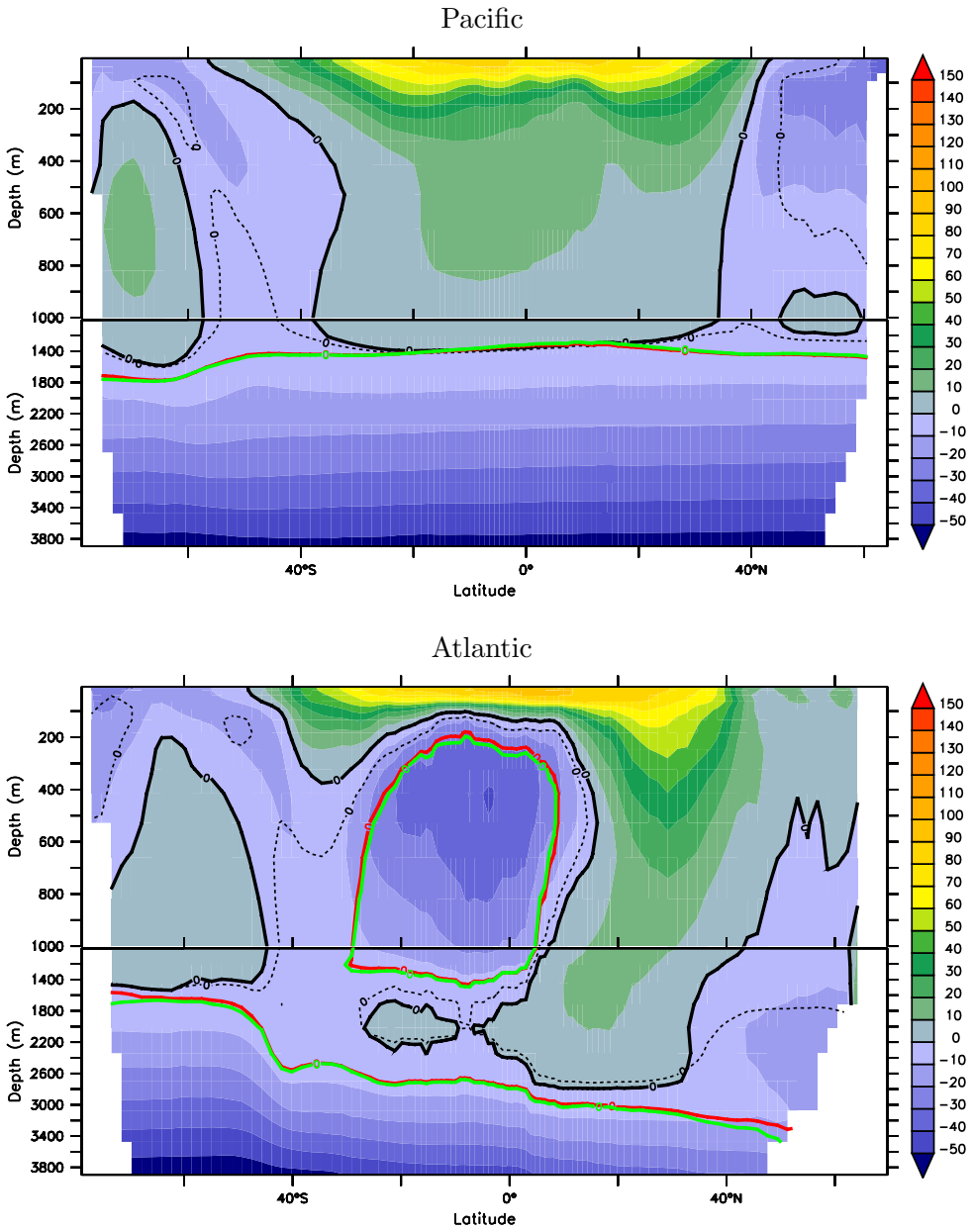

Figure 3.14: The annual mean aragonite saturation state indicated by $\Delta[CO_3^{2-}]$ (mmol/m^3) in the year 2100 under scenario A2: Zonal averages for Pacific (top) and Atlantic (bottom). Thick lines indicate the aragonite saturation horizon in 1820 (green), 1994 (red) and 2100 (black solid line for A2; black dashed line for B1).

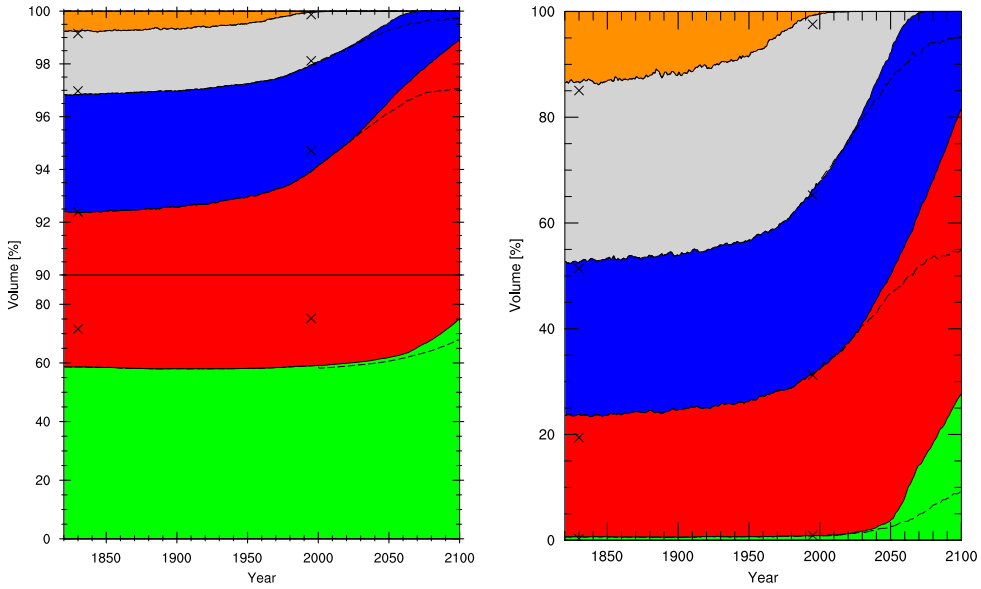

Figure 3.15: Global changes in the volume of supersaturated waters with respect to aragonite under the SRES A2. The left figure shows changes in the entire ocean volume, whereas the right figure shows only the top 210 m. Waters that are more than four times supersaturated (orange) are expected to vanish by the year 2010, and those that are 3 to 4 times supersaturated (gray) by the year 2075. The volumes of 2-3 and 1-2 times supersaturated waters (blue and red) decrease to 25% and 70% of the preindustrial values until 2100, which are changes by about 3% and 11% of the total ocean volume. Thus the volume of undersaturated waters (green) increases by about 30% (or 17% of the total ocean volume) until 2100. The dashed lines indicate the volume changes under the SRES B1 scenario. The crosses denote the respective values derived from the GLODAP/WOA01 data set for 1995 and the estimated preindustrial values (1830) obtained by subtracting anthropogenic CO_2 from DIC concentratons (see section 3.3.2 for a discussion of differences and section 3.2.2 for details on the measurements).

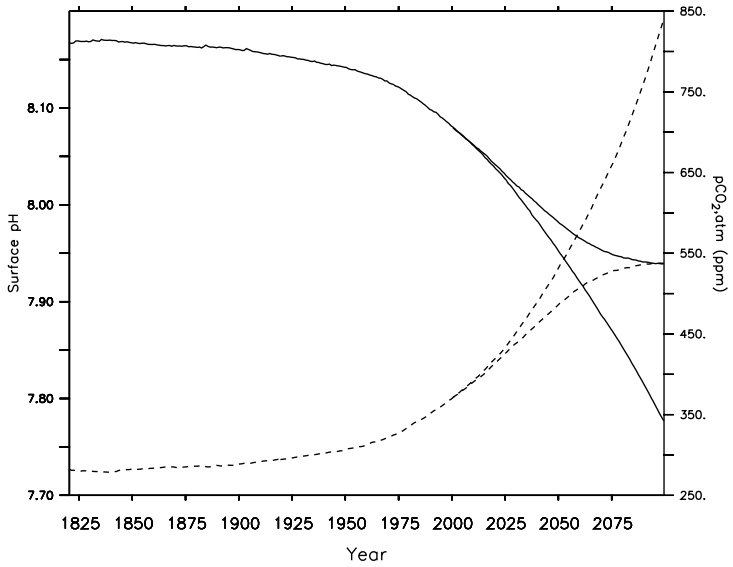

Figure 3.16: Projected global annual mean ocean surface pH (solid lines, left axis) and global annual mean atmospheric CO_2 concentrations (dashed lines, right axis) at the ocean surface in the SRES A2 (larger changes) and SRES B1 (smaller changes) scenario simulations.

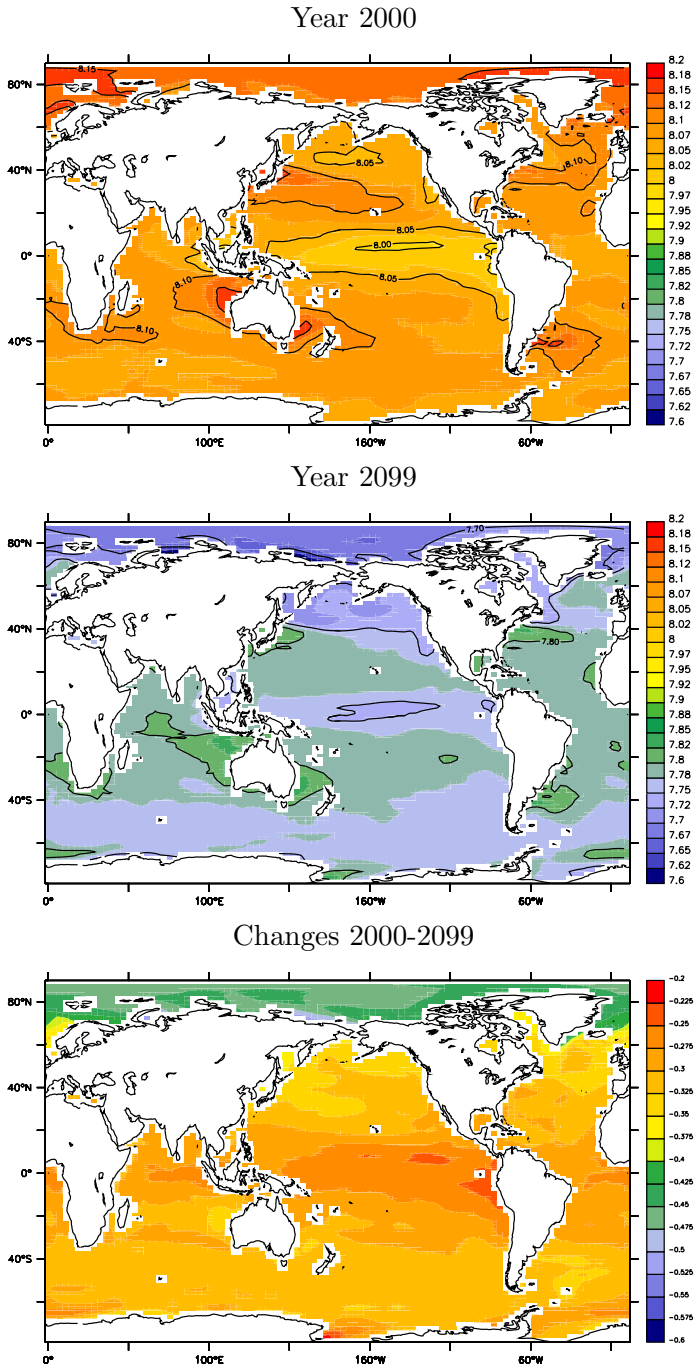

Figure 3.17: Annual mean ocean surface pH in the years 2000 (top) and 2100 (middle) as projected by the SRES A2 scenario simulation. The bottom panel shows the corresponding changes from 2000 to 2100.

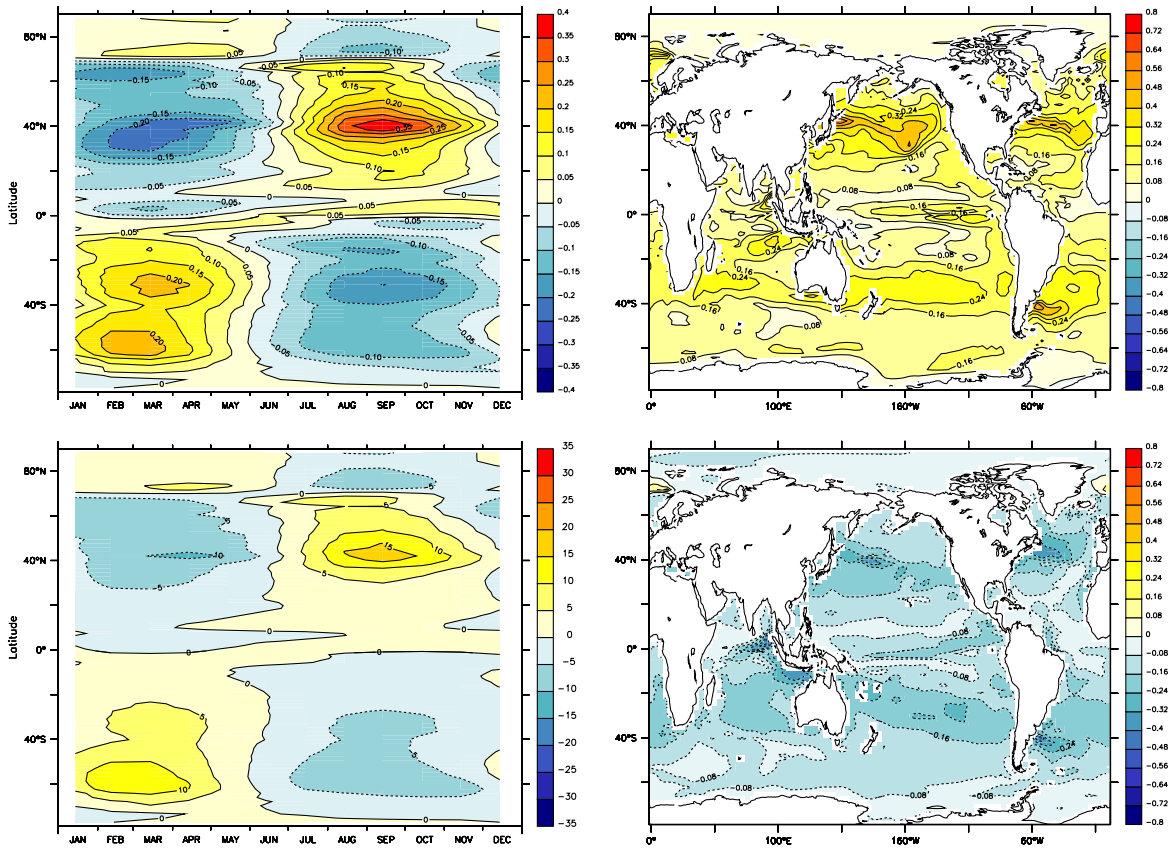

Figure 3.18: Seasonal variability of surface Ω_A for the decade 1990-1999.
Left column: Absolute (top) and relative (bottom, in percent) differences between the annual mean and the mean for each month, at different latitudes (zonal average).
Right column: Maps showing the maximum positive (top) and negative (bottom) anomalies in the surface aragonite saturation state.

Interestingly the Arctic Ocean shows the same seasonal pattern as the Southern Hemisphere. In the Arctic Ocean, the temperature is relatively constant throughout the year and alkalinity reveals a strong seasonal variability (up to +3% in April/May and -4% in August/September) compared to any other region. The varibility of DIC in the Arctic Ocean is also relatively large, but less pronounced. Therefore, the difference $[CO_3^{2-}] \approx Alk - DIC$ is small and its anomaly is positive (high alkalinity) in the first half of the year and negative in the second half (low alkalinity).

Maximum seasonal amplitudes $\Delta\Omega_A = -0.7$ to $+0.5$ can be found around 40°N in the West of the Pacific and the Atlantic, in the Indian Ocean near the coast of Indonesia, and in the South Atlantic near the coast of Argentina (figure 3.18, right column). These regions correspond with regions of high primary production and with large seasonality in production.

The average anomalies, including the standard deviation with respect to different longitudes and years of the decade 1990-1999, are shown in figure 3.19. The aragonite saturation state at the surface is increased by the end and after the high production phase (spring in the Southern Hemisphere/autumn in the Northern Hemisphere). It is approximately equal to

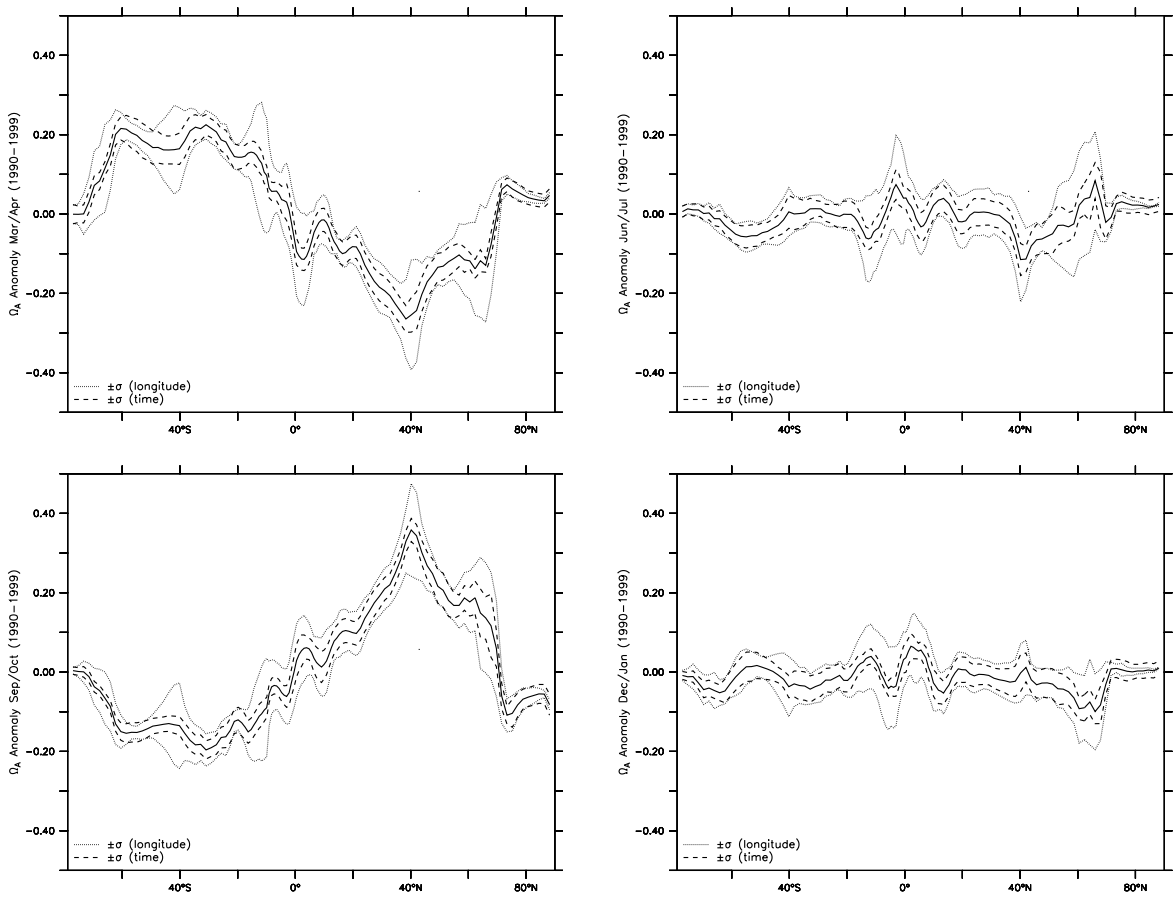

Figure 3.19: Average seasonal and interannual variability of surface Ω_A in March/April (top left), June/July (top right), September/October (bottom left), and December/January (bottom right) for the decade 1990-1999. Dashed lines indicate the interannual variability (one standard deviation); dotted lines indicate variability with longitude (one standard deviation).

the long-term average during summer and winter at all latitudes, and reduced after the low production phase. There are relatively large zonal fluctuations (σ =0.10-0.15) in high-production regions (around 40°S, at 40-70°N and around the equator), as the productivity differs among different longitudes. The standard deviation with respect to different years of the decade is usually smaller (σ =0.01-0.08).

The absolute amplitudes and patterns of the seasonal variability don't show any significant changes between 1820 and 2100 under SRES A2. However, as Ω_A decreases, the relative seasonal variability becomes larger. It increases from about +10%/-5% relative seasonal variability at 40°N in 1820 to about +25%/-15% in 2100.

Seasonal variability can be seen until 200 - 400 m depth and the amplitude seems to decrease slightly by the end of this century for waters below 50 m. The effect on the saturation horizon is low, except where it crosses surface waters with significant seasonal variability. There, the saturation horizon may vary by about 50 m in depth or 10° in latitude, due to seasonal variability (figure 3.20).

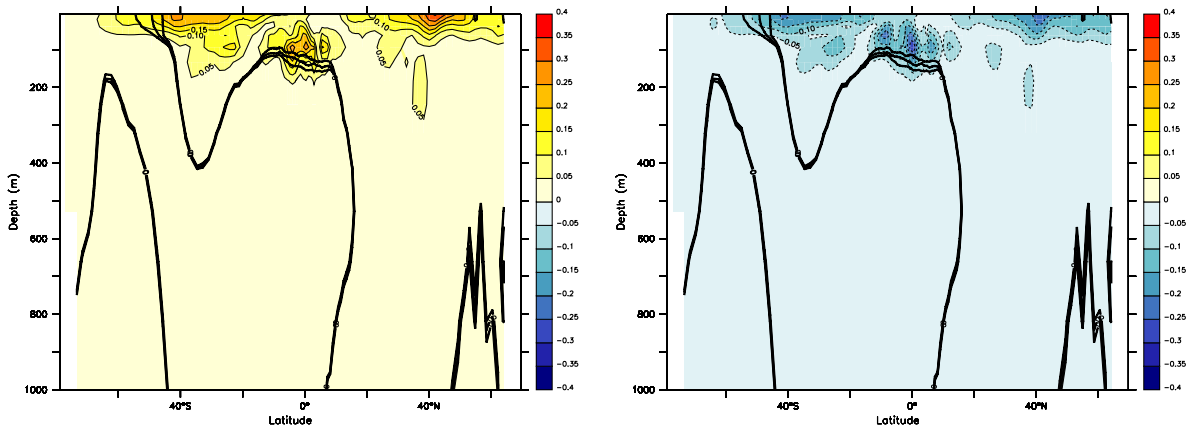

Figure 3.20: Maximum positive (left) and negative (right) seasonal anomalies of Ω_A in the Atlantic at depths of 0-1000 m, projected for the year 2100 under SRES A2. In both panels, the three thick lines indicate the annual average, the maximum and the minimum depth of the saturation horizon over the seasonal cycle.

3.3.6 The impact of climate change on projected changes in carbonate saturation state until 2100

In addition to the simulations discussed so far in this chapter, a 'no warming' simulation has been performed that includes CO_2 emissions according to the SRES A2 scenario, but does not account for the radiative forcing (see section 2.3). By comparing the ocean acidification results from this simulation with the results from the standard SRES A2 simulation discussed above, the impact of climate change on changes in the carbonate saturation state can be estimated.

The global annual mean ocean surface temperature, salinity, and alkalinity in the standard simulation exhibit relative large changes compared to the simulation without warming, where T, S and Alk remain more or less constant (figure 3.21). For annual mean surface DIC, Ω_A and pH this is completely different and both simulations project very similar changes. The surface DIC increase by 2100 is about 8% larger in the simulation without warming, because the capacity of the ocean to store CO_2 is higher at lower temperatures. Consequently, the projected decrease of surface Ω_A is also slightly larger (about 4% by 2100) in the simulation without warming, as Ω_A depends mainly on the DIC concentration when alkalinity is constant. In contrast, the pH decrease is slightly smaller (about 4% by 2100) without warming.

By reason of this global perspective, it is evident that changes in surface DIC, Ω_A, and pH are mainly dominated by the increase of atmospheric CO_2 per se, but not by the climate change (warming) due to this CO_2 increase. As for surface temperature, salinity and alkalinity, the opposite is the case.

Although little, climate change do have an effect on carbonate saturation state changes. In particular, there are regions where the differences between the simulations with and without warming are more significant than in the global average. Figure 3.22 shows the aragonite saturation state found in the two simulations by the end of this century. There are relatively large differences in the Arctic Ocean, where surface Ω_A remains 0.25-0.4 higher in the simulation without warming (figure 3.23). This is because the decrease in Alk (while DIC remains constant) in the standard simulation is larger than the increase of DIC (while Alk remains

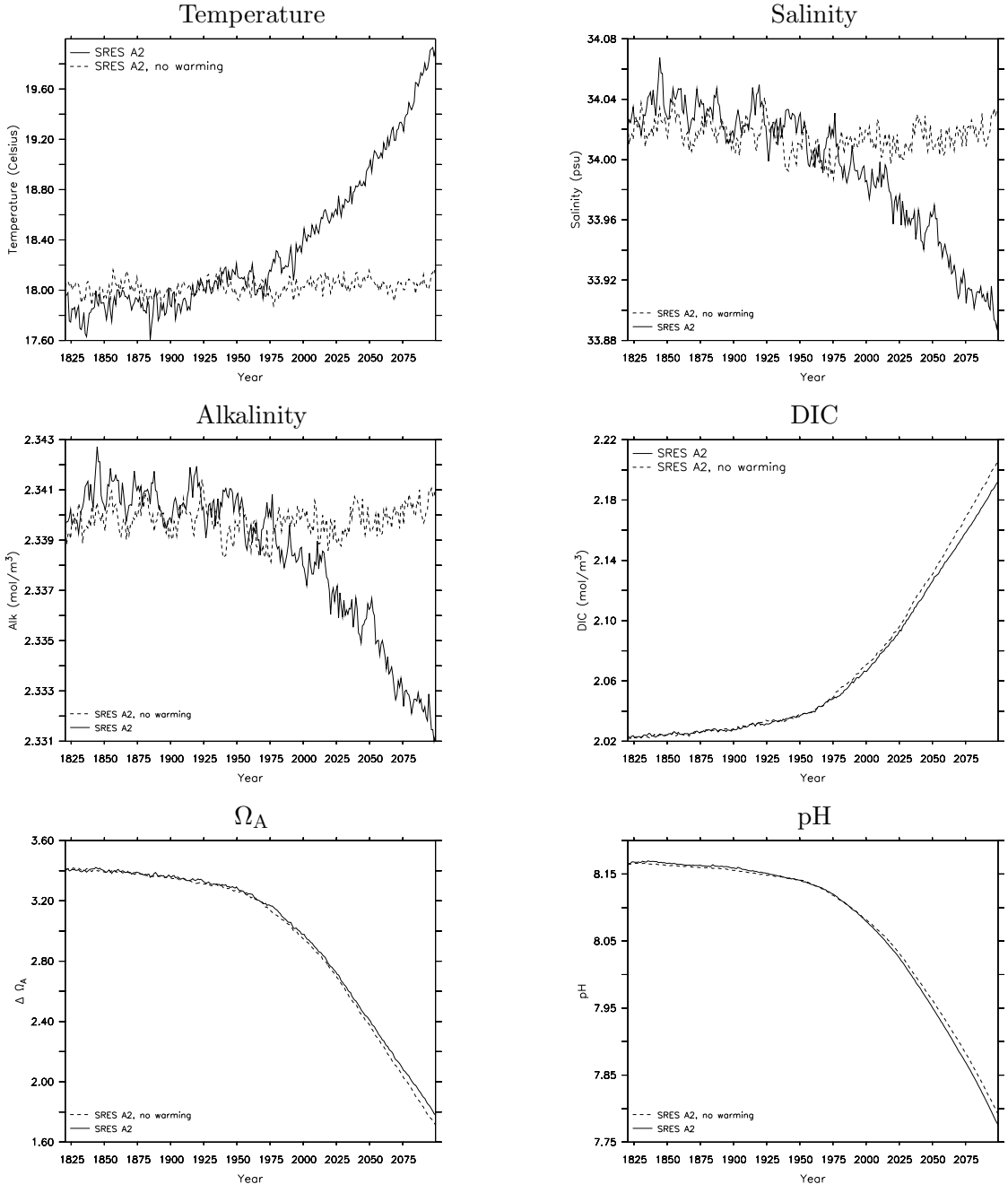

Figure 3.21: Global annual mean surface temperature, salinity, alkalinity, DIC, Ω_A, and pH as projected by the SRES A2 simulations with (solid line) and without warming (dashed line) for the years 1820 to 2099.

constant) in the no-warming simulation. At values around 0.7, this is a significant difference. In most other regions surface Ω_A is slightly lower in the simulation without warming. In the North Pacific between 60°N and 80°N, there is a relatively large difference in Ω_A up to 0.6 at depths between 1000 m and 3000 m.

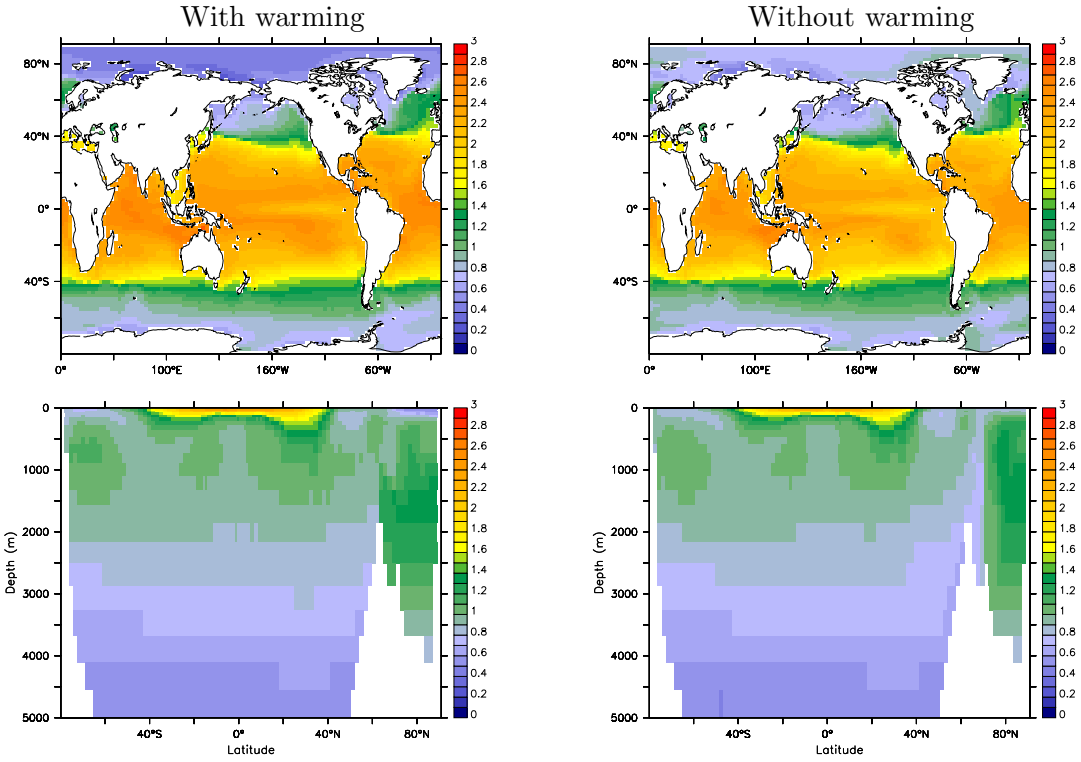

Figure 3.22: Surface (top row) and zonal average (bottom row) Ω_A in the simulations with (left) and without warming (right) by the end of the century. All panels show averages over the decade 2090-2099.

3.3.7 Sensitivity analysis

In order to estimate the uncertainties introduced by the simple pressure calculation and the constant present-day value for silicate (see also section 3.2), some sensitivity analysis have been performed.

Silicate concentrations have been either set to zero, increased uniformly by 20 $\frac{\mu\text{mol}}{\text{l}}$ (which corresponds to 10-90% of the original concentration), or doubled. These changes lead to local differences in $[CO_3^{2-}]$ and Ω_A of 0.4±0.2%, 0.5±0.1% and 0.6±0.3% respectively; maximum values are around 1%. Hence the silicate concentrations have little effect on carbonate concentration and saturation state.

To estimate the robustness of the results with respect to in-situ pressure calculations, the mean density of seawater used to calculate the pressure (eq. 3.1), has been varied from 1020 $\frac{\text{kg}}{\text{m}^3}$ to 1060 $\frac{\text{kg}}{\text{m}^3}$. The results differ by 0.3±0.1% to 0.5±0.1% for $[CO_3^{2-}]$ and by 0.3±0.2% to 1.8±0.8% for Ω_A; maximum values are around 3%.

The calcite saturation increases from about 0.1±0.1% at the surface to 0.75±0.3% at a depth

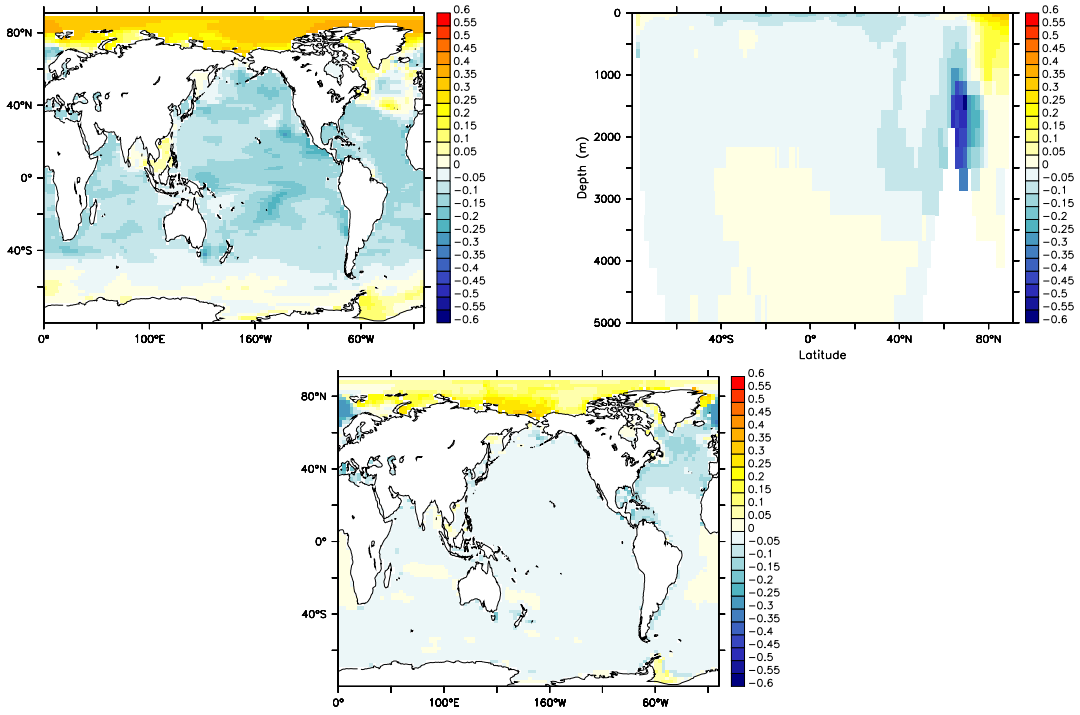

Figure 3.23: Differences in projected Ω_A between the simulations with and without warming. The top left panel shows the difference at the surface, the top right panel the global zonal mean difference and the bottom panel the average difference in the entire water column. All panels show the difference no-warming simulation minus standard simulation, averaged over the decade 2090-2099.

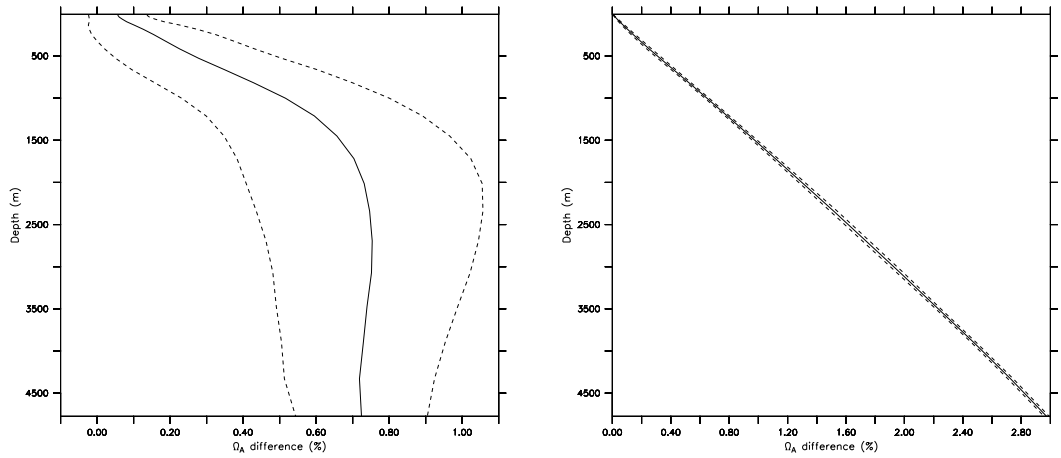

Figure 3.24: The effect on the aragonite saturation state, when doubling the silicate concentrations (left) and changing the mean seawater density from 1028 $\frac{\text{kg}}{\text{m}^3}$ to 1060 $\frac{\text{kg}}{\text{m}^3}$ (right). The solid line shows the average difference in percent and the dashed lines indicate one standard deviation of the differences.

of 2000 m and below, due to a doubling of the silicate concentrations (figure 3.24), following roughly the average silicate concentration gradient in the water column. With a mean seawater density of 1060 $\frac{kg}{m^3}$, the difference in Ω_A shows a linear response from 0% to about 3% at 4750 m. As a result, the error of $[CO_3^{2-}]$ and Ω_A can be expected less than 4% in regard to uncertainties of pressure and silicate. For surface waters the error can even be considered less than 1%.

3.3.8 Uncertainties

How certain are these results? Of course the emission scenario has a large impact on the results, because atmospheric CO_2 is the main driver of the projected changes. But for a given scenario, i.e. atmospheric CO_2 levels, the following four points have to be considered in order to estimate the uncertainties of the results:

1. The uncertainty of the model output (variables T, S, Alk, DIC, PO_4).

   It is difficult to quantify this uncertainty but one can compare the model results with observation based data or with other models to get an estimate. The model-observation comparison has shown that the model performs well in most regions. The average difference in the Atlantic is less than 15 % for Ω_A, except for latitudes south of 60°S and depths around 500 m, where the difference increases up to 20%. In the Pacific, average differences are less than 20% south of 20°S, less than 40% south of 30°N and then rise up to 90% in the North Pacific. The biggest differences in the Pacific can be found at depths of 500 to 1000 m.

2. The error by taking constant values for SiO_3 from WOA01.

   Sensitivity analysis have shown, that this error is very small ($< 1\%$ for Ω_A; see section 3.3.7).

3. The error of the simple pressure calculation.

   This error is also small, especially in the upper layers of the ocean ($< 1\%$ for Ω_A in the first 1500 m, $< 3\%$ below; see section 3.3.7).

4. The error in the calculation of the carbonate saturation variables.

   This includes effects that are not considered in the calculation and errors in the constants that were used. The probable error in Ω_A due to uncertainties in the equilibrium constants and measurements, has been estimated by Chung et al. [2004] to ± 0.054. This is $\leq 5\%$ for supersaturated waters and that is far less than the uncertainty of the model output.

Based on this, it is assumed, that the results can be considered to be quite reliable. The biggest uncertainties come from the simulated quantities and are expected to be strongly dependent on any specific region concerned.

3.4 Discussion

3.4.1 Main results

The projected changes in the carbonate chemistry of the ocean due to increasing atmospheric CO_2 show significant reductions of the carbonate saturation levels and a decrease of the pH of seawater. These projections are based on two SRES scenarios, a high CO_2 emission (A2) and a low CO_2 emission (B1) scenario.

Global annual mean surface pH decreases from 8.17 to 7.70 (A2) and 7.94 (B1), respectively, during the simulations from 1820 to 2100. The Arctic is exposed to the largest decrease and changes from a high-pH to a low-pH region. At high latitudes, the aragonite saturation state of surface waters will decrease by 0.5 to 1.0 in the A2 scenario (0.2 to 0.5 in B1 scenario) during this century. High latitude surface waters will start to become undersaturated by 2040 (475 ppm) in the north, and by 2060 (575 ppm) in the south. By 2100 the Southern Ocean and high northern latitude waters are expected to be largely undersaturated. The Southern Ocean is particularly affected because of low temperatures at the surface and large amounts of upwelling waters with high CO_2 concentration from organic matter remineralization. In the tropics and subtropics Ω_A is expected to decrease by 1.0 to 1.9 (about 30-60%) in the A2, and by 0.5 to 1.0 (about 15-30%) in the B1 scenario.

The aragonite saturation horizon shoals from about 1700 m to the surface in the Southern Ocean and in the subarctic Pacific. In the North Atlantic, it shoals from 3200-3400 m to 500-1400 m. As a result, the volume of supersaturated waters, which represent potential habitats of calcifying organisms with aragonite shells or skeletons, is reduced by about 12% (B1 scenario) to 20% (A2 scenario). Waters with saturation states, that are believed to provide optimal conditions for aragonite calcifiers ($\Omega_A > 4$), will even vanish for both B1 and A2.

The B1 scenario shows similar results as the A2 scenario until 2050. After that, the saturation state stabilizes at the surface due to the stabilization of the atmospheric CO_2 concentrations, which is a result of the reduction of the emissions in the B1 storyline after 2040.

The simulated seasonal variability is small in the high latitude and tropical ocean. In the mid-latitudes there are deviations up to 15-20% from the annual mean. The interannual variability is small.

The impact of climate change on changes in the carbonate saturation state is relatively small in the global mean. In most regions the decrease in Ω_A is slightly larger (0.05 to 0.25 at the surface) in the simulation without warming. In the Arctic Ocean the decrease is smaller in the no-warming simulation and in the North Atlantic at 1000 - 3000 m depth, the reduction is larger than anywhere else.

A comparison with observational data shows that the model is able to reproduce the present-day $CaCO_3$ saturation states reasonably well. There are, however, differences that have to be considered, particularly in the North Pacific. A too low export production in the North Pacific and Antarctic Intermediate Water that is not penetrating far enough northwards, do affect the model projections.

3.4.2 Related work and comparison to other studies

The presented results are in very good agreement with results from Orr et al. [2005], that are based on 13 models that participated in the second phase of the Ocean Carbon-Cycle Model Intercomparison Project (OCMIP-2), forced by the IPCC IS92a and S650 CO_2 scenarios. These scenarios are similar to the A2 and B1 scenarios used here. However, the IS92a yields lower atm. CO_2 by about 60 ppm less than the A2 scenario by 2100. The concentrations in S650 stabilizes at a level that is about 25 ppm higher than in the B1 scenario. In contrast to the results presented here, simulated perturbations were added to the modern DIC data provided by GLODAP and alkalinity was assumed to be constant in the Orr et al. [2005] study. Further the models were accounting for the direct geochemical effect only, but a comparison with three coupled climate models showed that the effect of climate change and seasonal variability is relatively low (increase of $[CO_3^{2-}] < 10\%$).

Common findings are the onset of undersaturation of Southern Ocean surface waters with respect to aragonite at 550 ppm atmospheric CO_2 concentration (by the year 2050/2055 in the IS92a/A2 scenarios) and the extension of the undersaturation at the surface to the entire Southern Ocean and into the subarctic Pacific Ocean by 2100. Orr et al. [2005] project a surface CO_3^{2-} concentration in the Southern Ocean (all waters south of 60°S) of 55±5μmol/kg by the year 2100, while our results yield 52±6 μmol/kg. Further the average tropical surface $[CO_3^{2-}]$ (all waters between 23.5°S and 23.5°N) declines in both studies by about 45 % to 147±9 μmol/kg (present study) and 149±14μmol/kg (Orr et al. [2005]), respectively.

In the Atlantic, the patterns of the saturation horizon in 2100 basically look similar, but differences are found in the North Atlantic. The horizon remains lower (at 2800 m in the Subtropics; at 500 m north of 50°N) in the present study than found by Orr et al. [2005], where the horizon shoals to about 1000 m in the Subtropics, and to 115 m north of 50°N. These differences are possibly due to deeper penetration of intermediate and deep waters in the North Atlantic in the present study, that leads to more supersaturated waters between 10°N and 30°N, at depths of 800-2800 m. Similar differences can also be seen in the comparison with observations, where the carbonate ion concentration in that region is about 10-20% higher than observation-based estimates (figure 3.7).

In the Pacific, the CSM1.4-carbon model results show a lower saturation horizon throughout the Pacific. Particularly in the North Pacific the saturation horizon is too deep and the model results show horizontal layers with respect to calcium carbonate concentrations, whereas observation based data indicate these layers shoal in the North Pacific (figure 3.2). The aragonite saturation horizon remains at 1400 m in the tropical and subtropical Pacific. On the other hand, it shoals quickly to the surface at latitudes higher than 40°. Orr et al. [2005] find that the saturation horizon shoals to 200-400 m in the tropical and subtropical Pacific, and consequently a less steep rise at higher latitudes.
In the Southern Ocean, water at depths of 200-1400 m south of 60°S (Pacific) and 50°S (Atlantic) remain slightly oversaturated in the present study, whereas Orr et al. [2005] project that the whole water column becomes undersaturated by 2100 under the IS92a scenario. In the South Atlantic, they find that the saturation horizon reaches the surface at about 60°S, while it rises steeper in the present study and reaches the surface at about 50°S.

The differences in the saturation horizon between Orr et al. [2005] and the present study are in regions with small $[CO_3^{2-}]$ gradients (e.g. 10-20 mmol/m^3 per 1000 m depth in the Pacific),

thus small differences in projected carbonate ion concentrations result in large fluctuations of the saturation horizon depth. These differences are about 10-20% of the in situ carbonate ion concentration and can partly be explained with increased water temperature due to global warming (+0.5°C in the tropical pacific at about 750 m from 2000 to 2100), which has not been taken into account by Orr et al. [2005]. However, the influecnce of global warming was found to be small in these regions and there are shortcomings in the CSM1.4-carbon model, as the comparison with observations has shown.

Chung et al. [2004] project, that the intermediate water (centered at about 800 m depth) of the entire tropical Atlantic will become undersaturated with respect to aragonite by about the middle of this century. This projection is based on the WOCE/JGOFS/OACES Atlantic carbon data set and the mean accumulation rate of anthropogenic CO_2 in the western tropical Atlantic over the last 45 years (0.20 μmol kg^{-1} yr^{-1}).
This finding is mostly consistent with this study, but the undersaturated area is shifted southwards by about 10°; we project undersaturated water in the entire Atlantic at depths of 800-1200 m at 30°S, shoaling to 300-700m at 5°N, but north of 10°N the Atlantic remains mostly supersaturated (figure 3.2). Again, the comparison of our results with observations suggest, that this southward shift is due to deficiencies in the model.

Caldeira and Wickett [2005] used the Lawrence Livermore National Laboratory (LLNL) ocean general circulation model to predict future changes in DIC and the effect of these changes on marine chemistry. This model uses the abiotic carbon protocols from the OCMIP-2 project and does not account for climate, circulation, biological, land-biosphere or dust feedbacks. It has been forced with different CO_2 emission and stabilization scenarios, among them the SRES A2 and B1 scenarios.
They find nearly identical values for mean surface pCO_2 (370 ppm), ΔpH (-0.09) and Ω_A (2.9) in the year 2000. The projected pCO_2 is considerably higher under both scenarios than in the present study (970 ppm in A2 and 650 ppm in B1 by 2100, which is 15% and 20% more, respectively), hence the mean surface aragonite saturation states are also lower. They project Ω_A=1.4 and ΔpH=-0.46 under A2, and Ω_A=1.9 and ΔpH=-0.30 under B1 in 2100, whereas we find Ω_A=1.8, ΔpH=-0.39, Ω_A=2.3 and ΔpH=-0.23, respectively). However, at corresponding atmospheric CO_2 concentrations we find Ω_A=1.5 at 970 ppm (extrapolated from A2 by second order polynomial fitting) and Ω_A=1.8 at 650 ppm (from A2), which match the values from Caldeira and Wickett [2005] within $\pm$0.1.
This indicates that both models show a similar response to atmospheric CO_2 concentrations with respect to calcium carbonate saturation, but behave differently regarding the distribution of anthropogenic CO_2 among different pools and/or transport in the ocean. Caldeira and Wickett [2005] admit that their model tends to get a relatively shallow North Atlantic thermohaline circulation, with much of the deep North Atlantic filling up with Antarctic Bottom Water. Their model takes up 1.86 PgC yr^{-1} for years 1980-1989 and 2.16 PgC yr^{-1} for years 1990-1999, this are 2-8% larger amounts than in the present study, where the ocean uptake is about 1.75 PgC yr^{-1} for years 1980-1989 and 2.01 PgC yr^{-1} for years 1990-1999. Both studies compare with 1.8$\pm$0.8 PgC yr^{-1} and 1.9$\pm$0.7 PgC yr^{-1} estimated by Le Quéré et al. [2003], and 1.7$\pm$0.6 PgC yr^{-1} and 2.4$\pm$0.7 PgC yr^{-1} estimated by Plattner et al. [2002].

Kleypas et al. [1999] investigated the future decrease of the aragonite saturation state in the tropics to assess geochemical consequences on coral reefs. They used two methods to project changes in surface saturation state. The first assumed constant alkalinity through

the middle of this century and that the ocean surface response to increased $pCO_{2,atm}$ is strictly thermodynamic, i.e. $pCO_{2,surf}$ is near equilibrium with $pCO_{2,atm}$. The second method employed the Hamburg Ocean Carbon Cycle (HAMOCC) global model, which simulates the response of the entire carbon system to increased $pCO_{2,atm}$.
Using the first method, they found that average surface Ω_A in the tropics was 4.6±0.2 in 1900, 4.0±0.2 in 2000, and projected values of 3.1±0.2 and 2.8±0.2 for the years 2065 and 2100 under the IPCC IS92a scenario. The HAMOCC model values are consistently lower, because of slightly different global change scenarios and differences between modeled and measured alkalinity.
These values are 8-10% higher for years 1990-2065 and 18% higher for 2100 than those found in the present study under SRES A2. The HAMOCC model values are 9-14% lower for 1900-2000, match our values in 2065, but are 8% higher in 2100. Thus the present study fits well between the values from HAMOCC and the strictly thermodynamic calculation, except for the projection after 2065. However, this can partly be justified with higher $pCO_{2,atm}$ in the A2 emission scenario, than in IS92a.

Gattuso et al. [1998] also estimated the average aragonite saturation state and pH of tropical surface waters. They found nearly the same values (Ω_A=2.93 and pH=7.93) as in the present study (Ω_A=2.99 and pH=7.93), when pCO_2 reaches double preindustrial values (560 ppm).

3.4.3 Possible consequences

Impacts on marine organisms and ecosystems

The impacts of decreasing calcium carbonate saturation and climate change is currently being discussed actively and is subject of many field studies [Kleypas et al., 2006, Hoegh-Guldberg, 2005, Langdon and Atkinson, 2005, Gattuso et al., 1998]. Many effects have to be considered, in order to assess possible impacts. First, the region and depth of habitats of potential endangered species have to be taken into account, because changes of the $CaCO_3$ saturation state depend on the location. Low saturation states and undersaturation of the whole water column is expected first in polar and subpolar regions, whereas the maximum relative changes of the saturation state can be found in the subtropics.

Second, the calcification response of organisms and the interactive effects of saturation state, temperature, light, and nutrients on calcification rates is essential. Open questions are competitive interactions between net production and calcification, as well as between photosynthesis and calcification. It has not yet been adequately determined which component of the carbonate system - CO_3^{2-}, saturation state, pH - controls the calcification rate. How decreased calcification rates will affect the long-term survival of calcifiers is unknown and further studies are required to determine the effect of increased pCO_2 on ecosystems [Kleypas et al., 2006].

Current evidence suggests, that calcification rates of many organisms are strongly dependent on Ω. This has been shown for corals, coralline algae, coccolithophorids, foraminifera, echinoderms, mesocosm coral reef communities and natural coral reef ecosystems [Langdon and Atkinson, 2005]. Coral reef development was associated with $\Omega_A \geq 4.0$ by Kleypas et al. [1999] and Langdon and Atkinson [2005] projected a 40-50% decrease of coral calcification rates by 2065 (Ω_A=3.1) relative to Ω_A=4.6, which corresponds to the conditions in the tropical ocean in 1880. For the same change of Ω_A, studies of Langdon et al. [2000], Broecker et al. [2001], and Reynaud et al. [2003] predict a decline in coral and coral reef calcification of 60% (range

40-83%), whereas for another cluster of data, a decline of only 1% to 18% has been projected [Gattuso et al., 1998, Leclercq et al., 2000, Marubini et al., 2001, 2003, Reynaud et al., 2003].

Multiple taxa of benthic and planktonic calcifiers have shown significant calcification response to carbonate chemistry. Pteropods, which are planktonic calcifiers and an integral component of food webs, are believed to be one of most endangered species, because they build aragonite shells and can be found in the upper 300 m of polar and subpolar waters. At saturation levels expected in the year 2100 under the A2 scenario, a marked dissolution at the growing edge of their shells is found in incubation studies [Orr et al., 2005].

The Arctic Ocean exhibit favorable conditions for calcifiers and $CaCO_3$ conservation in sediments. Sedimentation and respiration rates of organic matter are low and coccolithophorids, foraminifers and pteropods are abundant and can be found in sediments [Jutterström and Anderson, 2005]. However, the present study projects that the top 100 m of the Arctic Ocean will become undersaturated with respect to aragonite by the end of this century under SRES A2.

McNeil et al. [2004] claimed that rising sea surface temperatures (SST) will outweigh negative effects of decreased $[CO_3^{-2}]$ and that annual average coral reef calcification rate even will increase and eventually exceed pre-industrial rates by about 35% by 2100. This suggestion is based on projections of ocean warming and Ω_A (using a coupled atmospheric-ice-ocean carbon cycle model developed by the Commonwealth Scientific Industrial Research Organisation), as well as on empirical relationships between calcification and Ω_A by Langdon et al. [2000], and between calcification and SST by Lough and Barnes [2000]. However, this hypothesis was soundly refuted by a large number of authors [Kleypas et al., 2005], who denote problems with the additivity of SST and Ω_A regarding calcification, as well as the linearity of the calcification response on temperatures, which does not increase indefinitely with SST.

Further, the results from Lough and Barnes [2000] on the long-lived coral Porites on the Great Barrier Reef, which showed no long-term decrease of calcification with decreasing Ω_A, don't seem to be appropriate to derive a general SST-calcification relationship, as done by McNeil et al. [2004]. Additionally the definition of the coral habitat (oceanic area where annual average SST $> 18°C$) was considered to be too simple.

In the present study the projected SST and Ω_A in those regions differ largely from the results by McNeil et al. [2004], based on the IS92a scenario. Ω_A values correspond until 2000, but then diverge; the results by McNeil et al. [2004] are 10% higher in 2050, and even 37% higher in 2100. The mean SST corresponds until 1970, but afterwards, the difference increases steadily up to 1.6°C (+6%). The main reason for these differences is probably the about 30% smaller uptake of atmospheric CO_2 by the ocean in the model used by McNeil et al. [2004]. Despite the higher CO_2 emissions in the IS92a scenario, the cumulative uptake from 1850 to 2100 amounts to only 320 GtC [Matear and Hirst, 1999], whereas the present study yields 459 GtC for the same time period and the SRES A2 scenario. The average uptake for 1980-1989 is 1.35 GtC yr^{-1}, which is 20-25% less than found by Le Quéré et al. [2003] (1.8±0.8 GtC yr^{-1}), Plattner et al. [2002] (1.7±0.6 GtC yr^{-1}), and the present study (1.75 GtC yr^{-1}).

Besides the effects on calcification, increasing SST causes bleaching of corals, when $\Delta T \geq +1.0°C$ in summer. Increase of CO_2 is not known to cause bleaching [Hoegh-Guldberg, 2005]. Other potential influences of climate change on corals could be a direct effect of pH and CO_2 on the physiological performance, sea level rise (though this is believed to be a smaller

problem, if the condition of corals is good), as well as increasing storms and rainfalls (erosion). Gattuso et al. [1999] suggested that pH decrease could change membrane permeability and conductance or cause changes in the activity of an enzyme involved in some critical pathways related to calcification.
The reduction in ocean pH also has some direct effect on other marine species, e.g. by altering the acid-base balance within cells, which can lead to the dissolution of exoskeletal components, metabolic suppression, reduced protein synthesis and reduced activity. Particularly deep-sea organisms seem to be highly sensitive to even modest pH changes [Seibel and Walsh, 2001, Ishimatsu et al., 2005].

Not much is currently known about the ability of corals to adapt to new conditions or to avoid them through migration, but the speed of the changes is very likely important for the ability to adapt or migrate. The implications of acidification for the biodiversity of coral reefs is also largely unknown, but many organisms are highly dependent on corals, that provide food and shelter. Further there are also possible impacts on people (e.g. that depend directly on corals for daily subsidence) or industries like fishing and tourism [Hoegh-Guldberg, 2005].

Feedbacks on the carbon cycle

Besides the biological impacts, changes in the carbonate chemistry can also affect the air-sea CO_2 flux, and therefore the whole carbon cycle. On long time scales (several 100 years), global changes in the export of $CaCO_3$ relative to that of organic matter can lead to large changes in atmospheric CO_2 through $CaCO_3$ compensation (see 1.2.3).

On shorter time scales, reduced surface export of $CaCO_3$ leads to an increase in surface alkalinity, which will tend to lower oceanic pCO_2, and hence the ability to absorb atmospheric CO_2 is enhanced. Enhanced dissolution of $CaCO_3$ in the ocean results in smaller supply of $CaCO_3$ to the sediments and will eventually also result in greater supply of alkalinity to the surface. From a global prospective, a lowering of the calcification rate and an enhancement of the dissolution of $CaCO_3$ in the upper ocean would increase fossil fuel CO_2 storage in the ocean [Chung et al., 2004].

Finally, elevated atmospheric pCO_2 could lead to additional weathering of terrestrial carbonates, which in turn increases the Ca^{2+} input to oceans. This can partly counteract the decrease in Ω due to the decrease in pH.

3.4.4 Outlook

Further steps not covered in this thesis could include an extended discussion of the impacts of climate change on ocean acidification (e.g. comparison with Cao et al. [2007]), an analysis of the impact of using annual mean values instead of seasonal data when comparing results with observations, as well as of the link to changes in marine productivity (chapter 4). Additionally, the uncertainties could be better constrained using errors of the measurements when comparing results with observations, ensemble simulations, and a quantification of the uncertainties introduced by the model drift and the detrending of variables.

Caveats of the CSM1.4-carbon model with respect to ocean acidification are a missing sediment model and that the calcification and remineralization rates are not calculated dynamically. A sediment model will be especially important for simulations on longer time scales in

order to account for carbonate compensation.
To improve our understanding of the role of $CaCO_3$, the CO_2 uptake by the ocean, and their impacts on changes in the carbonate chemistry and in the carbon cycle, future modeling efforts will be required. These should include dynamic production and remineralization of $CaCO_3$ (both, calcite and aragonite [Gangstø et al., submitted, 2007]), sedimentary response, as well as organism or ecosystem response.
Global and regional models should be considered, because on the one hand $CaCO_3$ is an important component of the global carbon cycle, and on the other hand the impacts of decreasing $CaCO_3$ saturation can be restricted or particularly important to specific regions (e.g. shallow waters or coastal regions).

To assess the impacts on marine organisms and ecosystems, further experiments are needed to understand and quantify the process of calcification and its relation to net carbon production, photosynthesis and changing water temperatures, as well as to estimate their ability to adapt to changed conditions.

Chapter 4

Changes in marine productivity

4.1 Introduction

Marine primary production (PP) and export of organic matter are important elements in the global carbon cycle. They determine the amount of carbon that is used to form organic matter in the surface ocean, as well as the amount that is transported to depth by the biological pump. The vertical flux of carbon has an effect on the partial pressure pCO_2 in the surface waters and hence on the gas exchange between atmosphere and ocean. If there was no such biological pump, the atmospheric CO_2 concentration would be significantly higher than observed [Sarmiento and Gruber, 2004].

For that reason, marine productivity is an important factor in order to assess the impact of future climate change and are subject of ongoing research and discussion. Key questions are: What are the physical and biological controls on primary and export production? How is organic carbon transported, transformed and remineralized below the surface layer? And how does the ocean biogeochemistry respond to climate variability and are there feedbacks on climate change?

Schneider et al. [2007] compares spatial and temporal variability in net primary productivity and particulate organic carbon (POC) export from three different coupled carbon cycle models with observation-based estimates derived from satellite measurements of ocean color and inverse modeling. One of these models is the NCAR CSM1.4-carbon model, and the results from the simulation described in section 2.3 have been used.
Analyzing the period 1985-2004, Schneider et al. [2007] found that the model results confirm the dominant role of the low-latitude, permanently stratified ocean for global PP anomalies. Stronger stratification (higher SST) leads to negative PP anomalies and vice versa. This has also been shown by satellite observations [Behrenfeld et al., 2006]. The global annual amount of PP simulated by the models (24-31 GtC/yr) is considerably lower than satellite-based estimates of around 48 GtC/yr [Behrenfeld et al., 2006].
In the present study, the continuation of these model simulations in a scenario of future climate change (SRES A2, see section 2.3) until the year 2100 is analyzed with respect to changes in marine productivity.
First, a short overview of the models and methods used is given. Then, the projected changes in PP and POC export until the year 2100 are presented and changes in the PP limitation are discussed for the NCAR model. Finally, possible drivers and mechanisms of PP changes

are examined, followed by a short discussion of the main results.

4.2 Methods

4.2.1 Models

The results used in this chapter are based on simulations performed with three fully coupled 3-D atmosphere-ocean climate models (IPSL, MPIM, and NCAR), that include additional carbon cycle modules for the terrestrial and oceanic biospheres.

The IPSL model

The IPSL-CM4-LOOP (IPSL) model consists of the Laboratoire de Météorologie Dynamique atmospheric model (LMDZ-4) with a horizontal resolution of about $3° \times 3°$ and 19 vertical levels [Hourdin et al., 2006], coupled to the OPA-8 ocean model with a horizontal resolution of $2° \times 2° \cdot \cos\phi$ and 31 vertical levels and the LIM sea ice model [Madec et al., 1998]. The terrestrial biosphere is represented by the global vegetation model ORCHIDEE [Krinner et al., 2005], the marine carbon cycle by the PISCES model [Aumont et al., 2003].
PISCES simulates the cycling of carbon, oxygen and the major nutrients determining phytoplankton growth (PO_4, NO_3, NH_4, Si, Fe). Phytoplankton growth is limited by the availability of nutrients, temperature and light. The model has two phytoplankton size classes (small and large), representing nanophytoplankton and diatoms, as well as two zooplankton size classes (small and large), representing microzooplankton and mesozooplankton. For all species the C:N:P ratios are assumed constant (122:16:1), while the internal ratios of Fe:C, Chl:C and Si:C of phytoplankton are predicted by the model.
There are three non-living components of organic carbon in the model: semi-labile dissolved organic carbon (DOC), with a lifetime of several weeks to years, as well as large and small detrital particles, which are fueled by mortality, aggregation, fecal pellet production and grazing. Small detrital particles sink through the water column with a constant sinking speed of 3 m/day, while for large particles the sinking speed increases with depth from a value of 50 m/day at the depth of the mixed layer, increasing to a maximum sinking speed of 425 m/day at 5000 m depth.
For a more detailed description of the PISCES model see Aumont and Bopp [2006] and Gehlen et al. [2006]. Further details and results from the fully coupled model simulation of the IPSL-CM4-LOOP model are given in Friedlingstein et al. [2006].

The MPIM model

The Earth System Model employed at the Max-Planck-Institut für Meteorologie (MPIM) consists of the ECHAM5 [Roeckner et al., 2006] atmospheric model in T63L31 resolution with embedded JSBACH terrestrial biosphere model and the MPIOM physical ocean model, which further includes a sea-ice model [Marsland et al., 2003] and the HAMOCC5.1 marine biogeochemistry model [Maier-Reimer et al., 2005]. The coupling of the marine and atmospheric model components, and in particular the carbon cycles is achieved by using the OASIS coupler.
HAMOCC5.1 is implemented into the MPIOM physical ocean model [Marsland et al., 2003] using a curvilinear coordinate system with a 1.5° nominal resolution where the North Pole

is placed over Greenland, thus providing relatively high horizontal resolution in the Nordic Seas. The vertical resolution is 40 layers, with higher resolution in the upper part of the water column (10 m at the surface to 13 m at 90 m). The marine biogeochemical model HAMOCC5.1 is designed to address large scale/long term features of the marine carbon cycle, rather than to give a complete description of the marine ecosystem. Consequently, HAMOCC5.1 is a NPZD model with two phytoplankton types (opal and calcite producers) and one zooplankton species. The carbonate chemistry is identical to the one described in Maier-Reimer [1993]. A more detailed description of HAMOCC5.1 can be found in [Maier-Reimer et al., 2005], while here only the main features relevant for the described experiments will be outlined.
Marine biological production is limited by the availability of phosphorous, nitrate and iron. Silicate concentrations are used to distinguish the growth of diatoms and coccolithophorides: if silicate is abundant, diatoms grow first, thereby reducing the amount of nutrients available for coccolithophoride growth. The production of calcium carbonate shells occurs in a fixed ratio of the phytoplankton growth (0.2). The model also includes cyanobacteria that take up nitrogen from the atmosphere and transform it immediately into nitrate. Please note that biological production is temperature-independent, assuming that phytoplankton acclimate to local conditions. Global dust deposition fields are used to define the source function of bioavailable iron. Removal of dissolved iron occurs through biological uptake and export and by scavenging, which is described as a relaxation to the deep ocean iron concentration of 0.6 nmol/m^3. In the experiments used here, export of particulate matter is simulated using prescribed settling velocities for opal (30 m/day), calcite shells (30 m/day) and organic carbon (10 m/day). Remineralisation of organic matter depends on the availability of oxygen. In anoxic regions, remineralization using oxygen from denitrification takes place.
HAMOCC5.1 also includes an interactive module to describe the sediment flux at the sea floor. This component simulates pore water chemistry, the solid sediment fraction and interactions between the sediment and the oceanic bottom layer as well as between solid sediment and pore water constituents.

The NCAR model

A comprehensive description of the NCAR CSM1.4-carbon model can be found in chapter 2. Additionally, it is important to note that the total productivity in the NCAR model contains both new and regenerated production, though the regenerated contribution is probably lower than in the real ocean. This is because the total biological productivity is partitioned into sinking POC flux (1/3), equivalent to POC export, and into the formation of dissolved or suspended organic matter (2/3), much of which is remineralized within the model euphotic zone. While not strictly equivalent to primary production as measured by ^{14}C methods, rather net nutrient uptake, NCAR PP is a reasonable proxy for the time and space variability of PP if somewhat underestimating the absolute magnitude. In this study, net nutrient uptake for NCAR is labeled and treated as PP for reasons of simplicity, even though it is not essentially the same.

4.2.2 Experimental design

The experimental design of the SRES A2 scenario simulation performed with the NCAR model has already been described in section 2.3. For the simulations with the other two

models, the same emission scenario has been used, but in contrast to the NCAR model, the IPSL and MPIM models were only forced by CO_2 emissions and did not include CH_4, N_2O, CFCs, volcanic emissions or changes in solar radiation.

Because the output data from the IPSL and MPIM models is on a curvilinear coordinate system, all variables from these two models have been interpolated onto a $1^\circ \times 1^\circ$ rectangular grid using a Gaussian interpolation. For the interpolation, a scale of 2° and a cutoff factor of 2 have been used, which means that basically the data is regridded using a distance weighted average within a $4^\circ \times 4^\circ$-box around the grid points. The variables from the NCAR model have been analyzed using the actual model grid. All results in this chapter are based on annual mean values over the period from 1860 to 2100.

4.3 Results

4.3.1 Projected changes in marine productivity until 2100

All three models show a reduction in the globally integrated annual mean primary production (PP) and POC export the simulation from 1860 to 2100 (table 4.1, figure 4.1). The IPSL model, which also yields the highest preindustrial and present values for PP, shows the largest changes. The PP declines by -8.8 GtC/yr until the end of this century, which is 25% of the simulated preindustrial (1860-1869) production. The other two models show similar reductions of -2.3 GtC/yr and -2.0 GtC/yr, which are 10% and 7% of the preindustrial productivity, respectively. Despite the different preindustrial and present productivity, the IPSL and the NCAR model project about the same PP in 2100 due to the large reduction in the IPSL model, whereas the productivity in the MPIM model always remains about 2 GtC/yr below the one of the NCAR model.
The changes in POC export show very similar patterns as the changes in PP, but in the IPSL model, the relative reduction is about 5% higher than for PP.

The PP changes in the NCAR model are dominated by the North Atlantic, where PP is reduced strongly between 35°N and 60°N (figure 4.2). A slight decrease in PP can also be found in the Atlantic between 20°N and 20°S, in the Pacific at 30°N and north-east of New Zeeland, as well as in the Indian Ocean north of 40°S. Small increases in PP are projected in the Pacific north of 40°N, in the Atlantic and Greenland Sea north of 60°N, and in the Southern Ocean.
In the IPSL model PP changes are more distributed with maximum reductions in the North Atlantic between 40°N and 60°N, in the equatorial Pacific, and at the west coast of Africa. Slight to moderate reductions in PP can be found almost everywhere between 60°N and 40°S, except for the North Pacific around 45°N and the west coast of South America around 30°S, where a slight increase in PP is projected. In the Southern Ocean slight increases in PP are found, except south of New Zeeland.
The MPIM model projects the maximum decrease of PP in the equatorial Pacific and Atlantic, as well as in the north of the Indian Ocean. Increased PP is projected in the Southern Ocean near the coast of Antarctica, in the Arctic, and in the eastern Pacific around 30°S.

In order to quantify and compare the PP changes in different regions, the changes in integrated PP were calculated for nine regions: Arctic; North Pacific and Atlantic (north of 30°N); tropical Pacific, Atlantic and Indian (30°N-30°S); south Pacific, Atlantic and Indian (south

Primary production	*IPSL*	*MPIM*	*NCAR*
PP_{glob} 1865 [GtC yr^{-1}]	34.8	23.9	28.4
PP_{glob} 2000 [GtC yr^{-1}]	30.7	23.7	27.5
PP_{glob} 2095 [GtC yr^{-1}]	26.0	21.6	26.4
ΔPP_{glob} 1865-2000 [GtC yr^{-1}]	-4.1 (-12%)	-0.2 (-1%)	-0.9 (-3%)
ΔPP_{glob} 2000-2095 [GtC yr^{-1}]	-4.7 (-15%)	-2.1 (-9%)	-1.1 (-4%)
ΔPP_{glob} 1865-2095 [GtC yr^{-1}]	-8.8 (-25%)	-2.3 (-10%)	-2.0 (-7%)
POC export	*IPSL*	*MPIM*	*NCAR*
EP_{glob} 1865 [GtC yr^{-1}]	9.1	5.0	9.4
EP_{glob} 2000 [GtC yr^{-1}]	8.0	5.0	9.0
EP_{glob} 2095 [GtC yr^{-1}]	6.4	4.5	8.7
ΔEP_{glob} 1865-2000 [GtC yr^{-1}]	-1.1 (-12%)	0.0 (0%)	-0.4 (-4%)
ΔEP_{glob} 2000-2095 [GtC yr^{-1}]	-1.6 (-20%)	-0.5 (-10%)	-0.3 (-3%)
ΔEP_{glob} 1865-2095 [GtC yr^{-1}]	-2.7 (-30%)	-0.5 (-10%)	-0.7 (-7%)

Table 4.1: Integrated global annual primary production (PP) and POC export (EP) for the three models IPSL, MPIM and NCAR. ΔPP and ΔEP indicate the corresponding changes. The values are averages over the periods 1860-1869 (1865), 1985-2004 (2000), and 2090-2099 (2095).

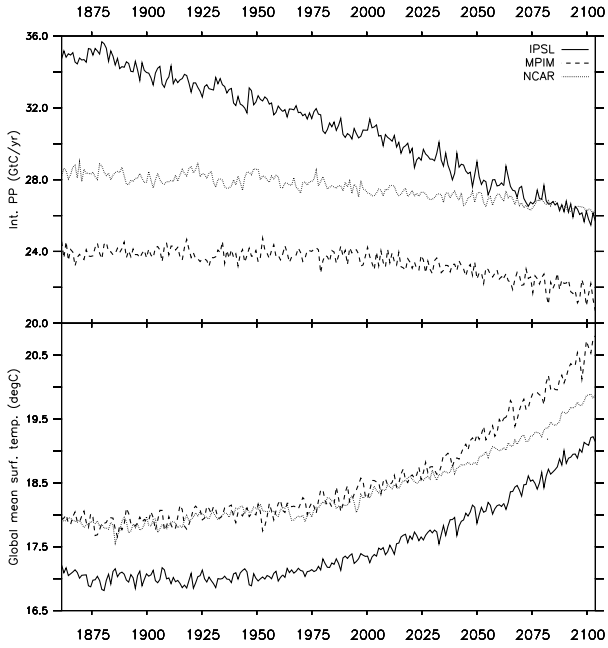

Figure 4.1: Vertically integrated annual mean primary production (PP, $\frac{\text{GtC}}{\text{yr}}$) and surface temperature (°C), as simulated by the IPSL (solid line), MPIM (dashed line), and the NCAR (dotted line) models for the period 1860-2100.

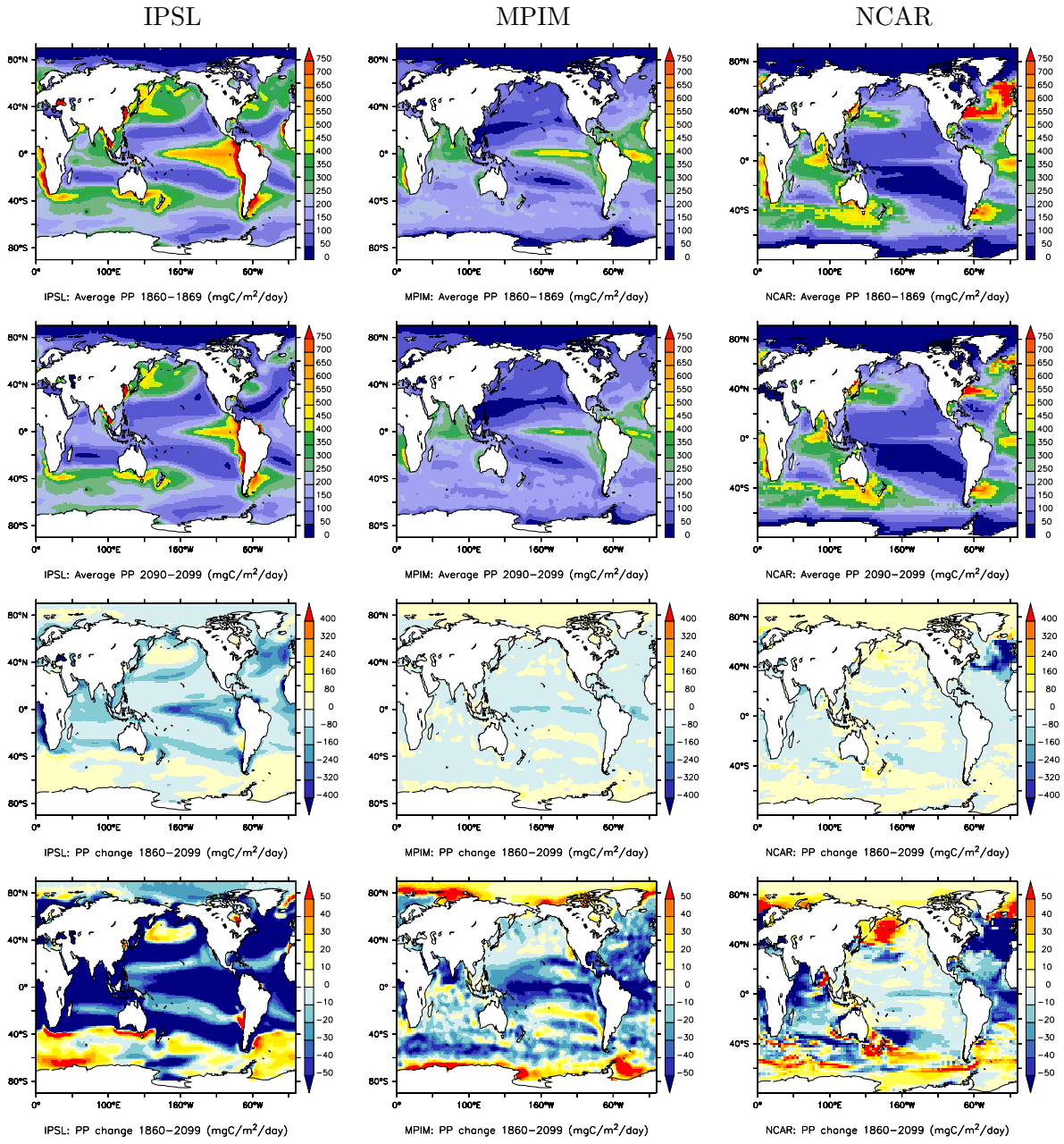

Figure 4.2: Vertically integrated annual mean primary production (PP) in $\frac{\text{mgC}}{\text{m}^2\ \text{day}}$, simulated by the IPSL (left column), MPIM (middle column), and the NCAR (right column) models. The top row shows the decadal average PP for 1860-1869, the second row for 2090-2099. The third and the fourth row both show PP changes between the decades 1860-1869 and 2090-2099, but the bottom row focus on small changes of $\pm 50 \frac{\text{mgC}}{\text{m}^2\ \text{day}}$.

of 30°S).
The spatial pattern of the changes is quite similar in the IPSL and the MPIM model. In both models the Pacific accounts for about half of the PP reduction (IPSL: 52%, MPIM: 48%) and the Atlantic for about a third (IPSL: 32%, MPIM: 38%). In the NCAR model, 83% of the reduction takes place in the Atlantic, while the PP in the Pacific increases even slightly because the reduction in the Tropics is compensated by increases in the north and south. However, despite the large contribution of the Atlantic to the global PP reduction in the NCAR model, in terms of absolute values the decrease in the Atlantic (-1.7 GtC/yr) lies between the projections of the MPIM (-0.9 GtC/yr) and the IPSL (-2.7 GtC/yr) models.
In all three models the Indian Ocean accounts for about the same fraction of the global PP reduction (IPSL: 15%, MPIM: 15%, NCAR: 20%). In the Arctic the NCAR and MPIM models show an increase in PP (1.5% and 3% of the global PP change, respectively), whereas in the IPSL model the Arctic accounts for 1% of the global PP reduction.

Looking at the changes at different latitudes, we find that in the IPSL and MPIM models, 72% and 77% of the reduction takes place in the Tropics (here defined as 30°N-30°S), 17% and 9% north of 30°N (except Arctic), and 10% and 17% south of 30°S, respectively. Again, the picture looks different in the NCAR model, where 57% of the PP reduction can be found north of 30°N (except Arctic) and 48% in the Tropics. South of 30°S the NCAR model projects a slight increase of 0.06 GtC/yr PP (3% of the global PP change).

Overall, there are relatively large differences between the different models in projecting changes in PP. This is not surprising because there are already large differences when simulating present-day PP [Schneider et al., 2007]. However, the models agree mostly on the reduction of PP in the low-latitude Atlantic and Indian Ocean, as well as on the slight increase of PP in high latitude regions (parts of the Arctic and the Southern Ocean). They agree partly on the reduction of PP in the low-latitude Pacific (IPSL and MPIM) and on the slight increase of PP in the North Pacific (IPSL and NCAR).

4.3.2 Changes in PP limitation in the NCAR model

In order to attribute the changes in PP to changes in nutrient and light availability, mixed layer depth (MLD), and temperature, the respective factors have been calculated from annual mean data in the same way as the NCAR model does (see section 2.2.1). Figure 4.3 shows these factors for the years 1985-2004 and figure 4.4 shows the changes from 1860 to 2099.

From this it follows that the large reduction of PP in the North Atlantic can mostly be attributed to a decrease in mixed layer depth. North-west of Europe, the mixed layer is very deep (more than 200 m in a large area) in 1860. From 1860 to 2099 the MLD decreases by more than 100 m in that region, but only south of 60°N (figure 4.5). North of 60°N it remains at great depth or even increases. Therefore the MLD scaling is switched off in a relatively large area, where the MLD is below the compensation depth ($z_c = 75$m) in 1860 (PP scaling by z_{ml}/z_c) and above z_c in 2099 (no PP scaling). North of 60°N the MLD scaling factor is increased where the mixed layer is deeper than in 1860.
The changes in the MLD scaling factor are partly compensated by changes in the light limitation, because more/less light is available in the production zone, when the MLD decreases/increases at depths below z_{comp}. The net effect of light limitation and MLD scaling leads to an increased PP limitation by 10-50% in a large area of the North Atlantic between

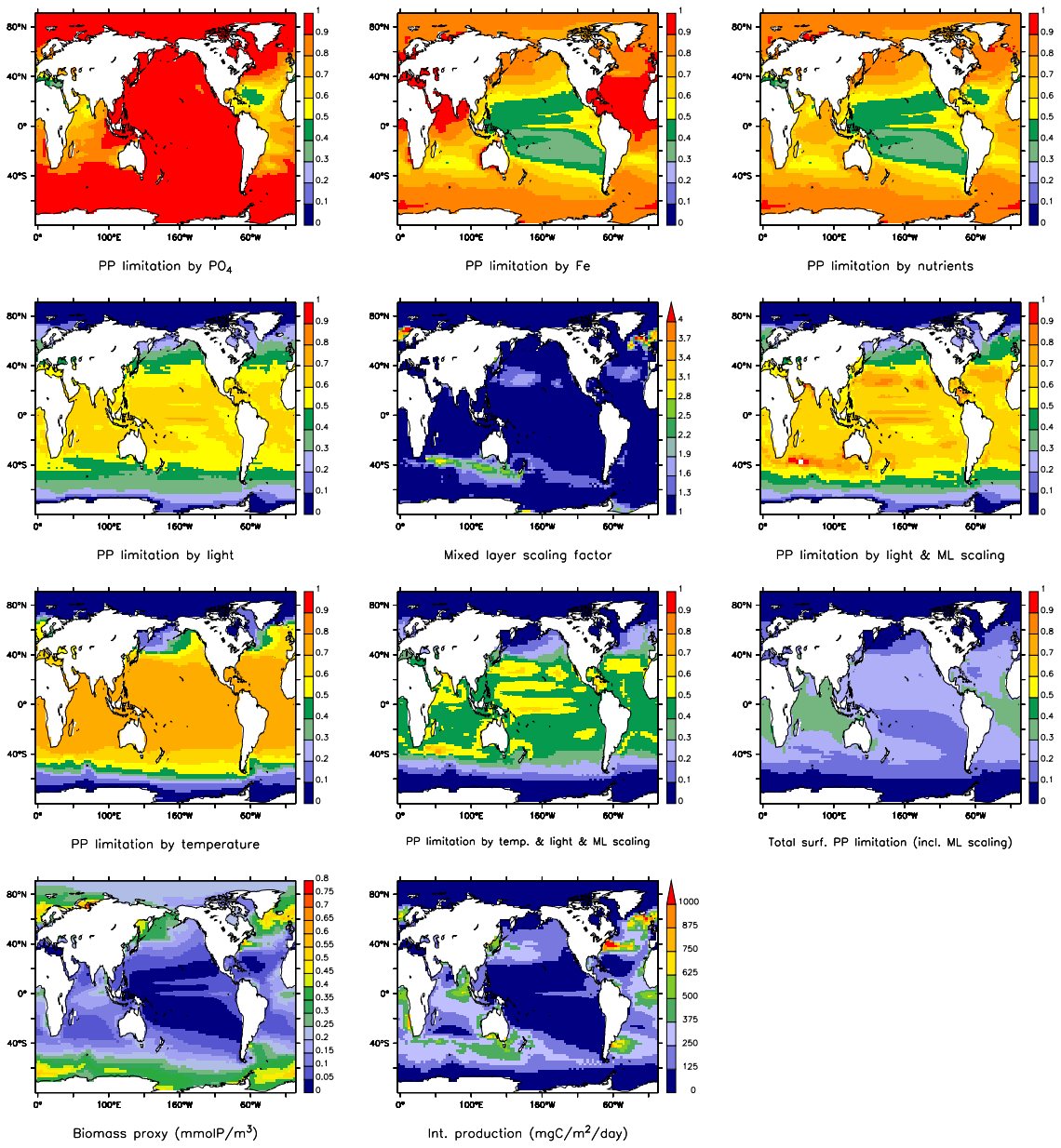

Figure 4.3: Factors that determine PP in the NCAR model. The figures show the present simulated factors (average 1985-2004) averaged over the compensation depth (75 m), except the figure in the bottom right panel, which shows the present simulated vertically integrated PP in mgC/m^2/day. The top row shows the nutrient limitation factors (phosphate, iron, and the minimum of both). The second row shows the light limitation factor, the mixed layer scaling factor, and the combination of both. The third row shows the temperature limitation factor, the combined effect of temperature, light, and mixed layer scaling, as well as the combination of all limiting/scaling factors. The bottom row shows the biomass proxy (mmolP/m^3) and the resulting PP.

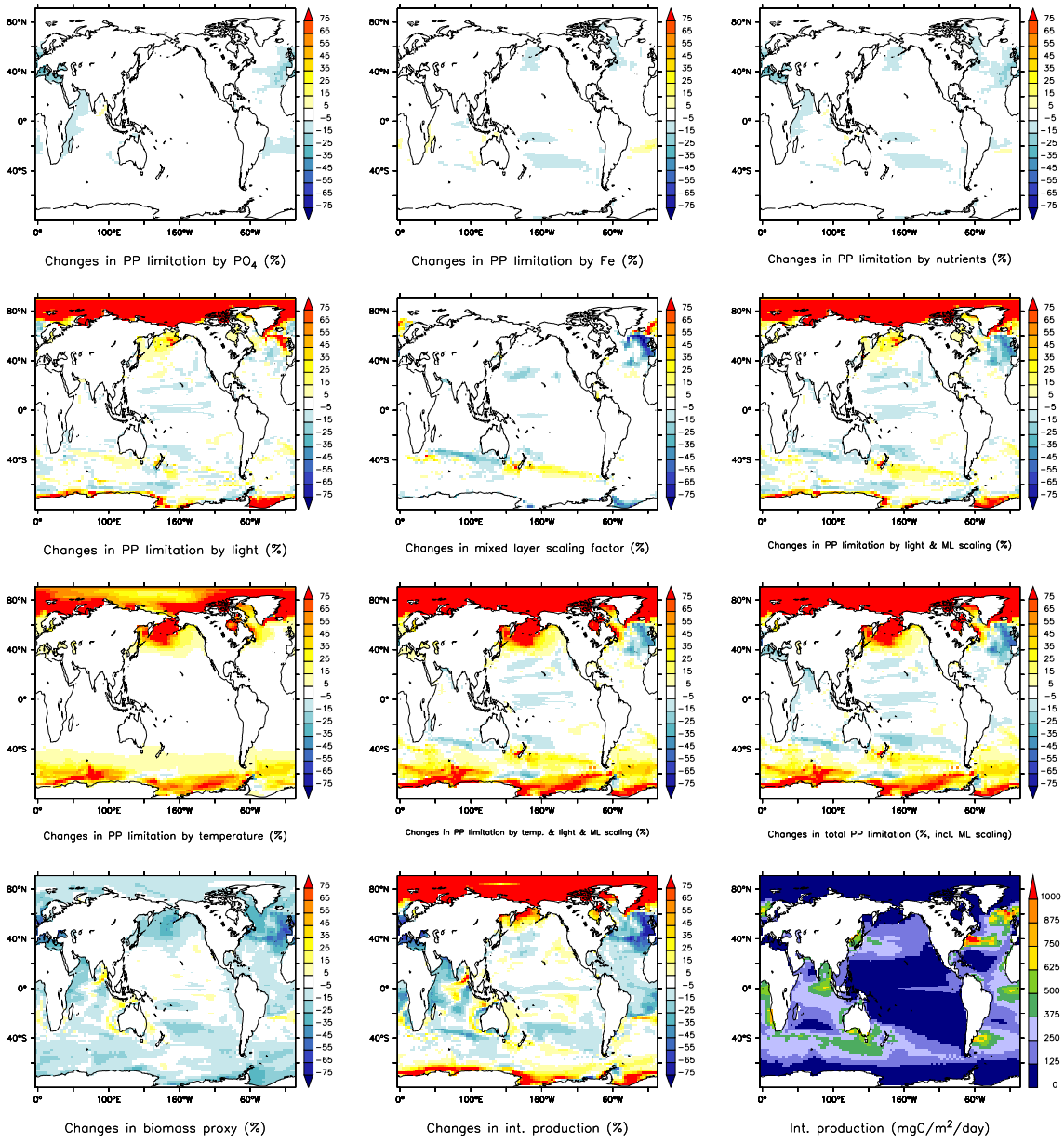

Figure 4.4: Changes in factors that determine PP in the NCAR model. The figures show relative changes from the average of the first decade (1860-1869) to the average of the last decade (2090-2099) in percent, except the figure in the bottom right panel, which shows the present simulated PP (average 1985-2004) in mgC/m^2/day. All values refer to averages over the compensation depth (75 m). Positive values indicate changes that enhance PP, negative values indicate changes that tend to reduce PP. The top row shows changes in nutrient limitation factors (phosphate, iron, and the minimum of both). The second row shows changes in the light limitation factor, mixed layer scaling factor, and in the combination of both. The third row shows changes in the temperature limitation factor, in the combined effect of temperature, light, and mixed layer scaling, as well as in the combination of all limiting/scaling factors. The bottom row shows changes in the biomass proxy and the resulting PP change.

40°N and 60°N. Additionally this trend is enhanced by stronger nutrient limitation (PO_4) in the East Atlantic between 30°N and 60°N.

At high latitudes (north and south of 60°) and in the North Pacific (north of 40°N) the PP limitation is strongly reduced because of higher temperatures and more light availability. In the North Pacific the PP limitation declines mainly because of higher temperatures.
At latitudes between 40°N and 40°S the PP limitation is slightly enhanced, because of less light availability (including reduced MLD scaling) and increased iron limitation in the south. Enhanced phosphate limitation is the main cause for decreased PP in the north and west Indian Ocean.
In the Southern Ocean, there are almost no changes in nutrient limitation. There, the pattern is produced by a decrease in the MLD scaling factor in the South Indian Ocean and an increase in the South Pacific around 40°S, as well as by increased light limitation at some spots, and a reduced temperature limitation in almost the entire Southern Ocean.
Because PP depends also on the biomass proxy (i.e. phosphate and iron concentrations), the actual PP can also change where the limitation factors are unchanged. For example this is the case in the Indian Ocean and in the Atlantic at low latitudes. The biomass proxy is reduced in most regions, except in the Pacific 30°N-30°S. Only at some spots around Australia in the east of India and in the South Atlantic around 20°S, the biomass proxy increases.

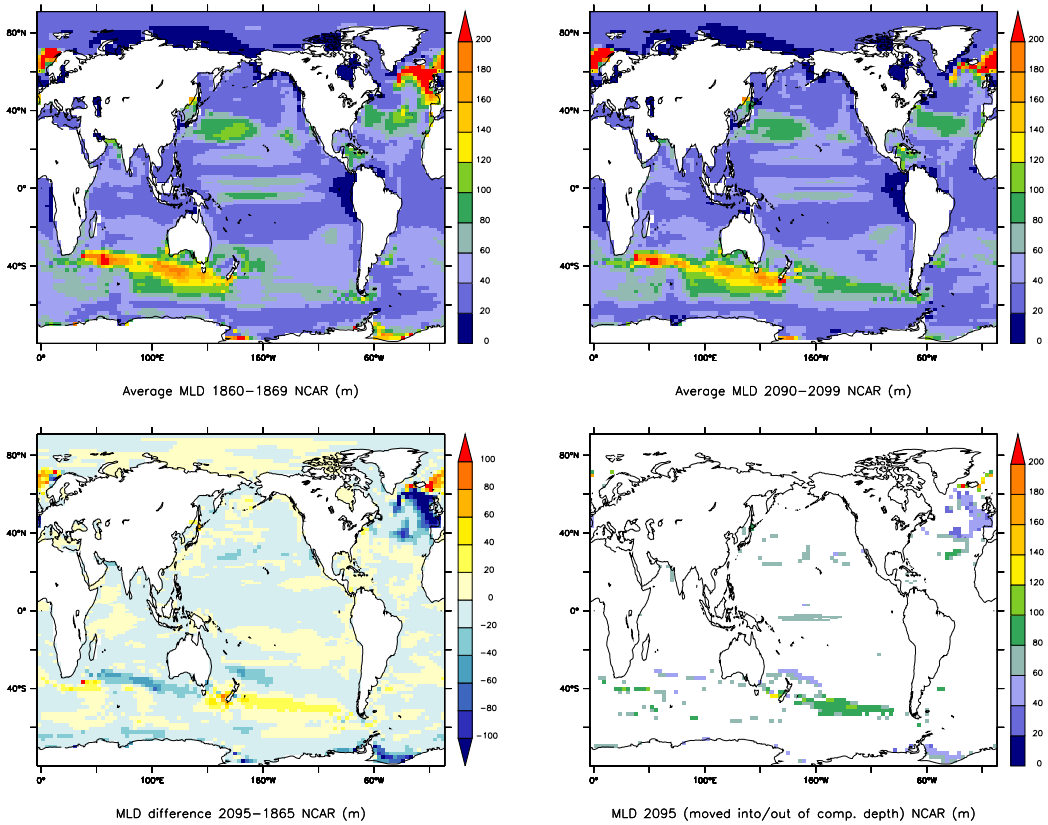

Figure 4.5: Changes in simulated mixed layer depth (MLD) in the NCAR model. The top panels show the average MLD in 1860-1869 (left) and in 2090-2099 (right). The bottom panels show the MLD changes (left) and the average MLD in 1860-1869, where the MLD either changes from below the compensation depth (75 m) into the production zone or from the production zone below the compensation depth (right).

4.3.3 Drivers of PP changes

The global perspective

A first order approach to identify drivers of PP changes is to look for simultaneous changes in the global mean of other tracers and physical properties. The models project an increase of global annual mean SST by 12% (IPSL), 14% (MPIM), and 10% (NCAR) from 1860 to 2099, which is in coincidence with increased stratification and reduced surface PO_4 and NO_3 concentrations (figure 4.6). The stratification index, which is defined as the water density difference between 0 m and 200 m depth according to Behrenfeld et al. [2006] and Schneider et al. [2007], increases by 21% (IPSL), 26% (MPIM), and 13% (NCAR). Global mean surface PO_4/NO_3 concentrations decline by -34% (IPSL), -11% (MPIM), and -4% (NCAR).
Compared to the other two models, the NCAR model shows a small response of MLD and PO_4 concentrations to rising SST and stratification, whereas the MPIM model shows a relatively strong response of the MLD. In the IPSL model, PO_4 and NO_3 concentrations experience a comparatively strong decrease.
Surface iron concentrations are strongly elevated in the IPSL model (30%), whereas in the MPIM and NCAR models decreases by 1%-3%. In all three models the global mean surface salinity (not shown) declines very slightly by -0.15 psu (IPSL), -0.12 psu (MPIM), and -0.09 psu (NCAR) and the short wave surface heat flux (QSW) is reduced by 1-2% in the NCAR and MPIM models and increased by about 1% in the IPSL model.

The reduction of global annual mean PP has about the same order of magnitude than the reduction of PO_4/NO_3 in the MPIM and IPSL models (figure 4.6). In the NCAR model PP is reduced more than surface PO_4 concentrations. From this global perspective it seems that increased stratification and reduced PO_4/NO_3 concentrations are main causes for the PP reduction in all models. Additionally, the MLD reduction doesn't seem to have a large effect on PP in the IPSL and MPIM models, but is more important in the NCAR model. Iron also is less likely a main cause for PP reduction on the global scale in the MPIM and IPSL models, whereas in the NCAR model the decrease in surface iron concentration might enforce global PP. Changes in surface irradiance doesn't seem to play an important role on the global scale in any of the three models.
Only in the IPSL model there is a difference between the reduction of POC export and the reduction of PP. The reduction is about 5% less than the PP reduction and the variations in time are a little bit smoothed out, compared to PP. In the MPIM and NCAR models POC export and PP changes are equal. (In the NCAR model POC export is a fixed ratio of PP by model design.)
An interesting feature is the export of calcium carbonate ($CaCO_3$, not shown), which is strongly reduced (by about 34%) in the IPSL model like the PP and the PO_4/NO_3 concentrations, but significantly increased in the MPIM model simulation (+21%). $CaCO_3$ export is not available for the NCAR model.

PP reduction in the North Atlantic

The North Atlantic (north of 30°N) is an interesting region because all three models show large relative changes in different variables there (figure 4.7). The stratification index increases more than in any other region (except the Arctic in the NCAR model): 90% in the IPSL model, 45% in the MPIM model, and 40% in the NCAR model. Simultanously PP is reduced

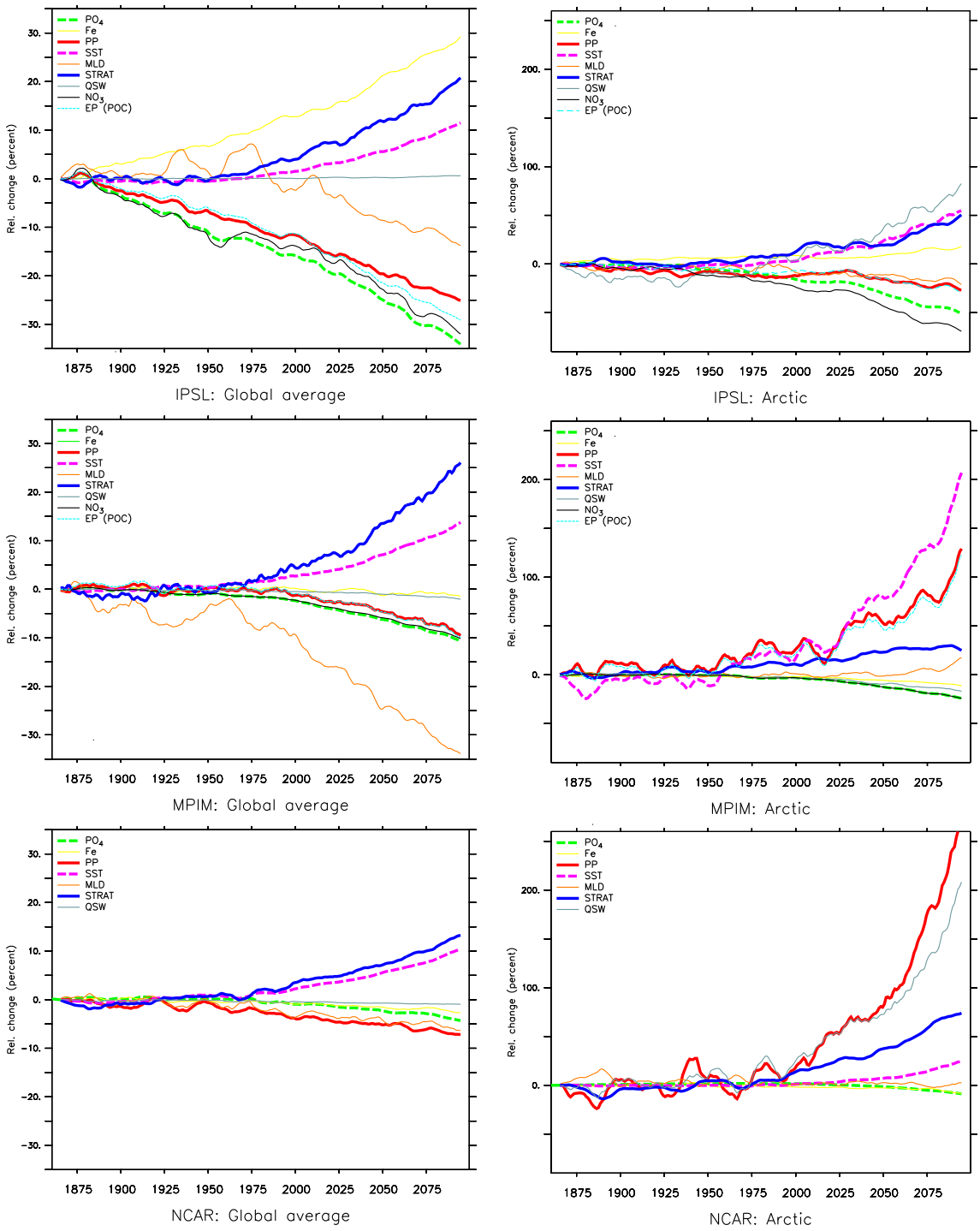

Figure 4.6: Temporal evolution (1860-2099) of different variables possibly related to PP, on the global scale (left column) and in the Arctic (right column) as simulated by the IPSL (top), MPIM (middle), and NCAR (bottom) models. Changes in surface nutrient concentrations (PO_4, NO_3, Fe; averaged over top 75 m), vertically integrated PP, surface temperatures (SST, averaged over top 75 m), mixed layer depth (MLD), stratification index (STRAT), short wave heat flux (QSW) at the surface, and POC export (EP) are shown. The figures show changes in percent relative to the average of the first decade (1860-1869). Interannual variability has been removed using a boxcar smoother (running mean) with a window length of 10 years. For the NCAR model NO_3 is not available and POC export is not shown, because it is a fixed ratio of PP.

strongly in the IPSL (-65%) and NCAR (-35%) models. In the MPIM model the reduction is less accentuated, but slightly larger than the global mean, though.
In the NCAR simulation a strong inverse relation between stratification and PP ($R^2 > 0.5$), as well as a positive correlation with MLD ($R^2 > 0.7$) is visible (figures 4.7 and 4.9), PO_4 is also reduced by about 26% but shows no significant correlation with PP (figure 4.10). In the region between 40°N and 60°N, where iron becomes the limiting factor, a strong correlation ($R^2 > 0.7$) between iron and PP reduction was found. Because the PP changes are correlated more with decreased surface salinity than with increased SST, the increase in stratification seems to be related primarily to changes in salinity, rather than in SST.
The PP reduction in the North Atlantic for the IPSL model seems to be more related to PO_4/NO_3 reductions. There is a less strong connection with MLD and iron is not limiting, as concentrations increase strongly, but similar salinity and stratification correlation patterns as in the NCAR model can be found.

The North Pacific

In the North Pacific (north of 30°N) the NCAR model projects a slight increase in PP mainly because of less light and temperature limitation (figure 4.7). SST increases by about 30% and QSW by about 5%, which results in a net PP increase, despite of stronger stratification, a slightly reduced MLD, and less iron availability, that counteract the PP increase. The PP increase in the very north is correlated ($R^2 > 0.5$) with increased QSW and the PP decrease in the west around 30°N is correlated with decreasing iron concentration and MLD (figures 4.9 and 4.10).
The MPIM model shows only very little PP variations in the North Pacific, which are most likely related to variations in iron availability and MLD.
In the IPSL simulation PP is reduced by about 25%, which is less than in the North Atlantic, despite the fact that PO_4 and NO_3 surface concentrations are reduced by nearly the same amount as in the North Atlantic. Although a slightly higher SST increase, the increase in stratification and the decrease of MLD is less strong than in the North Atlantic. Additionally, increased iron availability counteracts the PP decrease, because iron is a limiting nutrient in the North Pacific.

PP changes in the low latitude ocean

In the low latitude ocean (30°N-30°S), all three models show a reduction of PP. The IPSL model projects a PP reduction of about 60% for the low latitudes of all three basins, Atlantic, Pacific, and Indian Ocean. This reduction comes together with a similar but somewhat smaller reduction in surface PO_4 and a very strong (80-90%) decline of surface NO_3 concentrations, which is the major limiting nutrient in the low latitude ocean [Schneider et al., 2007]. Stratification is increased by about 20% in the Indian and Pacific (figure 4.8), while it increases only by a few percent in the Atlantic. The MLD decreases only slightly in the Pacific and Indian Ocean.
In the MPIM simulation the PP reduction in the low latitude Pacific is correlated weakly ($R^2 > 0.3$) with increased stratification, reduced MLD, and strongly ($R^2 > 0.7$) with less iron availability (figures 4.8 and 4.10). In the Atlantic, the stratification increase and the MLD decrease are weaker than in the Pacific, but PP is reduced by about the same factor (about -15%), because the decline of PO_4 and NO_3 concentrations is relatively strong. In

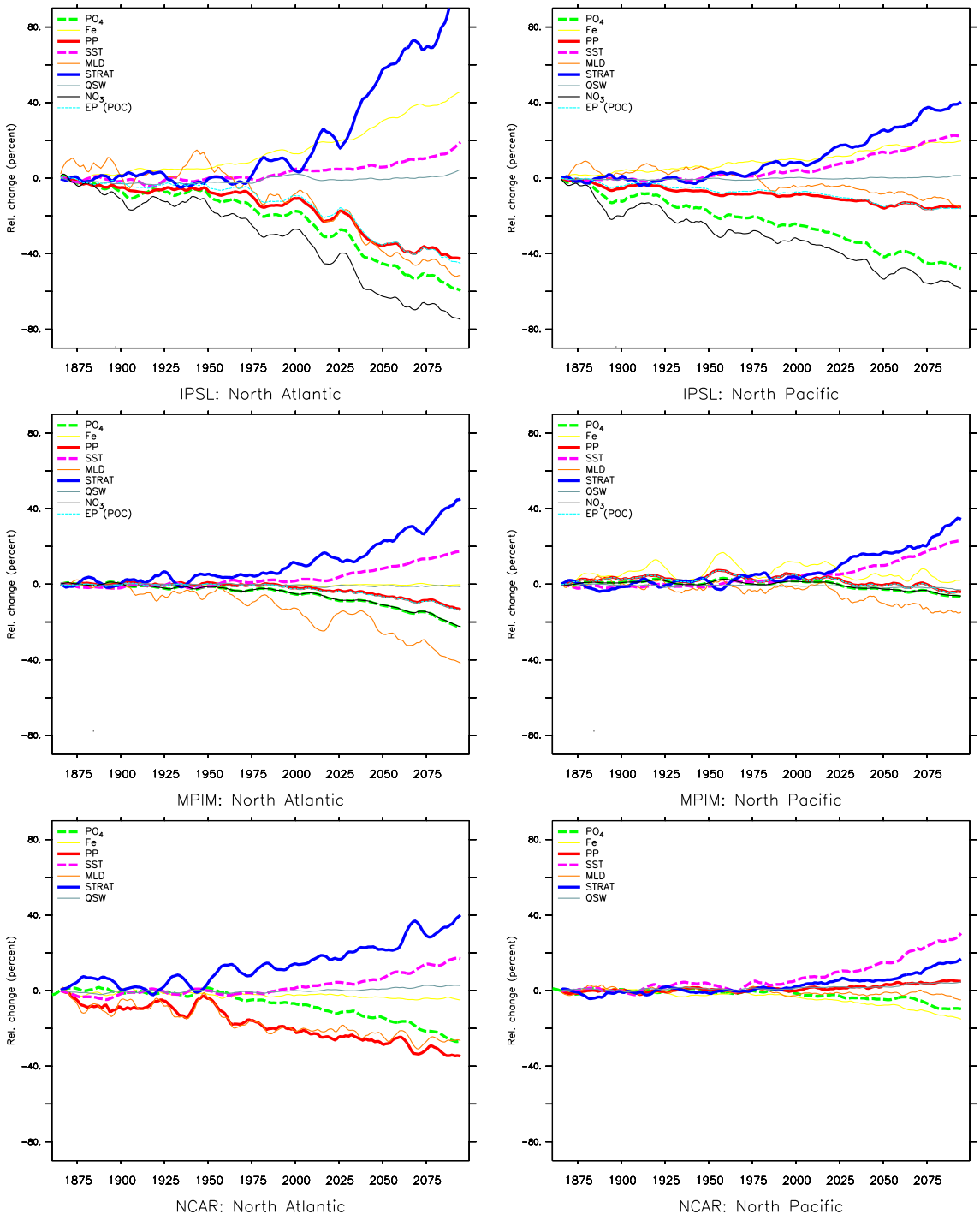

Figure 4.7: Temporal evolution (1860-2099) of different variables possibly related to PP, in the North Atlantic (north of 30°N, left column) and in the North Pacific (north of 30°N, right column). See figure 4.6 for a more detailed description.

the Indian Ocean there is only a small reduction of PP by about 5%, most probably because iron concentraions, which is the main limiting nutrient, increase slightly, while PO_4 and NO_3 concentrations decline with increasing stratification and reduced MLD.
The NCAR model projects a PP reduction of -10% in the low latitude Atlantic, which shows a weak correlation with increasing stratification and the slightly reduced MLD. Surface PO_4, that is the limiting nutrient in that region, is reduced by about 15%. Surface iron concentrations increase slightly and iron is not limiting in a large part of that region. In the low latitude Pacific the opposite is the case; the surface iron concentration declines with increasing stratification and decreasing MLD (figure 4.8). Because iron is the major limiting nutrient in the Pacific, there's a strong correlation between reduced iron availability and PP ($R^2 > 0.7$, figure 4.10). Again, the PP decrease (-8%) in the Indian Ocean is mainly determined by reduced PO_4 availability in the west (due to increased stratification) and reduced MLD in the south. This reduction is partly counteracted by increased upwelling north-east of India.

The Southern Ocean

The IPSL model shows only little changes in the Atlantic sector of the Southern Ocean (south of 30°S). Only SST and iron concentrations are increased by 2100 (like everywhere in the IPSL model). PP is reduced only slightly, together with surface PO_4 and NO_3, that is reduced by about 10%. In the South Pacific the changes are similar that in the North Pacific; PP is reduced by about 25% with increasing stratification and strongly reduced PO_4 and NO_3 surface concentrations (figure 4.8). Again, the PP reduction is partly absorbed by enhanced iron availability and possibly also by more light availability (QSW increase). This is even more true for the South Indian, where the net PP reduction is small, despite increased stratificaion and reduced PO_4/NO_3 concentrations.
In the MPIM simulation the Southern Ocean presents a fairly homogeneous picture. PP is reduced only slightly, the largest decreases can be found in the South Indian (about -8%). Obviously the increased stratification and the large decrease of MLD (up to -60% in the South Atlantic) do not have a big effect on nutrient concentrations and on PP in the Southern Ocean. In contrast to the other two models, QSW is reduced in the Southern Ocean.
The NCAR model projects a slight net increase of PP (3% of the global PP change) in the Southern Ocean, although the stratification increases by about 17% (South Atlantic and Pacific) to 27% (South Indian) and the surface iron availability decreases by about -10%. The PP reduction is compensated by less temperature and light limitation. Only in the South Indian PP is reduced slightly due to the large stratification increase and the MLD decrease.

The Arctic

The MPIM and NCAR models project a large relative increase of PP in the Arctic (MPIM: +120%, NCAR: +260%, figure 4.6). These large values arise, because the PP values are close to zero in the Arctic. In terms of absolute values these increases account only for 3% and 1.5% of the global PP changes, respectively. In the MPIM simulation PP increases mainly due to increasing SST, whereas in the NCAR simulation PP increases due to a large increase in light availability (QSW) and rised SST. In both models, stratification and MLD increase, while nutrient concentrations decline, but these changes have only a small effect on PP.
The IPSL model also projects a large increase of QSW in the Arctic, but nevertheless PP is reduced by about 60%, possibly due to a large increase in stratification and declined MLD

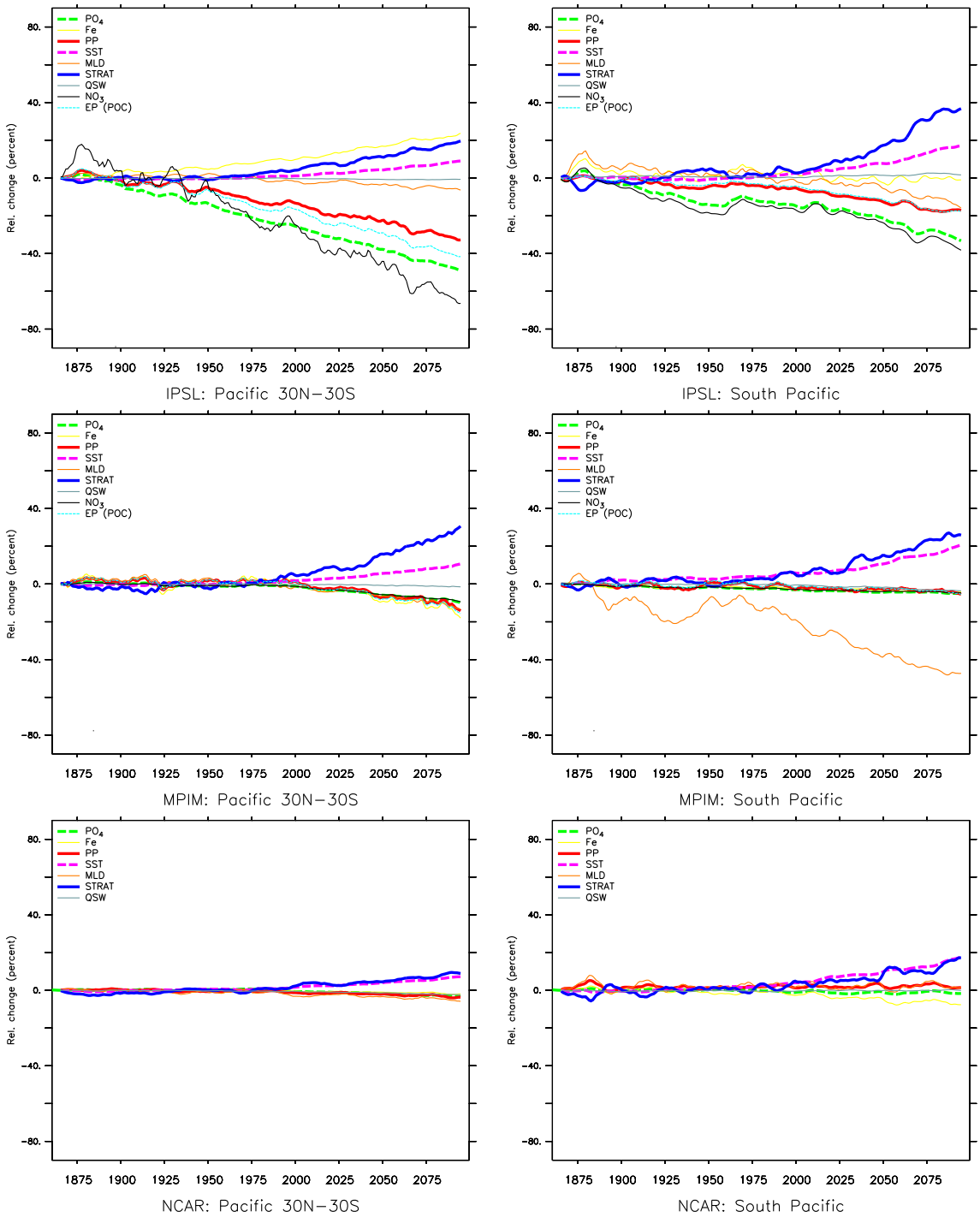

Figure 4.8: Temporal evolution (1860-2099) of different variables possibly related to PP, in the Pacific between 30°N and 30°S (left column) and in the South Pacific (south of 30°S, right column). See figure 4.6 for a more detailed description.

together with strongly reduced PO_4 and NO_3 availability.

Changes in ocean circulation

In the NCAR model the meridional overturning circulation (MOC) is slightly enhanced in the Southern Ocean around 55°S during the simulation from 1860 to 2099 (figure 4.11), potentially leading to more upwelling and nutrient supply to the surface. This corresponds with relatively small decreases in PO_4 concentrations in the Southern Ocean compared to the global average (figure 4.8).
The maximum overturning in the Atlantic is reduced by about 5 Sv from about 20 Sv to 15 Sv. This eventually results in less transport of nutrients the high production regions in the North Atlantic leading to a large decrease in PO_4 concentrations (figure 4.7). The North Atlantic deep water formation weakens and the transport of water masses from the surface to the deep ocean between 40°N and 70°N is reduced. This corresponds with increased stratification and reduced mixed layer depth, due to lower surface salinity, and possibly results in less transport of dissolved and particulate organic matter to the deep ocean and, on longer time scales, to other ocean basins.
In the Pacific and Indian Ocean, the upward transport of North Atlantic and North Indian deep water is reduced, as well as the northward transport of upwelled waters from the equator. This potentially reduces the nutrient flux from the deep ocean to the surface in the equatorial and in the North Pacific and Indian Ocean.

As a measure of upwelling and sinking of water masses in the productive zone, the vertical transport at 75 m has been chosen. Both, the IPSL and the NCAR model project a large decrease in upwelling in the equatorial Pacific (figure 4.12). Relatively large changes can also be found in the North Atlantic (decreased upwelling as well as decreased sinking) and in the Southern Ocean.

4.4 Discussion

All three models show a significant reduction in global primary productivity during the simulations from 1860 to 2100 under the SRES A2 emission scenario. Global decadal mean PP declines by -7% to -25% of the respective preindustrial value. The NCAR model, which also shows the smallest relative changes in SST (rel. to climate sensitivity), stratification, PO_4 surface concentrations, mixed layer depth, and surface salinity on the global scale, projects the smallest reduction. On the other hand, the MPIM model, which shows the highest relative changes in SST, stratification, and MLD (but not in PO_4 concentrations and salinity), projects a relatively small reduction in PP, compared to the IPSL model, which projects by far the largest (relative and absolute) changes in global annual mean PP, together with the largest changes in surface PO_4 concentrations and surface salinity.

The PP changes in the NCAR simulation seem to be dominated by the North Atlantic caused by increased stratification, reduced MLD, and reduced iron availability. Iron also seems to play a major role at low and mid latitudes in the Pacific and Indian Ocean. The mixed layer depths is a major factor in the North Pacific and also in other regions, due to the design of the NCAR model, that uses mixed layer scaling to calculate production of organic matter. The changes in the IPSL and MPIM simulations are more distributed. In the IPSL simulation, the PP reductions in the low-latitude ocean and in the North Atlantic are correlated with reductions

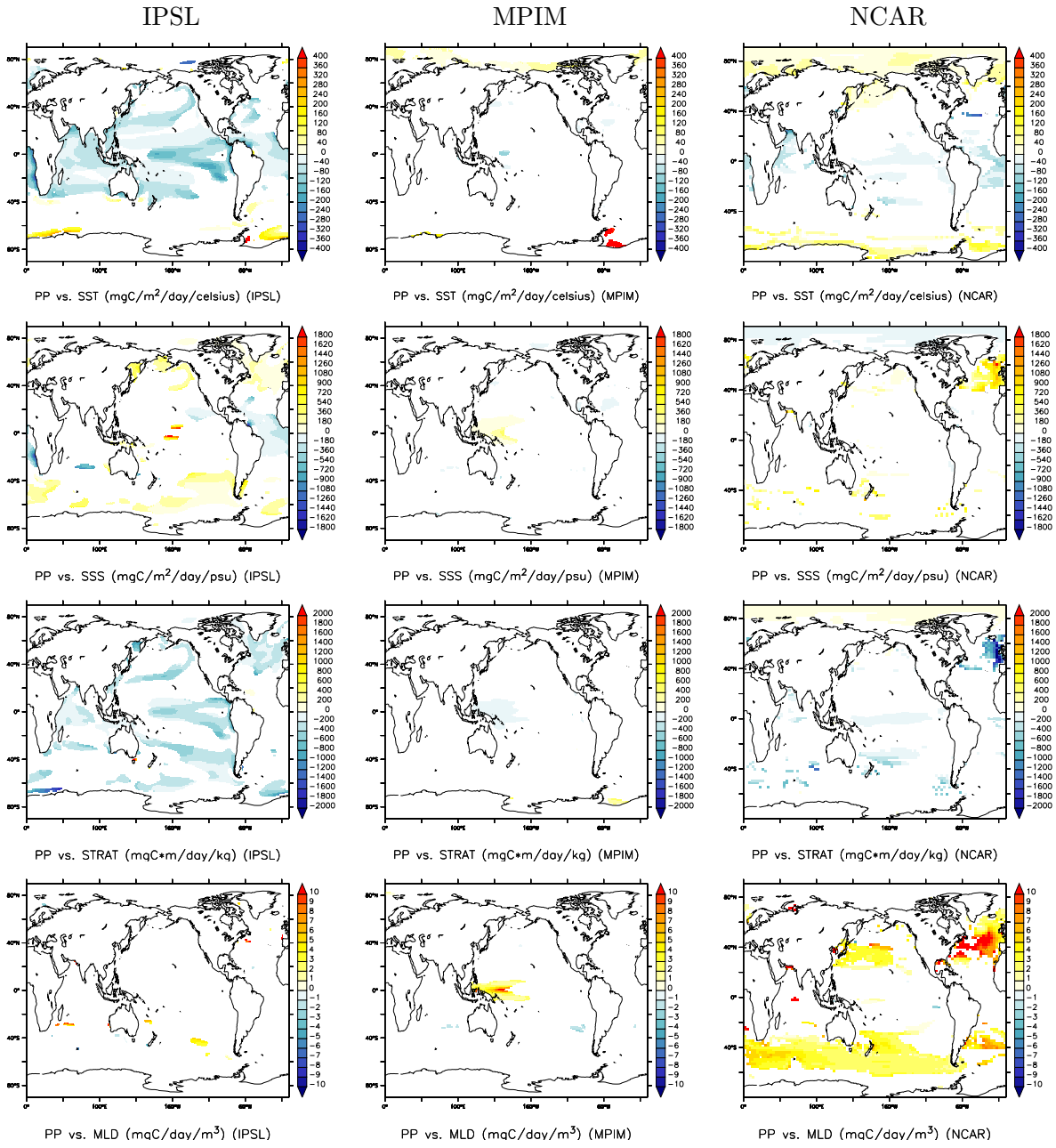

Figure 4.9: Linear correlation between vertically integrated annual mean PP and temperature (T, top row), salinity (S, second row), stratification index (STRAT, third row), and mixed layer depth (MLD, bottom row) as simulated by the IPSL (left column), MPIM (middle column), and NCAR (right column) models. The regression has been calculated for each grid cell using the time series from 1860 to 2100. For temperature and salinity, averages over the top 75 m have been used. The figures show the regression slopes (ΔPP [$\frac{\mathrm{mgC}}{\mathrm{m^2\ day}}$] per ΔT [°C], ΔS [psu], ΔSTRAT [$\frac{\mathrm{kg}}{\mathrm{m^3}}$], and ΔMLD [m]), where $R^2 > 0.5$.

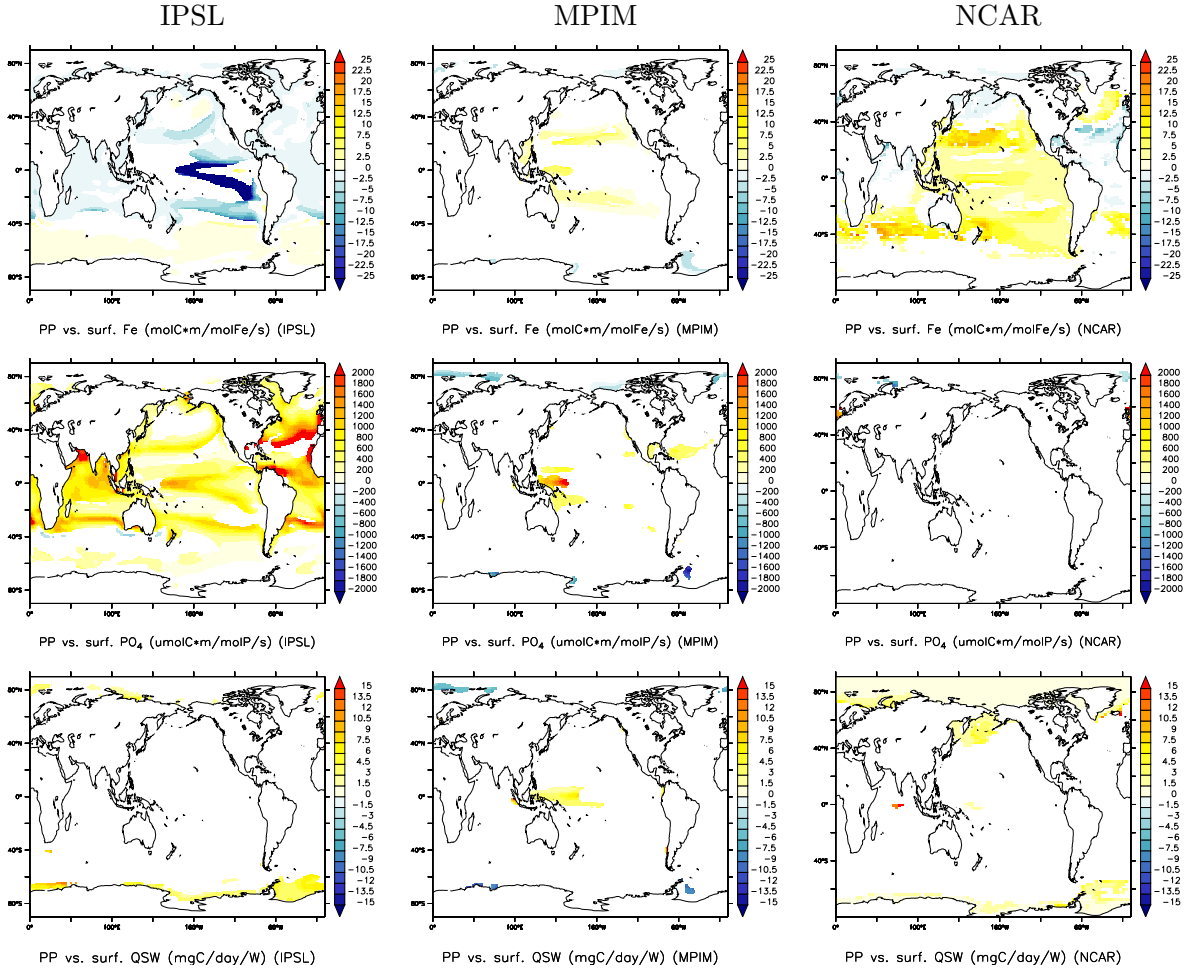

Figure 4.10: Linear correlation between vertically integrated annual mean PP and iron (Fe, top row), phosphate (PO_4, middle row), and surface solar irradiance (QSW, bottom row) as simulated by the IPSL (left column), MPIM (middle column), and NCAR (right column) models. The regression has been calculated for each grid cell using the time series from 1860 to 2100. For Fe and PO_4, average concentrations over the top 75 m have been used. The figures show the regression slopes (ΔPP ($\frac{\text{molC}}{\text{m}^2\ \text{s}}$) per Δ[Fe] ($\frac{\text{molFe}}{\text{m}^3}$); ΔPP ($\frac{\mu\text{molC}}{\text{m}^2\ \text{s}}$) per $\Delta[PO_4]$ ($\frac{\text{molP}}{\text{m}^3}$); ΔPP ($\frac{\text{mgC}}{\text{m}^2\ \text{day}}$) per ΔQSW ($\frac{\text{W}}{\text{m}^2}$)), where $R^2 > 0.5$.

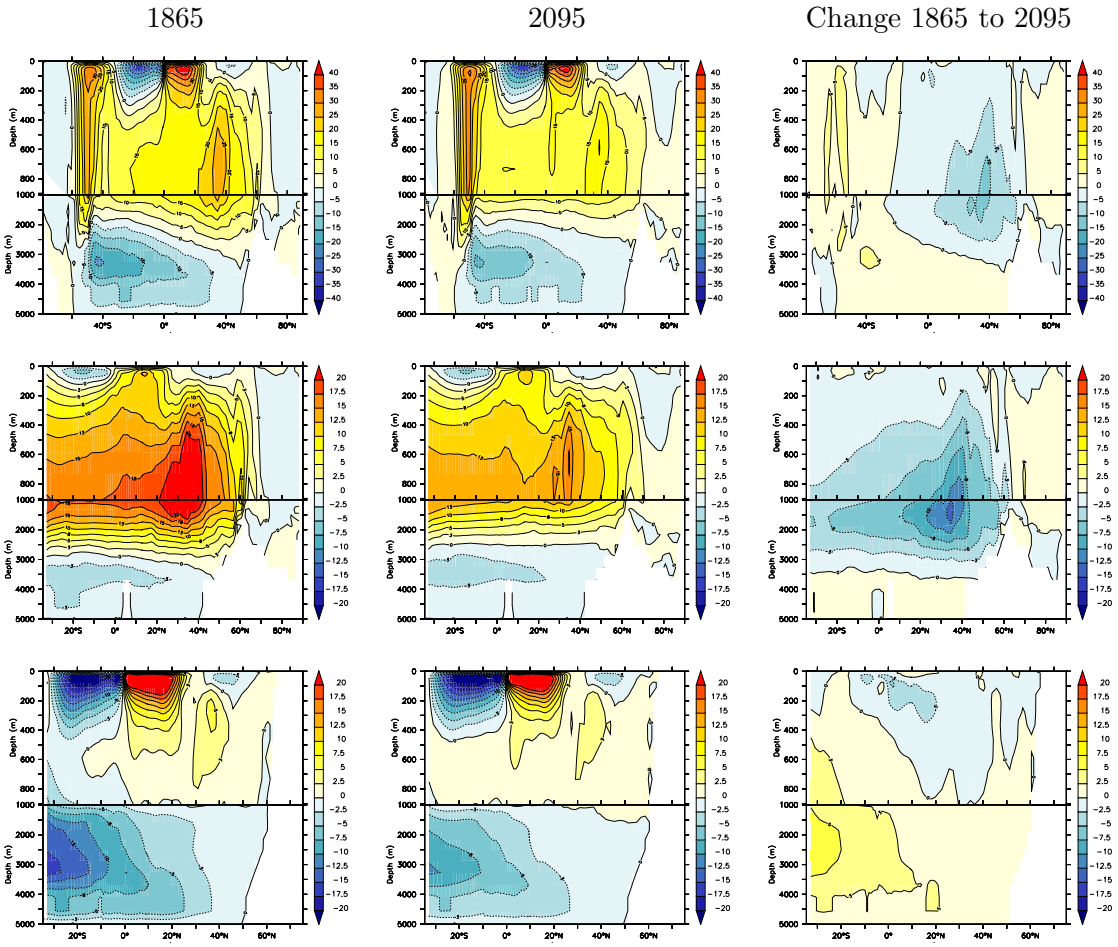

Figure 4.11: Simulated changes in the meridional overturning circulation (MOC) in the global ocean (top), in the Atlantic and Arctic (middle), and in the Pacific and Indian Ocean (bottom). In the left and middle columns the average MOC stream-function over the decades 1860-1869 (1865) and 2090-2099 (2095), respectively, is shown. The right column shows the difference 2095 minus 1865. All figures show values in Sverdrup [Sv] simulated by the NCAR model.

in surface PO_4 and NO_3 concentrations and increased stratification. At high latitudes, PP tends to increase in the Arctic (NCAR and MPIM), in the North Pacific (NCAR and a smaller region in IPSL), and in several regions in the Southern Ocean (all models), eventually due to less temperature and light limitation.

The results also show, that there are relatively large differences between the models and that the underlying mechanisms are rather complex and diverse. Therefore, estimating which factors determine the projected PP changes and to what extent, is a difficult task that has only been possible to a certain degree within the boundaries of this thesis.
In a further analysis of the simulation results, long-term changes could be compared to seasonal and interannual variability and changes in seasonal and interannual variability themselves could be analyzed. Furthermore, a more detailed analysis of changes in the ocean circulation could be done and more advanced statistical methods could be applied. Interesting topics would also be the export of $CaCO_3$, which is quite different in the IPSL and MPIM models, and its relation to the export of organic matter, as well as the relation be-

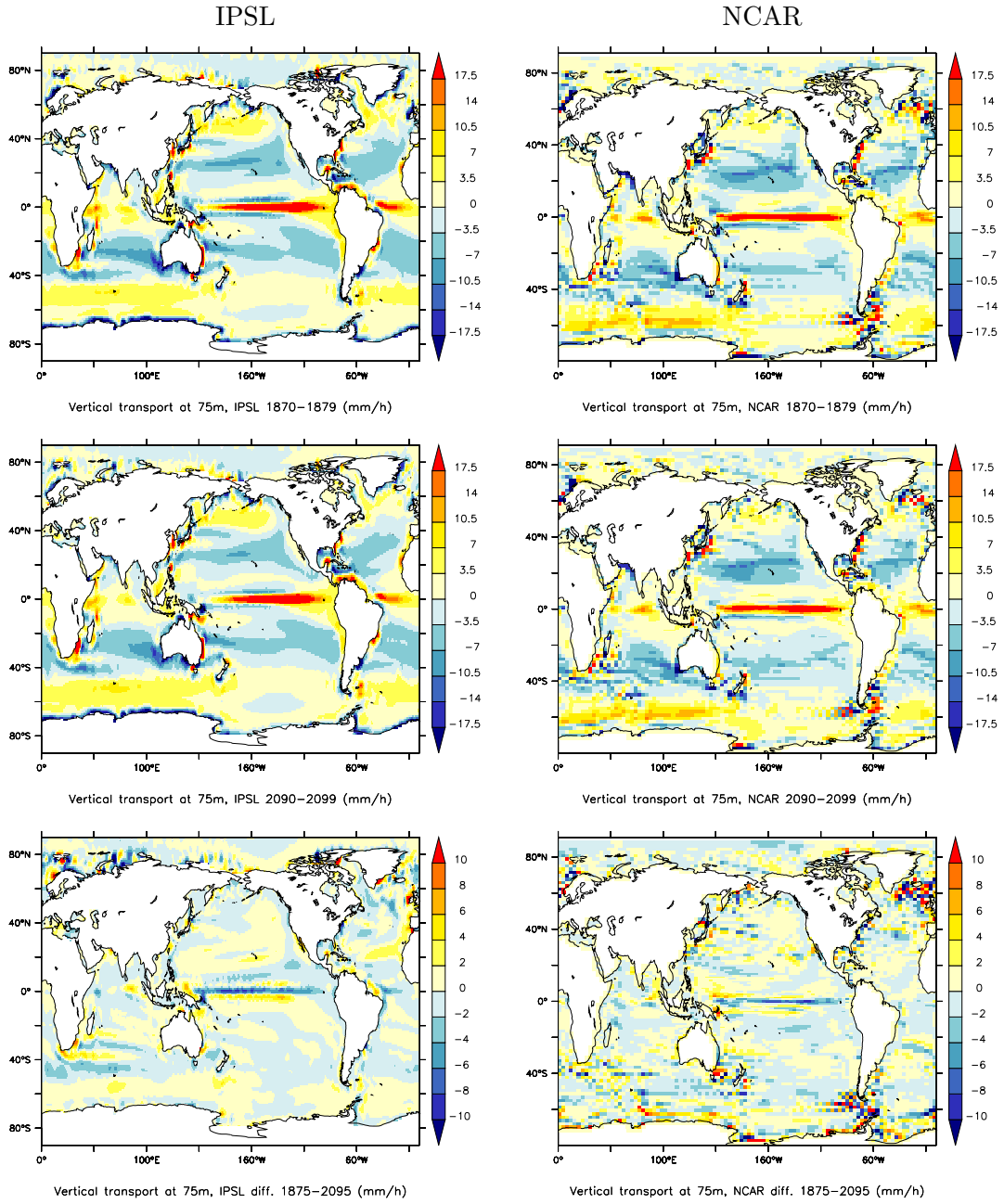

Figure 4.12: Vertical transport at a depth of 75 m as simulated by the IPSL (left column) and NCAR (right column) models. The top and middle rows show the averages over the decade 1870-1879 (1875) and 2090-2099 (2095), respectively. The bottom row shows the difference 2095 minus 1875. The vertical transport is indicated as sum of the eulerian velocity vertical component and the eddy induced transport velocity vertical component in meters per second.

tween primary production and export of particulate and dissolved organic matter. Finally, the results could be interpreted regarding more the internal implementation of the models and a comparison with other studies could be done.

Appendix A

Technical aspects of running the CSM1.4-carbon model

During my thesis work, I spent some time on setting up, debugging and running the NCAR CSM-1.4-carbon model. This included solving some issues that prevented the model from running properly on the local Linux PC cluster at our division, as well as porting the model code from the IBM SP4 (running AIX) platform to the new IBM p5 system (running Linux) at the Swiss National Supercomputing Centre[1] (CSCS) in Manno.
This appendix contains some technical information regarding this tasks. It is not intended to be a complete and definite manual, but it contains some important findings, which solved several problems.

A.1 Running the model on the IBM p5 system at CSCS

This sections provides an overview of the most important configuration settings and other information on running the CSM1.4-carbon code on the IBM p5 system[2] at the CSCS.

A.1.1 Running in 64bit mode

- Use 64-bit thread-safe libraries (see below)
- Set the `OBJECT_MODE` environment variable in the start script:
  `setenv OBJECT_MODE 64`

A.1.2 Libraries

- NetCDF
  - Include path: `/apps/netcdf-3.6.1/64/include`
  - Library path: `/apps/netcdf-3.6.1/64/lib`
  - Library switches: `-lnetcdf`
- IBM POE (including MPI and LAPI)

[1] http://www.cscs.ch/
[2] https://www-users.cscs.ch/resources/ibm/p5/docs.html (requires a login account at CSCS)

  - Include path: `/opt/ibmhpc/ppe.poe/include/thread64`
  - Library path: `-`
  - Library switches: `-lmpi_ibm -lpoe -llapi`

- IBM MASS (Mathematical Acceleration Subsystem)
  - Include path: `-`
  - Library path: `/opt/ibmcmp/xlmass/4.3`
  - Library switches: `-lmass_64 -lmassvp5_64`

- MSS utilities (included in CSM-1.4, no system library)
  - The library has to be compiled in `/ccsm/bio/lib/mss_utils64` using the script `compile.sh`. Edit the script to use the same compiler and compiler-options as the model components, and set the `OBJECT_MODE` environment variable to 64 in order to generate 64-bit code.
  - Include path: `-`
  - Library path: `$(HOME)/ccsm/bio/lib/mss_utils64`
  - Library switches: `-lmms`

A.1.3 Compilers and compiler options

- Preprocessor (`CPP`): `/opt/ibmcmp/xlf/10.1/exe/cpp -P`
  - Preprocessor macros (`CPPFLAGS`):
    * `-DLinux -DLINUX` - Enable Linux specific code (case sensitive; BOTH macros must be specified!)
    * `-DIBM_XLF` - Enable IBM XL Fortran Compiler specific code (newly introduced, see below)
    * `-DCOUP_CSM` - Run fully coupled model (MPI)
    * `-DMSS` - Enable MSS utils code
    * `-DTASKCOMMON='common'` - (Name for common data blocks)
    * `-DSPMD` - Enable code for running the atmosphere component in hybrid mode (multiple MPI-processes). Don't specify this macro, if only one atmosphere process (with SMP parallelization) is used!
  - Additional macros for the ocean component are included at compile time by adding `$(shell cat options.list)` to `CPPFLAGS`.
  - Additional macro for the atm component: `-DFORTFFT` - Use slow Fortran FFT routines instead of ECMTTF library.
    Additionally `$(SRCDIR)/mathutil` and `$(SRCDIR)/srchutil` must be in the include path.

- Fortran compiler (`FC`): `mpfort -compiler xlf90_r` (IBM XL Fortran with MPI and SMP support, thread-safe)
  - Compiler options (`FFLAGS` and `FOPT_LEVEL`):

    - `-qarch=pwr5 -qtune=pwr5` - Generate code for Power5 platform
    - `-qsmp=noauto -qthreaded` - Generate SMP code (OpenMP), no automatic parallelization
    - `-qrealsize=8` - Size of type real
    - `-qstrict` - Absolute floating point precision (IEEE semantics). Relevant when using -O3 optimization.
    - `-qextname=t_initializef:t_startf:t_stopf:t_prf` - Fixes missing underscore for this functions?
    - `-O2` - Optimization level 2. **IMPORTANT:** Do not use a higher optimization level! Using level 3 will produce different results than level 2 and it is very likely that the model (atmosphere) will crash sometimes with a 'segmentation fault' error. Level 2 produces the same results as when no optimization is used, but was not found to enhance performance, though.
  - Additional options for fixed-format code (*.F files, `FIXEDFLAGS`): `-qsuffix=f=f -qfixed=132`
  - Additional options for free-format code (*.F90 files, `FREEFLAGS`): `-qsuffix=f=f90 -qfree=f90`
  - Additional options for the ocean and land module: `-byteswapio`
  - Debugging options (not enabled in normal operation): `-g -qfullpath -qattr=full -qlist -qlistopt -qsource`

- C compiler (`CC`): `cc` (IBM XL C compiler)
  - Compiler options (`CFLAGS`):
    - `-qsmp=noauto -qthreaded` - Generate SMP code (OpenMP), no automatic parallelization

- Linker options (`LD_FLAGS`):
  - `-qsmp=noauto -qthreaded` - Generate SMP code (OpenMP), no automatic parallelization

A.1.4 Parallelization

- The model components (cpl,atm,ocn,ice,lnd) run as individual processes (MPI tasks) and communicate with MPI.
- The model components atm,ocn,lnd and cpl can be shared-memory parallelized on SMP nodes (OpenMP). These processes then run multithreaded on multiple CPUs (one MPI-task with multiple threads).
- The atm and lnd component can be parallelized additionally by enabling `-DSPMD`. In this case the atm component runs with multiple MPI-tasks (processes), which again can run multithreaded.
- The number of MPI-tasks (processes) is defined in the start script by the variable `NTASKS`. It must be 1 for all components, except for atm and lnd when `-DSPMD` is being used.

- The number of threads per MPI-task is defined in the start script by the variable `NCPUS`. The OpenMP variable `OMP_NUM_THREADS` will be set to this values for each component at start-up.
- The OpenMP variable `OMP_DYNAMIC` must NOT be set to `true` in order to gain the desired performance.
- The IBM XL SMP variable `XLSMPOPTS` must be set to `"stack=256000000"` and `MP_CSS_INTERRUPT` must NOT be set to `yes`. Otherwise, the atm component crashes with 'Segmentation fault' at start-up. Additionally the stack_limit load-leveler variable has been set to `# @ stack_limit = 2200mb`, as well as the environment variable `MP_THREAD_STACKSIZE=200M`. These values, however, are possibly larger than required. (Note: This information has to be verified, because these problems might have been connected to the 'optimization level 3 problem' described above and might be solved using a lower optimization level.)
- The distribution of the MPI-tasks to multiple nodes can be specified by the `task_geometry` load-leveler variable. The format is `task_geometry = {(a,b,c)(d,e)}`, where the parentheses embrace task ids that run on the same node. Here the tasks a, b and c run on the first node, d and e on the second node. If only one atm task is used (total 5 tasks), task 0 is atm, task 1 lnd, task 2 ice, task 3 ocn, and task 4 cpl. If more than one atm is used the task ids of the other components increment accordingly.
- To get the optimal performance the following parameters have to be fine-tuned:
  - The number of atm and lnd tasks (`NTASKS` / `-DSMPD`)
  - The number of atm, ocn, lnd and cpl SMP-threads per task (`NCPUS`)
  - The distribution of the MPI-tasks onto multiple nodes (`task_geometry`)
  - The network adapter (`network.MPI`)
  - Possibly the OpenMP scheduling variable (`OMP_SCHEDULE`) or other things

A.1.5 Code modifications

In order to get the model running, the following changes have been made to the code:

1. `src.atm/chemmix.F`: The comment starting at line 75 has been modified, because the $-signs confused the compiler.
2. `src.atm/select.F90`: The function `select()` (which is part of the atmosphere mathutil code, but never used...) has been removed, because it caused a conflict with the system call `select()`! (This was done by replacing the original subroutine with the empty `select_dummy()`.)
3. `src.shr/mpi_setup.F`: `call chdir()` has been changed to `call shr_sys_chdir()` at line 110, in order to use the proper wrapper function when changing the directory.
4. `src.atm/ioFileMod.F90` and `src.shr/shr_sys_mod.F90`: Some `#ifdef AIX` preprocessor directives have been changed to the newly introduced `#ifdef IBM_XLF`, because the corresponding code is rather compiler-specific than AIX architecture-specific.

Additionally, some modifications have been made in `src/atm/spmdinit.F90` and `src.shr/shr_msg_mod.F90` in order to fix some minor issues.

A.1.6 Current status and performance

- The model runs well with pure shared-memory message passing, on one node with up to 16 CPUs. Best performance (5.7 min/mt) was achieved with one task per component (SPMD disabled) and the following distribution of the CPUs among the tasks for SMP-threads: cpl(1), atm(7), ocn(5), ice(1), lnd(2)

- On two nodes with a total of 32 CPUs, best performance (3.3 min/mt) was achieved again without SPMD and by using the network adapter `# @ network.MPI = sn_all, shared,US,HIGH`, as well as the following node/task/thread distribution: first node: atm(16); second node: cpl(1), ocn(10), ice(1), lnd(4) (`task_geometry = {(0) (1,2,3,4)}`).

- Using more than two nodes did not improve the performance significantly (figure A.1).

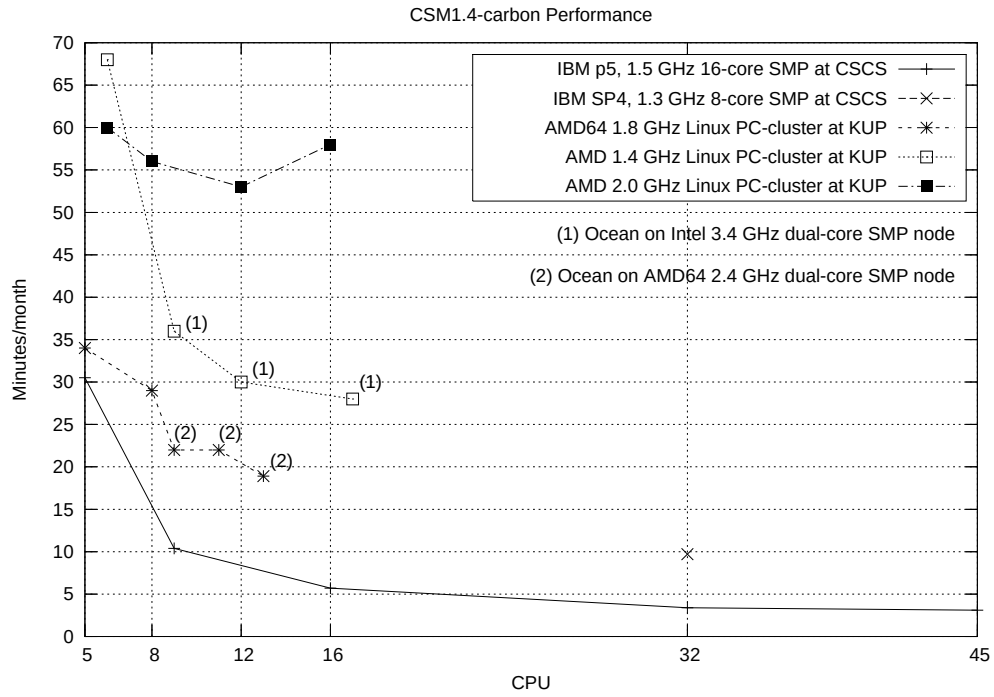

Figure A.1: Performance and scalability of the CSM1.4-carbon model on different platforms. The performance is indicated by the amount of time it takes to simulate one month.

A.1.7 Additional notes

- For FFT, slow Fortran routines (-DFORTFFT macro) are used because the ECMFFT library is not available.

- While debugging and running the model, the start script and the makefile have been improved and cleaned up. Additionally some tools have been developed (e.g. new backup procedure, performance calculator, script to automatically set up the model for a restart).

A.2 Running the model on the local Linux PC cluster

The setup of the CSM1.4-model on the local PC cluster is similar to the setup on the IBM p5 system (section A.1), because both systems use the Linux operating system. However there are some differences, most notably another compiler (PGI) is used.

In order to run the model on the Linux cluster, some code modification was needed. Added or modified files are: `src.atm/data.h` and `src.atm/data.F.90` (declaration of ff-emission variables), `src.atm/spmdinit.F90` (fixed if/endif issue), `src.lnd/casactli.F` (removed redundant 'implicit none'), and `src.atm/scan2.F90` (fixed typo). Fortran formatting issues have been fixed in `src.lnd/lsm_csmrcv.F, src.lnd/lsm_spmd.F, hist_inihst.F, hist_timvar.F, lsm_csmsnd.F,` and `restwrt.F`.
Additionally, the makefile and start script have been improved and a new header file `src.shr/case_definition.h` has been introduced, in order to simplify the setup of new cases. The following instructions may help to set up a new case:

1. Edit the start script `C4t.001.nqs0`:
   - `CASE` : Case name (max. 16 characters).
   - `NCPUS` : Only relevant for the ocean module. Set it to the number number of CPUs, if the ocean runs with OpenMP on a SMP node, otherwise set it to 1.
   - `CSMROOT` : Root directory of model code.
   - `EXEDIR` : Output directory for executables, log files etc.
   - `CP_DIR` : Data output directory.
   - `TMPDIR` : Temporary directory for compiling.
   - `MPIRUN` : Path to the mpirun script.
   - `INC_MPI` : Path to the MPI include files.
   - `LIB_MPI` : Path to the MPI libraries.
2. Edit `Makefile`:
   - Add `-DSPMD` to `CPPFLAGS` if multiple atmosphere processes should be used, otherwise remove it.
   - Add `-mp` to `FFLAGS` and `LD_FLAGS` of the ocean module, if the ocean runs with OpenMP on a SMP node, otherwise remove it.
   - `INC_NETCDF` : Path to the Netcdf include files.
   - `LIB_NETCDF` : Path to the Netcdf libraries.
   - `INC_MPI` : Path to the MPI include files.
   - `LIB_MPI` : Path to the MPI libraries.
3. Edit `src.ocn/setdefs.csh`: Set `OpenMP = yes`, if the ocean component should run with OpenMP on a SMP node, otherwise set it to 'no'.
4. Edit `pgfile`: Set node names and the paths to executables (EXEDIR).
5. Edit `src.shr/case_definition.h`:

- `CASE_NAME` : Like `CASE` in the start script.
- `CASE_CP_DIR` : Like `CP_DIR` in the start script.
- `CASE_DATE` : Date for log files.
- Adjust the user name.

6. Compile `mss_utils`: Run `compile.sh` in `src.shr/mms_utils/`.

7. Compile and run the model: Run the start script `C4t.001.nqs0`.

Because the ocean component (NCOM) can only be parallelized using shared-memory (OpenMP) parallelization, the scalability on single CPU systems is very limited. To improve performance the ocean component was also deployed on a cluster node with a dual-core CPU, which improved the performance significantly (figure A.1). A major performance improvement has also be found when running the model in 64bit mode on AMD64 systems.
When using OpenMP with the ocean component, it is very important **NOT** to use the `-Mconcur` PGI compiler flag, because this will produce different results and will likely crash the model.

A.3 Differences between model results on different platforms

Results from models that run on different platforms (i.e. the combination of CPU, compiler, libraries etc. on a specific machine) are not identical but differ slightly, although the model code and setup are identical. A small comparison of the results from the control run on four different platforms (IBM SP4 and IBM p5 systems at CSCS, as well as two local Linux PC clusters (AMD 32bit and AMD 64bit)) shows that these differences are strongly region and tracer dependent. All differences between two of the four platforms are very similar, that means for example that the difference between the two IBM systems is not smaller or larger as the difference between one IBM system and the Linux PC clusters.

The differences in surface DIC (first 100 years of the control run) is virtually zero in the global average. However, the standard deviation of the difference distribution among all surface grid boxes is about 0.02 mol/m^3 ($\approx$ 1% of the in situ value) and the maximum is around 0.2 mol/m^3 ($\approx$ 10%). This means that there are regions where the differences between different platforms are more pronounced than in the global average. The standard deviation and the maximum of the difference increse very rapidly during the first year and then remain relatively constant on the levels mentioned above, which means that there is no trend with time. The simulated surface DIC shows virtually no difference in spatial variability between the four platforms.
Atmospheric CO_2 at the ocean surface looks similar. The average difference is around $\pm$2 ppm ($\approx$ 1% of the in situ value) and maximum deviations are around 6 ppm ($\approx$ 5%). Again, no trend is visible in the first 100 years and the standard deviation and the maximum difference are relatively constant.
The comparison of simulated oxygen between results from the IBM SP4 and from the two Linux PC clusters show, that the differences are particularly large (around 5%) where the model shows the largest drift. For O_2 that is in the North Atlantic between 40°N and 60°N above 1000 m depth and in the Southern Ocean south of 60°S above 1500 m.

In the case of surface DIC and atmospheric CO_2 the differences between results from different platforms are small compared to the changes in the real simulations with increasing CO_2. However, the differences have to be considered and, in principle, the impacts should be assessed for every variable. The deviations due to different computing platforms can be an indicator of the model's stability and a measure of errors in the simulation results.

Bibliography

C. M. Ammann, G. A. Meehl, W. M. Washington, and C. S. Zehnder. A monthly and latitudinally varying volcanic forcing dataset in simulations of 20th century climate. *Geophysical Research Letters*, 30, 2003.

C. M. Ammann, F. Joos, D. S. Schimel, B. L. Otto-Bliesner, and R. A. Tomas. Solar influence on climate during the past millennium: Results from transient simulations with the NCAR Climate System Model. *PNAS*, 104(10):3713–3718, 2007. doi: 10.1073/pnas.0605064.

O. Aumont and L. Bopp. Globalizing results from ocean in situ iron fertilization studies. *Global Biogeochemical Cycles*, 20:GB2017, 2006.

O. Aumont, E. Maier-Reimer, S. Blain, and P. Monfray. An ecosystem model of the global ocean including Fe, Si, P colimitations. *Global Biogeochemical Cycles*, 17(2):1060, 2003.

M. J. Behrenfeld, R. T. O'Malley, D. A. Siegel, C. R. McClain, J. L. Sarmiento, G. C. Feldman, A. J. Milligan, P. G. Falkowski, R. M. Letelier, and E. S. Boss. Climate-driven trends in contemporary ocean productivity. *Nature*, 444(7120):752–755, December 2006.

M. Blackmon, B. Boville, F. Bryan, R. Dickinson, P. Gent, K. Kiehl, R. Moritz, D. Randall, J. Shukla, S. Solomon, G. Bonan, S. Doney, I. Fung, J. Hack, E. Hunke, J. Hurrel, J. Kutzback, J. Meehl, B. Otto-Bliesner, R. Saravanan, E. K. Schneider, L. Sloan, M. Spall, K. Taylor, J. Tribbia, and W. Washington. The community climate system model. *Bulletin of the American Meteorological Society*, 82:2357–2376, 2001.

G. B. Bonan. The NCAR land surface model (LSM version 1.0) coupled to the ncar community climate model. *NCAR Tech. Note NCAR/TN-429+STR*, page 171pp, 1996.

B. A. Boville and P. R. Gent. The NCAR climate system model, version one. *Journal of Climate*, 11:1115–1130, 1998.

W. S. Broecker, T. Langdon, T. Takahashi, and T.-S. Peng. Factors controlling the rate of $CaCO_3$ precipitation on Grand Bahama Bank. *Global Biogeochemical Cycles*, 15:589–596, 2001.

K. Caldeira and M. E. Wickett. Ocean model predictions of chemistry changes from carbon dioxide emissions to the atmosphere and ocean. *Journal of Geophysical Research*, 110: C09S04, 2005.

L. Cao, K. Caldeira, and A. K. Jain. Effects of carbon dioxide and climate change on ocean acidification and carbonate mineral saturation. *Geophysical Research Letters*, 34:L05607, 2007.

S. Chung, G. Park, K. Lee, R. M. Key, F. J. Millero, R. A. Feely, C. L. Sabine, and P. G. Falkowski. Postindustrial enhancement of aragonite undersaturation in the upper tropical and subtropical atlantic ocean: The role of fossil fuel CO_2. *Limnology and Oceanography*, 49(2):315–321, March 2004.

M. E. Conkright, J. I. Antonov, T. P. Boyer, R. A. Locarnini, T. D. O'Brien, C. Stephens, and H. E. Garcia. *World Ocean Atlas 2001*, volume 49-52 of *NOAA Atlas NEDIS*. U.S. Govt. Printing Office, Washington, D. C., 2002.

A. Dickson. *Handbook of methods of the analysis of the various parameters of the carbon dioxide system in seawater*. U.S. Dep. of Energy, Washington, D. C., 2002.

S. Doney, K. Lindsay, I. Fung, and J. John. Natural variability in a stable, 1000 year global coupled climate-carbon cycle simulation. *Journal of Climate*, 19(13):3033–3054, July 2006.

P. Friedlingstein, P. Cox, R. Betts, L. Bopp, W. Von Bloh, V. Brovkin, P. Cadule, S. Doney, M. Eby, I. Fung, G. Bala, J. John, C. Jones, F. Joos, T. Kato, M. Kawamiya, W. Knorr, K. Lindsay, H. D. Matthews, T. Raddatz, P. Rayner, C. Reick, E. Roeckner, K. G. Schnitzler, R. Schnur, K. Strassmann, A. J. Weaver, C. Yoshikawa, and N. Zeng. Climate-Carbon Cycle Feedback Analysis: Results from the C^4MIP model intercomparison: Evolution of carbon sinks in a changing climate. *Journal of Climate*, 19:3337–3353, 2006.

I. Fung, S. Doney, K. Lindsay, and J. John. Evolution of carbon sinks in a changing climate. *Proceedings of the national academy of sciences of the USA*, 102(32):11201–11206, August 2005.

R. Gangstø, M. Gehlen, L. Bopp, O. Aumont, B. Schneider, and F. Joos. Representing aragonite production and dissolution in a biogeochemical ocean model. *Global Biogeochemical Cycles*, submitted, 2007.

J.-P. Gattuso, M. Frankignoulle, I. Bourge, S. Romaine, and R. W. Buddemeier. Effect of calcium carbonate saturation of seawater on coral calcification. *Global and Planetary Change*, 18:37–46, 1998.

J.-P. Gattuso, D. Allemand, and Frankignoulle. Photosynthesis and calcification at cellular, organismal and community levels in coral reefs: A review on interactions and control by carbonate chemistry. *American Zoology*, 39:160–183, 1999.

M. Gehlen, L. Bopp, N. Ernprin, O. Aumont, C. Heinze, and O. Raguencau. Reconciling surface ocean productivity, export fluxes and sediment composition in a global biogeochemical ocean model. *Biogeosciences*, 3:521–537, 2006.

P. R. Gent, F. O. Bryan, G. Danabasoglu, S. C. Doney, W. R. Holland, W. G. Large, and J. C. McWilliams. The NCAR Climate System Model global ocean component. *Journal of Climate*, 11:1287–1306, 1998.

N. Gruber, J. L. Sarmiento, and T. F. Stocker. An improved method for detecting anthropogenic CO_2 in the oceans. *Global Biogeochemical Cycles*, 10:809–837, 1996.

O. Hoegh-Guldberg. Low coral cover in a high-CO_2 world. *Journal of Geophysical Research*, 110:C09S06, 2005.

F. Hourdin, I. Musat, S. Bony, P. Braconnot, F. Codron, J.-L. Dufresne, L. Fairhead, M.-A. Filiberti, P. Friedlingstein, J.-Y. Grandpeix, G. Krinner, P. Levan, Z.-X. Li, and F. Lott. The LMDZ4 general circulation model: climate performance and sensitivity to parametrized physics with emphasis on tropical convection. *Climate Dynamics*, 19:3445–3482, 2006.

S. E. Ingle. Solubility of calcite in the ocean. *Marine Chemisty*, 3:301–319, 1975.

W. P. Inskeep and P. R. Bloom. An evaluation of rate equations for calcite percipitation kinetics at pCO_2 less than 0.01 atm and pH greater than 8. *Geochimica et Cosmochimica Acta*, 49:2165–2180, 1985.

Intergovernmental Panel on Climate Change IPCC. *Special Report on Emission Scenarios, Working Group III*, volume 11. Cambridge University Press, New York, 2000.

Intergovernmental Panel on Climate Change IPCC. *Climate Change 2007: The Physical Science Basis, Summary for Policymakers*. 2007.

A. Ishimatsu, M. Hayashi, K.-S. Lee, T. Kikkawa, and J. Kita. Physiological effects on fishes in a high-CO_2 world. *Journal of Geophysical Research*, 110:C09S09, 2005. doi: 10.1029/2004JC002564.

F. Joos, I. C. Prentice, S. Sitch, R. Meyer, G. Hooss, G.-K. Plattner, S. Gerber, and K. Hasselmann. Global warming feedbacks on terrestrial carbon uptake under the Intergovernmental Panel on Climate Change (IPCC) emission scenarios. *Global Biogeochemical Cycles*, 15(4): 891–907, 2001.

S. Jutterström and L. G. Anderson. The saturation of calcite and aragonite in the arctic ocean. *Marine Chemistry*, 94:101–110, 2005.

C. D. Keeling and T. P. Whorf. Atmospheric CO_2 records from sites in the SIO air sampling network. *In Trends: A Compendium of Data on Global Change. Carbon Dioxide Information Analysis Center, Oak Ridge National Laboratory, U.S. Department of Energy, Oak Ridge, Tenn., U.S.A.*, 2005.

R. M. Key, A. Kozyr, C. L. Sabine, K. Lee, R. Wanninkhof, J. Bullister, R. A. Feely, F. Millero, C. Mordy, and T.-H. Peng. A global ocean carbon climatology: Results from Global Data Analysis Project (GLODAP). *Global Biogeochemical Cycles*, 18:GB4031+, 2004. doi: 10.1029/2004GB002247.

J. T. Kiehl, J. J. Hack, G. B. Bonan, B. A. Boville, D. L. Williamson, and P. J. Rasch. The National Center for Atmospheric Research Community Climate Model. *Journal of Climate*, 11:1151–1178, 1998.

J. A. Kleypas, R. W. Buddemeier, D. Archer, J.-P. Gattuso, C. Langdon, and B. N. Opdyke. Geochemical consequences of increased atmospheric carbon dioxide on coral reefs. *Science*, 284:118–120, Apr 1999.

J. A. Kleypas, R. W. Buddemeier, C. M. Eakin, J.-P. Gattuso, J. Guinotte, O. Hoegh-Guldberg, R. Iglesias-Prieto, P. L. Jokiel, C. Langdon, W. Skirving, and A. E. Strong. Comment on "coral reef calcification and climate change: the effect of ocean warming". *Geophysical Research Letters*, 32:L08601, 2005.

J. A. Kleypas, R. A. Feely, V. J. Fabry, C. Langdon, C. L. Sabine, and L. L. Robbins. Impacts of ocean acidification on coral reefs and other marine calcifiers: A guide for future research, report of a workshop held 18-20 april 2005, St. Petersburg, FL, sponsored by NSF, NOAA, and the U.S. Geological Survey. 2006.

G. Krinner, N. Viovy, N. de Noblet-Ducoudre, J. Ogee, J. Polcher, P. Friedlingstein, P. Ciais, S. Sitch, and I. C. Prentice. A dynamic global vegetation model for studies of the coupled atmosphere-biosphere system. *Global Biogeochemical Cycles*, 19:GB1015, 2005.

C. Langdon and M. J. Atkinson. Effect of elevated pCO_2 on photosynthesis and calcification of corals and interactions with seasonal change in temperature/irradiance and nutrient enrichment. *Journal of Geophysical Research*, 110:C09S07, 2005.

C. Langdon, T. Takahashi, C. Sweeney, D. Chipman, J. Goddard, F. Marubini, H. Aceves, H. Barnett, and M. J. Atkinson. Effect of calcium carbonate saturation state on the calcification rate of an experimental coral reef. *Global Biogeochemical Cycles*, 14(2):639–654, June 2000.

C. Le Quéré, O. Aumont, L. Bopp, P. Bousquet, P. Ciais, R. Francey, M. Heimann, C. D. Keeling, R. F. Keeling, H. Kheshgi, P. Peylin, S. C. Piper, I. C. Prentice, and P. J. Rayner. Two decades of ocean CO_2 sink and variability. *Tellus, Series B*, 55(2):649–656, Apr 2003.

N. Leclercq, J.-P. Gattuso, and J. Jaubert. CO_2 partial pressure controls the calcification rate of a coral community. *Global Change Biology*, 6:329–334, 2000.

J. M. Lough and D. J. Barnes. Environmental controls on growth of the massive coral porites. *Journal of Experimental Marine Biology and Ecology*, 245:225–243, 2000.

T. J. Lueker, A. G. Dickson, and Keeling C. D. Ocean pCO_2 calculated from dissolved inorganic carbon, alkalinity, and equations for K-1 and K-2: validation based on laboratory measurements of CO_2 in gas and seawater at equilibrium. *Marine Chemistry*, 70(1-3): 105–119, May 2000.

G. Madec, P. Delecluse, M. Imbard, and C. Levy. OPA 8.1 ocean general circulation model reference manual. *Notes du Pôle de Modélisation 11, Tech. rep., Institut Pierre Simon Laplace des Sciences de l'Environment Global, Paris*, pages 1–91, 1998.

E. Maier-Reimer. Geochemical cycles in an ocean general circultion model. Preindustrial tracer distributions. *Global Biogeochemical Cycles*, 7:645–677, 1993.

E. Maier-Reimer, I. Kriest, J. Segschneider, and P. Wetzel. The HAMburg Ocean Carbon Cycle model HAMOCC5.1 - Technical description. *Berichte zur Erdsystemforschung 14/2005, Max Planck-Institut für Meteorologie, Hamburg, Germany*, 2005.

A. C. Manning and R. F. Keeling. Global oceanic and land biotic carbon sinks from the Scripps atmospheric oxygen flask sampling network. *Tellus, Series B*, 58(2):95–116, April 2006.

S. J. Marsland, H. Haak, J. H. Jungclaus, M. Latif, and F. Roske. The Max-Planck-Institute global ocean/sea ice model with orthogonal curvilinear coordinates. *Ocean Modelling*, 5: 91–127, 2003.

F. Marubini, H. Barnett, C. Langdon, and M. J. Atkinson. Dependence of calcification on light and carbonate ion concentration for the hermatypic coral Porites compressa. *Marine Ecology-Progress Series*, 220:153–162, 2001.

F. Marubini, C. Ferrier-Pages, and J. P. Cuif. Suppression of skeletal growth in scleractinian corals by decreasing ambient carbonate-ion concentration: a cross-family comparison. *Proceedings of the Royal Society of London Series B*, 270:179–184, January 2003.

R. J. Matear and A. C. Hirst. Climate change feedback on the future oceanic CO_2 uptake. *Tellus, Series B*, 51:722–733, 1999.

B. I. McNeil, R. J. Matear, and D. J. Barnes. Coral reef calcification and climate change: The effect of ocean warming. *Geophysical Research Letters*, 31:L22309, 2004.

F. J. Millero. The thermodynamics of the carbonic acid system in seawater. *Geochimica et Cosmochimica Acta*, 43:1651–1661, 1979.

F. J. Millero. Thermodynamics of the carbon dioxide system in the oceans. *Geochimica et Cosmochimica Acta*, 59(4):661–677, 1995.

A. Mucci. The solubility of calcite and aragonite in seawater at various salinities, temperatures and 1 atmosphere total pressure. *American Journal of Science*, 238:780–799, 1983.

R. G. Najjar, J. L. Sarmiento, and J. R. Toggweiler. Downward transport and fate of organic matter in the ocean: simulations with a general circulation model. *Global Biogeochemical Cycles*, 6(1):45–76, 1992.

J. C. Orr, V. J. Fabry, O. Aumont, L. Bopp, S. C. Doney, R. A. Feely, A. Gnanadesikan, N. Gruber, A. Ishida, F. Joos, R. M. Key, K. Lindsay, E. Maier-Reimer, R. Matear, P. Monfray, A. Mouchet, R. G. Najjar, G.-K. Plattner, K. B. Rodgers, C. L. Sabine, J. L. Sarmiento, R. Schlitzer, R. D. Slater, I. J. Totterdell, M. F. Weirig, Y. Yamanaka, and A. Yool. Anthropogenic ocean acidification over the twenty-first century and its impact on calcifying organisms. *Nature*, 437:681–686, September 2005.

G.-K. Plattner, F. Joos, and T. F. Stocker. Revision of the global carbon budget due to changing air-sea oxygen fluxes. *Global Biogeochemical Cycles*, 16(4):1096, 2002.

J. T. Randerson, M. V. Thompson, T. J. Conway, I. Y. Fung, and C. B. Field. The contribution of terrestrial sources and sinks to trends in the seasonal cycle of atmospheric carbon dioxide. *Global Biogeochemical Cycles*, 11(4):535–560, 1997.

S. Reynaud, N. Leclercq, S. Romaine-Lioud, C. Ferrier-Pags, J. Jaubert, and J.-P. Gattuso. Interacting effects of CO_2 partial pressure and temperature on photosynthesis and calcification in a scleractinian coral. *Global Change Biology*, 9:1660–1668, 2003.

E. Roeckner, R. Brokopf, M. Esch, M. Giorgetta, S. Hagemann, L. Kornblueh, E. Manzini, U. Schlese, and U. Schulzweida. Sensitivity of simulated climate to horizontal and vertical resolution in the ECHAM5 atmosphere model. *Journal of Climate*, 19:3771–3791, 2006.

J. L. Sarmiento and N. Gruber. *Ocean Biogeochemical Dynamics*. Princeton University Press, 2004.

B. Schneider, L. Bopp, M. Gehlen, J. Segschneider, T. L. Frölicher, F. Joos, P. Cadule, P. Friedlingstein, S. C. Doney, and M. J. Behrenfeld. Spatio-temporal variability of marine primary and export production in three global coupled climate carbon cycle models. *Biogeosciences Discussions*, 4(3):1877–1921, June 2007.

K. Schneider and J. Erez. The effect of carbonate chemistry on calcification and photosynthesis in the hermatypic coral Acropora eurystoma. *Limnol. Oceanogr.*, 51(3):1284–1293, May 2006.

B. A. Seibel and P. J. Walsh. Potential impacts of CO_2 injection on deep-sea biota. *Science*, 249(5541):319–320, October 2001.

D. P. Van Vuuren and B. O'Neill. The consistency of IPPC's SRES scenarios to recent literature and recent projections. *Climatic Change*, 75(1-2):9–46, March 2006. doi: 10.1007/s10584-005-9031-0.

Y. M. Wang, J. L. Lean, and N. R. Sheeley. Modeling the sun's magnetic field and irradiance since 1713. *Astrophysical Journal*, 625:522–538, 2005.

S. Zhong and A. Mucci. Calcite and aragonite precipitation from seawater solutions of various salinities: Precipitation rates and overgrowth compositions. *Chemical Geology*, 78:283–299, 1989.

Acknowledgments

I would like to thank ...

... Fortunat Joos for giving me the opportunity to write this thesis at the Climate and Environmental Physics department, for pointing out interesting and important topics in valuable discussions, and for his support during this time.

... Gian-Kasper Plattner for stimulating discussions and helpful comments on parts of this thesis.

... Thomas Frölicher for the collaboration and his help during my thesis.

... Kay Bieri for the excellent IT support and for the very agreeable working atmosphere in our office.

... all the members of the Climate and Environmental Physics department for the enjoyable atmosphere.

... Dominique Rothen for her support and everything.

... my parents for their support during my education and throughout my life.